STUDY ON A BIDIRECTIONAL RECTANGULAR RING ANTENNA

SUTHASINEE LAMULTREE

A THESIS SUBMITTED IN PARTIAL FULFILLMENT OF
THE REQUIREMENT FOR THE DEGREE OF
DOCTOR OF ENGINEERING IN ELECTRICAL ENGINEERING
FACULTY OF ENGINEERING
KING MONGKUT'S INSTITUTE OF TECHNOLOGY LADKRABANG
2008

KMITL-2009-EN-D-018-002

หัวข้อวิทยานิพนธ์ การศึกษาสายอากาศวงแหวนสี่เหลี่ยมมุมฉากที่แพร่กระจายคลื่นแบบสองทิศทาง

นักศึกษา นางสาวสุธาสินี ละมุลตรี

รหัสประจำตัว 47060001

ปริญญา วิศวกรรมศาสตรดุษฎีบัณฑิต

สาขาวิชา วิศวกรรมไฟฟ้า

พ.ศ. 2551

อาจารย์ที่ปรึกษาวิทยานิพนธ์ ผศ.ดร. ชูวงค์ พงศ์เจริญพาณิชย์

บทคัดย่อ

วิทยานิพนธ์ฉบับนี้เป็นการนำเสนอการศึกษาสายอากาศวงแหวนสี่เหลี่ยมมุมฉากที่แพร่กระจายคลื่นแบบสองทิศทาง โดยโครงสร้างของสายอากาศนี้มีลักษณะไม่ซับซ้อน ประกอบด้วยวงแหวนสี่เหลี่ยมมุมฉากที่ล้อมรอบตัวป้อนสัญญาณที่เป็นโพรบเชิงเส้น ในการพิจารณาคุณลักษณะการแพร่กระจายคลื่นของสายอากาศ ได้ใช้วิธีฟังก์ชันกรีนไดแอดิก ซึ่งให้สูตรแสดงความสัมพันธ์ของพารามิเตอร์ต่างๆ อย่างชัดเจน และนอกจากนี้ได้ใช้วิธีโมเมนต์ที่มีฟังก์ชันฐาน RWG (Rao-Wilton-Glisson) ที่พิจารณาการกระจายกระแสที่แม่นยำกว่าวิธีฟังก์ชันกรีนไดแอดิก (ในวิทยานิพนธ์นี้) เพื่อพิจารณาคุณลักษณะเชิงอิมพีแดนซ์ และค่าอัตราการขยายของสายอากาศ และศึกษาผลกระทบของพารามิเตอร์ต่างๆ ต่อคุณลักษณะของสายอากาศ เช่น ความกว้าง ความสูง และความยาวของวงแหวน ตลอดจนความยาวและตำแหน่งของโพรบป้อนสัญญาณ สำหรับพิจารณาหาพารามิเตอร์ที่ดีที่สุดของสายกาศวงแหวนสี่เหลี่ยมมุมฉากที่ป้อนสัญญาณด้วยโพรบเชิงเส้นที่แพร่กระจายคลื่นแบบสองทิศทาง นอกจากนี้ได้นำเสนอการปรับปรุงคุณลักษณะของสายอากาศ ให้สามารถใช้งานในระบบแถบกว้างความถี่ช่วงกว้างได้ โดยการใช้ตัวป้อนสัญญาณแผ่นโมโนโพลแบบขั้นบันไดแทนโพรบเชิงเส้น สำหรับการพิจารณาเริ่มจากพารามิเตอร์ของวงแหวนที่เหมาะสมที่มีความถี่เรโซแนนซ์ตามที่ต้องการ และให้แบบรูปการแพร่กระจายคลื่นแบบสองทิศทาง จากนั้นได้ศึกษาพารามิเตอร์ของตัวป้อนสัญญาณแผ่นโมโนโพลแบบขั้นบันไดที่เหมาะสมและสามารถปรับปรุงอิมพีแดนซ์ของสายกาศให้สามารถใช้งานในแถบกว้างความถี่กว้างยิ่งยวด (Ultra-wide band)ได้ และได้ทำการจำลองผลของสายอากาศโดยใช้โปรแกรมจำลองผล CST Microwave Simulation เพื่อศึกษาคุณลักษณะเชิงอิมพีแดนซ์ แบบรูปการแพร่กระจายคลื่นและค่าอัตราการขยายของสายอากาศ นอกจากนี้ได้ทำการสร้างและทดสอบคุณลักษณะของสายอากาศเพื่อยืนยันผลการวิเคราะห์จากทฤษฎีและการจำลองผล ซึ่งพบว่าผลที่ได้จากการคำนวณเชิงทฤษฎีและการจำลองผลนั้นสอดคล้องกับผลที่ได้จากการทดสอบ

Thesis Title	Study on a Bidirectional Rectangular Ring Antenna
Student	Miss Suthasinee Lamultree
Student ID.	47060001
Degree	Doctor of Engineering
Programe	Electrical Engineering
Year	2008
Thesis Advisor	Asst.Prof.Dr. Chuwong Phongcharoenpanich

ABSTRACT

This thesis presents an analysis of a bidirectional rectangular ring antenna. It is very simple structure with a feeder surrounded by a rectangular ring. In this thesis, the radiation characteristics of a probe-excited rectangular ring antenna are analyzed by the dyadic Green's function approach providing a closed form. Its impedance characteristics and gain are determined by using the Method of Moments (MoM) with the Rao-Wilton-Glisson (RWG) basis functions that obtain more accurate current comparing with the dyadic Green's function approach (which used in this thesis). The parametric effects of the rectangular ring and excited probe, such as ring width, ring length, ring height, probe length and probe position, to its characteristics are investigated. Consequently, the optimum parameters, which provide bidirectional pattern, are obtained. In addition, the bandwidth-enhancement of a bidirectional rectangular ring antenna is presented by using an ultra-wideband rectangular ring fed by stepped monopole antenna. The initial parameters of rectangular ring are first considered to obtain the bidirectional pattern with a desired resonant frequency. Subsequently, the parameters of stepped-monopole excitation for enhancing impedance bandwidth are investigated. To study the impedance characteristic, radiation pattern and gain, the simulations of the proposed antenna have been carried out using the CST Microwave Simulation. Furthermore, the prototype antenna was fabricated and measured to verify the theory and simulations. Obviously, the simulated and measured results are reasonably in good agreement.

ACKNOWLEDGEMENTS

This thesis is the final submission to accomplish the Doctor of Engineering of Electrical Engineering at King Mongkut's Institute of Technology Ladkrabang. During the time I have been working on my thesis, I have been received good support, assistance and encouragement from many people as below. Therefore, I would like to take this opportunity to express my sincere thanks to those who have contributed directly or indirectly to bring this thesis to the final format.

I would like to express my grateful to my advisor, Asst. Prof. Dr. Chuwong Phongcharoenpanich, who has always given me suggestions for a long-term. I am especially thankful for the various opportunities that he gave to me including his guidance and kindly support. In addition, I would like to express my grateful to Prof. Dr. Monai Krairiksh and Assoc. Prof. Dr. Sompol Kosulvit for their kindly discussions and suggestions. Moreover, I would like to express my grateful to thank to Dr. Titipong Lertwiriyaprapa for his kindness in the read-proof of my thesis.

Furthermore, I would love to thank to all alumnae and present members in Wireless Communication Laboratory for their helpful discussions and friendship. I would love to express my thanks to especially Dr. Krittaya Chawanonphithak and Mr. Phairote Wounchoum for their helpful discussions, and Mr. Kittisak Phaebua and Mr. Chawanthawat Mansap for their helpful of the fabrication and measurement.

Moreover, I would like to extend my thankful to Asian University to allow time for me doing my thesis. In addition, I would like to express my grateful to Asst. Prof. Dr. Danai Torrungrueng for his kindly suggestions for many things.

For my parents including all members in my family (also, my dear grandma and my love brother who see me in my dream) and my sister's family, most importantly, I would never be who I am and what I am without them. I am proud to give a credit to them who are totally the main reason to drive me to be at this point. I would love to express my grateful and appreciation to all of them for their support, encouragement, stimulation and enthusiasm.

Finally, it is my wish that this thesis will be a valuable source of data for those who are interested in this field.

Suthasinee Lamultree

TABLE OF CONTENTS

TABLE OF CONTENTS (CONTINUE)

LIST OF TABLES

LIST OF FIGURES

LIST OF FIGURES (CONTINUE)

LIST OF FIGURES (CONTINUE)

Figure Page

CHAPTER 1
INTRODUCTION

1.1 Rationale

Recently, the wireless communications become essential in human activity. Therefore, the demand for using a mobile telephone is increased everywhere. Mostly, the omnidirectional antennas [1]-[3] are widely employed to cover the communicable cell around it. Generally, the base station antennas in microcellular system for the urban areas are located lower than the surrounded buildings along the streets and sometime they located in the underground areas. Many base stations are placed in doors such as in the building, underground shopping areas, subway station; the communicable cell is formed along the street. For these environments, the omnidirectional pattern is degraded when it places closed or attached to the wall or metal. If a bidirectional antenna is applied, the deterioration on the omnidirectional antenna performance can be avoided. In addition, bidirectional antennas have been developed to enlarge the cell size in the street microcell environment [4], [5]. Therefore, many researches and developments on bidirectional antenna have been extensively conducted [6]-[13]. It was found that a bidirectional pattern can be achieved from a bidirectional rod antenna (BIRA) comprising a collinear antenna and parasitic wires [6] by adjusting the spacing between the collinear antenna and the parasitic wire, and the length of the parasitic wires. However, its bidirectional properties are sensitive to the length of the parasitic elements. Therefore, it may not be suitable for mass production. A bidirectional rod antenna comprising a narrow patch (BNPA) and parasitic elements placing on both sides of radiation patches was presented in [7] providing a bidirectional pattern without degrading the efficiency. Nevertheless, adding parasitic elements makes the antenna structure in [7] even more complicated. Moreover, a dual-band bidirectional reconfigurable antenna by controlling switches in the slots etched on the koch patch, different far field bidirectional patterns at the dual-band around 60 GHz/80 GHz could be achieved [8]. In the work by [8], an electronically controlling the switches in the slots of the patch is required which involves more complication. From the aforementioned researches, it is evident that the development of a bidirectional antenna which has suitable characteristics for the applications of the base station antenna in microcellular system,

especially for the confined areas, is desired. Moreover, the low cost must be considered since the number of cell is very large. Therefore, a series of probe-excited different shapes of rings, such as rectangular, circular, elliptical rings, are introduced [9]-[13]; the omnidirectional pattern of linear probe is forced by the surrounded rings to provide a bidirectional pattern. Because of the simple structure, the bidirectional rectangular ring was presented in [9], [11]-[12] to be used as a base station antenna at the narrow and long part serviced areas. Furthermore, a bidirectional antenna using a linear probe-excited circular ring was also proposed [10] to serve these demands. Although the circular ring provides the slightly higher gain than the rectangular ring, its beamwidth cannot be easily adjusted due to the symmetrical structure. Also, a bidirectional antenna using a linear probe-excited elliptical ring was proposed [13]. However, it is noted that rectangular ring is more simple structure compared to an elliptical one. It is also possible to adjust the beamwidth of the antenna corresponding to the applications by changing the ring width and ring height. Furthermore, the desired directivity is easily obtained by varying the ring length.

A probe-excited rectangular ring antenna was proposed in [9] to be used as a base station antenna of a Personal Communication Telephone (PCT). To simplify the analysis in [9], only equivalent magnetic current density on the aperture was considered for determining the electric and magnetic far fields excluding a probe excitation, since the aperture is assumed to be placed on the infinite ground plane. In this thesis, the aperture is assumed to place in free space and, a probe-excited is included to analyze by taking into account the equivalent electric and magnetic current densities on the aperture. Furthermore, the mode distributions in the rectangular ring are expressed to consider its influence to the radiation fields. Theoretically, there are many techniques to analyze the radiation from the aperture fed by probe in open literature [14]-[20]. Each method possesses its advantages and disadvantages. In this thesis, the dyadic Green's function approach [19]-[24] is used to analyze the radiation characteristics of the proposed antenna since it is straightforward, and the closed form solution can be obtained. The rigorous analysis for determining the fields inside the rectangular ring, equivalent electric and magnetic current densities on the aperture, and far fields radiation is expressed in detail. Nevertheless, the analysis is performed under the assumption that the current is assumed to be sinusoidal distribution, the mutual coupling between the two apertures and the diffraction at the edge of the ring are neglected. Hence, this solution provides

a less correction of input impedance under those assumptions. The Method of Moments (MoM) with the Rao-Wilton-Glisson (RWG) basis functions [25]-[26], which is probably the most popular choice when using the MoM to solve surface integral equations for arbitrarily shaped objects, is applied to determine the impedance characteristic and gain of the antenna. For this method, the basis functions include not only for each member of patch which contains an edge lying on the boundary of the unit cell, but also the adjacent face-pairs of the triangulated surface. Therefore, the more accurate solutions can be obtained from this technique comparing with the previous solution (the dyadic Green's function approach). However, the computation time for RWG-MoM is longer than the dyadic Green's function approach, and the closed form is not available for RWG-MoM.

In addition to a bidirectional rectangular ring fed by linear probe, a technique to enhance the antenna bandwidth is also introduced. In this thesis, to enhance the impedance bandwidth, a stepped-monopole excitation is used instead of linear-monopole (probe) excitation [27]. This antenna can be applied in an ultra-wideband (UWB) application [28] which is gaining prominence and becoming very attractive in modern wireless and mobile communication systems. In the analyses, firstly, the initial parameters of rectangular ring are considered to obtain the bidirectional pattern with the desired resonant frequency. Subsequently, the parameters of stepped monopole for enhancing impedance bandwidth are investigated. To study the impedance and radiation behaviors, the CST Microwave Simulation [29] based on finite integration technique (FIT), which is a well know as the simulator for electromagnetic fields (EM), is used. Because it is very convenient for varying several parameters with less time consume. The simulations of the proposed antenna have been carried out. Finally, the appropriated parameters are provided. Furthermore, to verify the simulation, the prototype antenna was fabricated and measured.

1.2 Scope of the Thesis

This thesis is organized as follows. Chapter 2 presents the theory of the antenna including the antenna structure and the derivation expressions by using the dyadic Green's function approach. The normalized magnitudes of the equivalent electric and magnetic current densities in the rectangular ring for various modal distributions are shown. The radiation characteristics as the function of antenna parameters are studied.

In Chapter 3, the RWG-MoM is introduced to determine impedance characteristic, gain and radiation pattern of a probe-excited rectangular ring antenna. In addition, a technique for improving a bandwidth of the antenna for wideband application is presented. Therefore, a bidirectional UWB antenna using rectangular ring fed by stepped monopole is shown in Chapter 4. Then, the fabrication and measurement for validity of the theoretical and simulated results are provided in Chapter 5. Finally, the conclusions and discussions are presented in Chapter 6.

CHAPTER 2
ANALYSIS OF RADIATION CHARACTERISTICS BY THE DYADIC GREEN'S FUNCTION APPROACH

2.1 Introduction

In this chapter, radiation characteristics of a probe-excited rectangular ring antenna are investigated by using the dyadic Green's function approach. The radiation characteristics, such as radiation pattern, beam-peak direction, half-power beamwidth and directivity, are analyzed. In addition, the effects of the excited probe and rectangular ring to the modal distributions are described. This chapter is organized as follows. Section 2.2 presents the theory of the antenna including the antenna structure and the derivation expressions. In Section 2.3, the radiation characteristics as a function of antenna parameters are shown. Finally, the summary is addressed in Section 2.4.

2.2 Theory

The proposed antenna consists of a linear electric probe of length l aligned along y direction at the position of ($x = s$, $y = -b/2$, $z = 0$). The probe is surrounded by rectangular ring of width a, height b and length c, respectively, as shown in Fig. 2.1.

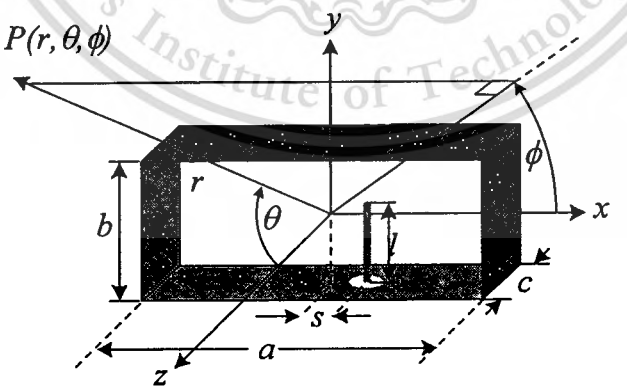

Fig. 2.1 Antenna structure.

The rectangular ring is considered as a part of rectangular waveguide that is truncated at $z = +c/2$ and $z = -c/2$, where the mutual coupling between the two apertures and the diffraction at the edge of the aperture are omitted. In this thesis, the

propagation direction and the piloting vector in z direction is assumed. In addition, the time convention $e^{j\omega t}$ is used and suppressed, where $\omega = 2\pi f$ and f is the frequency. The scalar wave function [21] solved by the method of separation of variables is

$$\psi^{\pm z}_{\substack{e\\o}mn}(k_z) = \begin{Bmatrix} C_x & C_y \\ S_x & S_y \end{Bmatrix} e^{\mp jk_z z}, \qquad \begin{matrix} m = 1,\ 2,\ 3,\ \ldots \\ n = 0,\ 1,\ 2,\ \ldots \end{matrix} \tag{2.1}$$

where $S_x = \sin\left(k_x\left(x+\frac{a}{2}\right)\right)$, $C_x = \cos\left(k_x\left(x+\frac{a}{2}\right)\right)$, $S_y = \sin\left(k_y\left(y+\frac{b}{2}\right)\right)$,

$C_y = \cos\left(k_y\left(y+\frac{b}{2}\right)\right)$, $k_x = \frac{m\pi}{a}$, $k_y = \frac{n\pi}{b}$, $k_c = k_x^2 + k_y^2$, $k_z = \sqrt{k^2 - (k_x^2 + k_y^2)}$,

$k = \omega\sqrt{\mu_0\varepsilon_0}$, $\mu_0 = 4\pi\times10^{-7}$ H/m, $\varepsilon_0 = 8.854\times10^{-12}$ F/m. The superscript $\pm z$ in the right side denotes the field radiations in $+z$ and $-z$ directions, respectively. The subscript e and o are an abbreviation for the even and odd functions, respectively.

The vector wave functions, $\overline{M}_{emn}$ and $\overline{N}_{omn}$, satisfy the vector Dirichlet boundary condition at the conducting wall ($\hat{a}_n \times \overline{M}_{emn} = 0$ and $\hat{a}_n \times \overline{N}_{omn} = 0$), where $\hat{a}_n$ is the normal unit vector. The vector wave functions $\overline{M}_{emn}$ and $\overline{N}_{omn}$ represent the electric field of TE_{mn} and TM_{mn} modes, respectively. In the same manner, $\overline{M}_{omn}$ and $\overline{N}_{emn}$ are the vector wave functions that satisfy the vector Neumann boundary condition $\hat{a}_n \times \begin{Bmatrix} \nabla\times\overline{M}_{omn} \\ \nabla\times\overline{N}_{emn} \end{Bmatrix} = 0$. Hence, they can be written as

$$\overline{M}_{\substack{e\\o}mn}(k_z) = \nabla\times\left[\hat{a}_z\psi_{\substack{e\\o}mn}(k_z)\right] \tag{2.2}$$

and

$$\overline{N}_{\substack{e\\o}mn}(k_z) = \frac{1}{k}\nabla\times\nabla\times\left[\hat{a}_z\psi_{\substack{e\\o}mn}(k_z)\right]. \tag{2.3}$$

Following the method of magnetic dyadic Green function and applying the Ohm-Rayleigh method, the magnetic dyadic Green function due to an electric source ($\overline{\overline{G}}_{HJ}(\overline{R},\overline{R}')$) that satisfies the dyadic differential equation is

$$\nabla\times\nabla\times\overline{\overline{G}}_{HJ}(\overline{R},\overline{R}') - k^2\overline{\overline{G}}_{HJ}(\overline{R},\overline{R}') = \nabla\times\left[\overline{\overline{I}}\delta(\overline{R}-\overline{R}')\right]. \tag{2.4}$$

where

$$\overline{\overline{G}}_{HJ} = \begin{bmatrix} G_{HJ}^{xx} & G_{HJ}^{xy} & G_{HJ}^{xz} \\ G_{HJ}^{yx} & G_{HJ}^{yy} & G_{HJ}^{yz} \\ G_{HJ}^{zx} & G_{HJ}^{zy} & G_{HJ}^{zz} \end{bmatrix},$$

the $\delta\left(\overline{R}-\overline{R'}\right)$ denotes the Dirac delta function, which is equal to $\delta(x-x')\delta(y-y')\delta(z-z')$ in the Cartesian coordinate. $\overline{\overline{I}}$ is the unit dyadic. The primed variables (x', y', z') and unprimed variables (x,y,z) are the source point and the observation point, respectively. The relationship in (2.4) is defined in the domain $-\frac{a}{2} \le x \le \frac{a}{2}$, $-\frac{b}{2} \le y \le \frac{b}{2}$, $-\infty \le z \le \infty$, and the Neuman boundary condition

$$\hat{a}_n \times \nabla \times \overline{\overline{G}}_{HJ}(\overline{R}, \overline{R'}) = 0, \tag{2.5}$$

at x = -$a/2$ and $a/2$, y = -$b/2$ and $b/2$. The eigenfunction expansion of $\overline{\overline{G}}_{HJ}$ in term of the rectangular vector wave functions is given by [21]

$$\overline{\overline{G}}_{HJ}(\overline{R}, \overline{R'}) = \int_{-\infty}^{\infty} dk_z \frac{jk}{ab} \sum_{m,n} \frac{(2-\delta_0)\kappa}{\pi a b k_c^2 \left(\kappa^2 - k^2\right)} \left[\overline{N}_{emn}(k_z) \overline{M'}_{emn}(-k_z) + \overline{M}_{omn}(k_z) \overline{N'}_{omn}(-k_z) \right] \tag{2.6}$$

where, $\kappa^2 = \left(\frac{m\pi}{a}\right)^2 + \left(\frac{n\pi}{b}\right)^2 + k_z^2 = k_c^2 + k_z^2$. The δ_0 denotes the Kronecker delta function defined as

$$\delta_0 = \begin{cases} 1 & m \text{ or } n = 0 \\ 0 & m \text{ and } n \neq 0. \end{cases} \tag{2.7}$$

$$\overline{M}_{emn}^{\pm z}(k_z) = \left(-\hat{a}_x k_y C_x S_y + \hat{a}_y k_x S_x C_y\right) e^{\mp jk_z z}, \tag{2.8}$$

$$\overline{N}_{omn}^{\pm z}(k_z) = \frac{1}{\kappa}\left(\mp \hat{a}_x jk_z k_x C_x S_y \mp \hat{a}_y jk_z k_y S_x C_y + \hat{a}_z k_c^2 S_x S_y\right) e^{\mp jk_z z}, \tag{2.9}$$

$$\overline{M}_{omn}^{\pm z}(k_z) = \left(\hat{a}_x k_y S_x C_y - \hat{a}_y k_x C_x S_y\right) e^{\mp jk_z z} \tag{2.10}$$

and

$$\overline{N}_{emn}^{\pm z}(k_z) = \frac{1}{k}\left(\pm \hat{a}_x jk_z k_x S_x C_y \pm \hat{a}_y jk_z k_y C_x S_y + \hat{a}_z k_c^2 C_x C_y\right) e^{\mp jk_z z}. \tag{2.11}$$

Note that the primed auxiliary parameters are associated to the source location.

By applying the contour integration, (2.6) becomes

$$\overline{\overline{G}}_{HJ}^{\pm z}(\overline{R},\overline{R'}) = \begin{cases} -\dfrac{jk}{ab}\displaystyle\sum_{m,n}\frac{2-\delta_0}{k_c^2 k_z}\left[\overline{N}_{emn}(+k_z)\overline{M'}_{emn}(-k_z)+\overline{M}_{omn}(+k_z)\overline{N'}_{omn}(-k_z)\right]; & z > z' \\ +\dfrac{jk}{ab}\displaystyle\sum_{m,n}\frac{2-\delta_0}{k_c^2 k_z}\left[\overline{N}_{emn}(-k_z)\overline{M'}_{emn}(+k_z)+\overline{M}_{omn}(-k_z)\overline{N'}_{omn}(+k_z)\right]; & z < z'. \end{cases} \tag{2.12}$$

The electric dyadic Green function due to an electric source $\overline{\overline{G}}_{EJ}(\overline{R},\overline{R'})$ is obtained from the relationship

$$\nabla\times\overline{\overline{G}}_{HJ}(\overline{R},\overline{R'}) = \overline{\overline{I}}\delta(\overline{R}-\overline{R'})+k^2\overline{\overline{G}}_{EJ}(\overline{R},\overline{R'}). \tag{2.13}$$

Then, we obtain

$$\overline{\overline{G}}_{EJ}^{\pm z}(\overline{R},\overline{R'}) = -\hat{a}_z\hat{a}_z\frac{1}{k^2}\delta(\overline{R}-\overline{R'}) + \begin{cases} -\dfrac{j}{ab}\displaystyle\sum_{m=1}^{\infty}\sum_{n=0}^{\infty}\frac{2-\delta_0}{k_c^2 k_z}\left[\overline{M}_{emn}(+k_z)\overline{M'}_{emn}(-k_z)+\overline{N}_{omn}(+k_z)\overline{N'}_{omn}(-k_z)\right]; & z > z' \\ +\dfrac{j}{ab}\displaystyle\sum_{m=1}^{\infty}\sum_{n=0}^{\infty}\frac{2-\delta_0}{k_c^2 k_z}\left[\overline{M}_{emn}(-k_z)\overline{M'}_{emn}(+k_z)+\overline{N}_{omn}(-k_z)\overline{N'}_{omn}(+k_z)\right]; & z < z', \end{cases} \tag{2.14}$$

The electric field $\left(\overline{E}\left(\overline{R}\right)\right)$ inside the ring with the probe excitation is determined by using

$$\overline{E}^{\pm z}(\overline{R}) = \mp j\omega\mu_0\iiint_V \overline{\overline{G}}_{EJ}^{\pm}(\overline{R},\overline{R'})\cdot\overline{J}(\overline{R'})dV', \tag{2.15}$$

where $\overline{\overline{G}}_{EJ}^{\pm}(\overline{R},\overline{R'})$ is obtained from (2.14) and $\overline{J}(\overline{R'})$ is the electric current distribution along the probe. In this chapter, the linear probe directed in y direction has a small diameter compared to the wavelength and the sinusoidal distribution is reasonably assumed as

$$\overline{J}(\overline{R'}) = \hat{a}_y\frac{I_m}{d}\sin k\left(l-y'-\frac{b}{2}\right);\ -\frac{b}{2}\le y'\le -\frac{b}{2}+l, \tag{2.16}$$

where I_m is the maximum current that is normalized to be unity and d is the diameter of the probe. Since the probe is oriented in y direction, hence only G_{EJ}^{xy}, G_{EJ}^{yy}, and G_{EJ}^{zy} can contribute to the electric field. All of these components are derived and shown as

$$G_{EJ}^{xy,\pm z}=\begin{cases}-\dfrac{j}{ab}\displaystyle\sum_{m=1}^{\infty}\sum_{n=0}^{\infty}\dfrac{2-\delta_0}{k_c^2k_z}\left(-k_xk_yC_xS_yS_x'C'+\dfrac{1}{\kappa^2}k_z^2k_xk_yC_xS_yS_x'C_y'\right)e^{-jk_z(z-z')};\ z>z'\\ \dfrac{j}{ab}\displaystyle\sum_{m=1}^{\infty}\sum_{n=0}^{\infty}\dfrac{2-\delta_0}{k_c^2k_z}\left(-k_xk_yC_xS_yS_x'C_y'+\dfrac{1}{\kappa^2}k_z^2k_xk_yC_xS_yS_x'C_y'\right)e^{+jk_z(z'-z)};\ z<z',\end{cases} \tag{2.17}$$

$$G_{EJ}^{yy,\pm z}=\begin{cases}-\dfrac{j}{ab}\displaystyle\sum_{m=1}^{\infty}\sum_{n=0}^{\infty}\dfrac{2-\delta_0}{k_c^2k_z}\left(k_x^2S_xC_yS_x'C_y'+\dfrac{1}{\kappa^2}k_z^2k_y^2S_xC_yS_x'C_y'\right)e^{-jk_z(z-z')};\ z>z'\\ \dfrac{j}{ab}\displaystyle\sum_{m=1}^{\infty}\sum_{n=0}^{\infty}\dfrac{2-\delta_0}{k_c^2k_z}\left(k_x^2S_xC_yS_x'C_y'+\dfrac{1}{\kappa^2}k_z^2k_y^2S_xC_yS_x'C_y'\right)e^{+jk_z(z'-z)};\ z<z'\end{cases} \tag{2.18}$$

and

$$G_{EJ}^{zy,\pm z}=\begin{cases}-\dfrac{j}{ab}\displaystyle\sum_{m=1}^{\infty}\sum_{n=0}^{\infty}\dfrac{2-\delta_0}{k_c^2k_z}\dfrac{j}{\kappa^2}k_c^2k_zk_yS_xS_yS_x'C_y'e^{-jk_z(z-z')};\ z>z'\\ \dfrac{j}{ab}\displaystyle\sum_{m=1}^{\infty}\sum_{n=0}^{\infty}\dfrac{2-\delta_0}{k_c^2k_z}\left(-\dfrac{j}{\kappa^2}\right)k_c^2k_zk_yS_xS_yS_x'C_y'e^{+jk_z(z'-z)};\ z<z'.\end{cases} \tag{2.19}$$

Consequently, the electric field inside the ring x, y, and z components are

$$E_x^{\pm z}=-\frac{\omega\mu_0I_m}{abd}\sum_{m=1}^{\infty}\sum_{n=0}^{\infty}\left\{\frac{2-\delta_0}{k_c^2k_z}(-k)\sin\left(k_x\left(s+\frac{a}{2}\right)\right)\left(\frac{\cos(k_yl)-\cos(kl)}{k_y^2-k^2}\right)\right.$$
$$\left.\times\left(-k_xk_y+\frac{k_z^2k_xk_y}{\kappa^2}\right)\cos\left(k_x\left(x+\frac{a}{2}\right)\right)\sin\left(k_y\left(y+\frac{b}{2}\right)\right)e^{-jk_zz}\right\}, \tag{2.20}$$

$$E_y^{\pm z}=-\frac{\omega\mu_0I_m}{abd}\sum_{m=1}^{\infty}\sum_{n=0}^{\infty}\left\{\frac{2-\delta_0}{k_c^2k_z}(-k)\sin\left(k_x\left(s+\frac{a}{2}\right)\right)\left(\frac{\cos(k_yl)-\cos(kl)}{k_y^2-k^2}\right)\right.$$
$$\left.\times\left(k_x^2+\frac{k_z^2k_y^2}{\kappa^2}\right)\sin\left(k_x\left(x+\frac{a}{2}\right)\right)\cos\left(k_y\left(y+\frac{b}{2}\right)\right)e^{-jk_zz}\right\} \tag{2.21}$$

and

$$E_z^{\pm z}=-j\frac{\omega\mu_0I_m}{abd}\sum_{m=1}^{\infty}\sum_{n=0}^{\infty}\left\{\frac{2-\delta_0}{\kappa^2}(-k)\sin\left(k_x\left(s+\frac{a}{2}\right)\right)\left(\frac{\cos(k_yl)-\cos(kl)}{k_y^2-k^2}\right)\right.$$
$$\left.\times k_y\sin\left(k_x\left(x+\frac{a}{2}\right)\right)\sin\left(k_y\left(y+\frac{b}{2}\right)\right)e^{-jk_zz}\right\}. \tag{2.22}$$

Then, the electric and magnetic fields inside the ring are transformed to be the equivalent current densities at the aperture by considering as the source for determining the far field radiations. Since the aperture is assumed to be in the free space. Thus, both equivalent magnetic and electric current densities are determined by

$$\left.\begin{aligned}\overline{M}_s &= \overline{E}_a \times \hat{a}_n \\ \overline{J}_s &= \hat{a}_n \times \overline{H}_a\end{aligned}\right\} \begin{aligned} &-a/2 \le x' \le a/2 \\ &-b/2 \le y' \le b/2 \end{aligned} \qquad (2.23)$$
$$\overline{M}_s \simeq \overline{J}_s \simeq 0 \quad \text{elsewhere}$$

where $\overline{E}_a$ and $\overline{H}_a$ are fields at the aperture.

The equivalent magnetic current densities ($\overline{M}_s$) at the two apertures are obtained from

$$\overline{M}_s^{\pm z}(\overline{R}) = \overline{E}^{\pm z}(\overline{R})\Big|_{z=\pm c/2} \times (\pm \hat{a}_z) \qquad (2.24)$$

The resultant equivalent magnetic current densities are

$$\begin{aligned}\overline{M}_s^{\pm z}(\overline{R}) = -\frac{\omega\mu_0 I_m}{abd}\sum_{m=1}^{\infty}\sum_{n=0}^{\infty}&\left\{\frac{2-\delta_0}{k_c^2 k_z}(-k)\sin\left(k_x\left(s+\frac{a}{2}\right)\right)\right\}\left(\frac{\cos(k_y l)-\cos(kl)}{k_y^2-k^2}\right)e^{-jk_z z} \\ &\times\left\{\pm\hat{a}_x\left[\left(k_x^2+\frac{k_z^2 k_y^2}{\kappa^2}\right)\sin\left(k_x\left(x+\frac{a}{2}\right)\right)\cos\left(k_y\left(y+\frac{b}{2}\right)\right)\right]\right. \\ &\left.\mp\hat{a}_y\left[\left(-k_x k_y+\frac{k_z^2 k_x k_y}{\kappa^2}\right)\cos\left(k_x\left(x+\frac{a}{2}\right)\right)\sin\left(k_y\left(y+\frac{b}{2}\right)\right)\right]\right\}.\end{aligned} \qquad (2.25)$$

By following the same fashion, the magnetic field $\left(\overline{H}\left(\overline{R}\right)\right)$ can be found from

$$\overline{H}(\overline{R}) = \iiint_V \overline{\overline{G}}_{HJ}(\overline{R},\overline{R}')\cdot\overline{J}(\overline{R}')dV' \qquad (2.26)$$

where $\overline{\overline{G}}_{HJ}$, after some mathematical manipulations, can be derived as

$$G_{HJ}^{xy,\pm z} = \frac{k}{ab}\sum_{m=1}^{\infty}\sum_{n=0}^{\infty}\frac{(2-\delta_0)}{k_c^2\kappa}S_x C_y S_x' C'\begin{cases}(k_x^2+k_y^2)e^{-jk_z(z-z')}; & z>z' \\ (-k_x^2-k_y^2)e^{+jk_z(z'-z)}; & z<z',\end{cases} \qquad (2.27)$$

$$G_{HJ}^{yy,\pm z} = 0 \qquad (2.28)$$

and

$$G_{HJ}^{zy,\pm z} = \begin{cases}-\dfrac{jk}{ab}\displaystyle\sum_{m=1}^{\infty}\sum_{n=0}^{\infty}\frac{(2-\delta_0)}{k_c^2 k_z\kappa}k_c^2 k_x C_x S_y S_x' S_y' e^{-jk_z(z-z')}; & z>z' \\ \dfrac{jk}{ab}\displaystyle\sum_{m=1}^{\infty}\sum_{n=0}^{\infty}\frac{(2-\delta_0)}{k_c^2 k_z\kappa}k_c^2 k_x C_x S_y S_x' S_y' e^{+jk_z(z'-z)}; & z<z'.\end{cases} \qquad (2.29)$$

The magnetic field components are

$$H_x^{\pm z} = \pm \frac{kI_m}{abd} \sum_{m=1}^{\infty} \sum_{n=0}^{\infty} \left\{ \frac{(2-\delta_0)}{\kappa k_c^2} (-k) \sin\left(k_x \left(s + \frac{a}{2} \right) \right) \left(\frac{\cos(k_y l) - \cos(kl)}{(k_y^2 - k^2)} \right) e^{-jk_z z} \right.$$
$$\left. \times \left(k_x^2 + k_y^2 \right) \sin\left(k_x \left(x + \frac{a}{2} \right) \right) \cos\left(k_y \left(y + \frac{b}{2} \right) \right) \right\}, \tag{2.30}$$

$$H_y^{\pm z} = 0 \tag{2.31}$$

and

$$H_z^{\pm z} = \mp j \frac{kI_m}{abd} \sum_{m=1}^{\infty} \sum_{n=0}^{\infty} \left\{ \frac{(2-\delta_0)}{\kappa k_c^2} (-k) \sin\left(k_x \left(s + \frac{a}{2} \right) \right) \left(\frac{\cos(k_y l) - \cos(kl)}{(k_y^2 - k^2)} \right) e^{-jk_z z} \right.$$
$$\left. \times \frac{k_x k_c^2}{k_z} \cos\left(k_x \left(x + \frac{a}{2} \right) \right) \cos\left(k_y \left(y + \frac{b}{2} \right) \right) \right\}. \tag{2.32}$$

Similarly, the equivalent electric current densities $\left(\overline{J}_s\right)$ at the two apertures are

$$\overline{J}_s^{\pm z}(\overline{R}) = \pm \hat{a}_z \times \overline{H}(\overline{R})\Big|_{z=\pm c/2} \tag{2.33}$$

and

$$\overline{J}_s^{\pm z}\left(\overline{R}\right) = \frac{kI_m}{abd} \sum_{m=1}^{\infty} \sum_{n=0}^{\infty} \left\{ \frac{2-\delta_0}{k_c^2 \kappa} (-k) \sin\left(k_x \left(s + \frac{a}{2} \right) \right) \left(\frac{\cos(k_y l) - \cos(kl)}{k_y^2 - k^2} \right) e^{-jk_z z} \right.$$
$$\left. \times \left[\pm \hat{a}_y \left(k_x^2 + k_y^2 \right) \sin\left(k_x \left(x + \frac{a}{2} \right) \right) \cos\left(k_y \left(y + \frac{b}{2} \right) \right) \right] \right\}. \tag{2.34}$$

After the equivalent magnetic and electric current densities are readily obtained, the far-zone radiated field from a probe-excited rectangular ring antenna can be subsequently found by using radiation parameters from [30]. By neglecting the mutual coupling and diffraction at the edge of the ring and assuming that there is no reflection from the opposite aperture, a superposition of the fields from the two apertures can be applied. The radiated fields from the two apertures are combined with the same phase but in opposite directions. The resultant field can be written as follows

$$E_\theta^{\pm z}(r,\theta,\phi) \simeq -\frac{jke^{-jk\left(r \mp \frac{c}{2}\cos\theta\right)}}{4\pi r} \left(L_\phi^{\pm z} + \eta N_\theta^{\pm z} \right) \tag{2.35}$$

and

$$E_\phi^{\pm z}(r,\theta,\phi) \simeq +\frac{jke^{-jk\left(r \mp \frac{c}{2}\cos\theta\right)}}{4\pi r} \left(L_\theta^{\pm z} - \eta N_\phi^{\pm z} \right) \tag{2.36}$$

where the radiation factors are

$$N_\theta = \iint_s \left[J_x \cos\theta\cos\phi + J_y \cos\theta\sin\phi - J_z \sin\theta \right] e^{jkr'\cos\psi} ds', \tag{2.37}$$

$$N_\phi = \iint_s \left[-J_x \sin\phi + J_y \cos\phi \right] e^{jkr'\cos\psi} ds', \tag{2.38}$$

$$L_\theta = \iint_s \left[M_x \cos\theta\cos\phi + M_y \cos\theta\sin\phi - M_z \sin\theta \right] e^{jkr'\cos\psi} ds', \tag{2.39}$$

$$L_\phi = \iint_s \left[-M_x \sin\phi + M_y \cos\phi \right] e^{jkr'\cos\psi} ds'. \tag{2.40}$$

The differential path and area are represented by

$$ds' = dx'dy' \tag{2.41}$$

and

$$\begin{aligned} r'\cos\psi = r'\cdot\hat{r} &= (x'\hat{a}_x + y'\hat{a}_y)\cdot(\hat{a}_x \sin\theta\cos\phi + \hat{a}_y \sin\theta\sin\phi + \hat{a}_z \cos\theta) \\ &= x'\sin\theta\cos\phi + y'\sin\theta\sin\phi \end{aligned} \tag{2.42}$$

There for the radiation factors become

$$\begin{aligned} N_\theta^{\pm z} = \pm\frac{kI_m}{abd}\sum_{m=1}^{\infty}\sum_{n=0}^{\infty}\Bigg\{ & \frac{2-\delta_0}{k_c^2\kappa}\frac{ab}{4j}(-k)\sin\left(k_x\left(s+\frac{a}{2}\right)\right)\left(\frac{\cos(k_y l)-\cos(kl)}{k_y^2-k^2}\right)e^{-jk_z z} \\ & \times\left[\pm\left(k_x^2+k_y^2\right)\cos\theta\sin\phi\left(SA-SA'\right)\left(SB+SB'\right)\right]\Bigg\}, \end{aligned} \tag{2.43}$$

$$\begin{aligned} N_\phi^{\pm z} = \pm\frac{kI_m}{abd}\sum_{m=1}^{\infty}\sum_{n=0}^{\infty}\Bigg\{ & \frac{2-\delta_0}{k_c^2\kappa}\frac{ab}{4j}(-k)\sin\left(k_x\left(s+\frac{a}{2}\right)\right)\left(\frac{\cos(k_y l)-\cos(kl)}{k_y^2-k^2}\right)e^{-jk_z z} \\ & \times\left[\pm\left(k_x^2+k_y^2\right)\cos\phi\left(SA-SA'\right)\left(SB+SB'\right)\right]\Bigg\}, \end{aligned} \tag{2.44}$$

$$\begin{aligned} L_\theta^{\pm z} = -\frac{\omega\mu_0 I_m}{abd}\sum_{m=1}^{\infty}\sum_{n=0}^{\infty}\Bigg\{ & \frac{2-\delta_0}{k_c^2 k_g}\frac{ab}{4j}(-k)\sin\left(k_x\left(s+\frac{a}{2}\right)\right)\left(\frac{\cos(k_y l)-\cos(kl)}{k_y^2-k^2}\right)e^{-jk_z z} \\ & \times\Bigg[\pm\left(k_x^2+\frac{k_z^2k_y^2}{\kappa^2}\right)\cos\theta\cos\phi\left(SA-SA'\right)\left(SB+SB'\right) \\ & \mp\left(-k_xk_y+\frac{k_z^2k_xk_y}{\kappa^2}\right)\cos\theta\sin\phi\left(SA+SA'\right)\left(SB-SB'\right)\Bigg]\Bigg\} \end{aligned} \tag{2.45}$$

and

$$\begin{aligned} L_\phi^{\pm z} = -\frac{\omega\mu_0 I_m}{abd}\sum_{m=1}^{\infty}\sum_{n=0}^{\infty}\Bigg\{ & \frac{2-\delta_0}{k_c^2 k_g}\frac{ab}{4j}(-k)\sin\left(k_x\left(s+\frac{a}{2}\right)\right)\left(\frac{\cos(k_y l)-\cos(kl)}{k_y^2-k^2}\right)e^{-jk_z z} \\ & \times\Bigg[\mp\left(k_x^2+\frac{k_z^2k_y^2}{\kappa^2}\right)\sin\phi\left(SA-SA'\right)\left(SB+SB'\right) \\ & \mp\left(-k_xk_y+\frac{k_z^2k_xk_y}{\kappa^2}\right)\cos\phi\left(SA+SA'\right)\left(SB-SB'\right)\Bigg]\Bigg\}. \end{aligned} \tag{2.46}$$

Where $SA=\dfrac{\sin\left[(a/2)(k\sin\theta\cos\phi+k_x)\right]}{a/2(k\sin\theta\cos\phi+k_x)}e^{jk_xa/2}$,

$$SA'=\frac{\sin\left[(a/2)(k\sin\theta\cos\phi-k_x)\right]}{a/2(k\sin\theta\cos\phi-k_x)}e^{-jk_xa/2},$$

$$SB=\frac{\sin\left[(b/2)(k\sin\theta\sin\phi+k_y)\right]}{b/2(k\sin\theta\sin\phi+k_y)}e^{jk_yb/2}$$

and $$SB'=\frac{\sin\left[(b/2)(k\sin\theta\sin\phi-k_y)\right]}{b/2(k\sin\theta\sin\phi-k_y)}e^{-jk_yb/2}.$$

Consequently, the far-field radiation of the antenna can be expressed by substituting (2.43)-(2.46) into (2.35)-(2.36).

2.3 Radiation Characteristics

The total far-field distributions of the probe-excited rectangular ring antenna, is the summation of the electric fields from the two apertures as written in (2.35) and (2.36), that are obtained from the summation of electric and magnetic field distributions inside rectangular ring as written in (2.20)-(2.22), (2.30)-(2.32). It noted that by considering the minimum number of summation terms of m and n, which provide efficiently accurate results for minimizing the running time of the computed results, is important. The appropriate number of m and n for the numerical convergence should be obtained. Figure 2.2 shows the number of summation m and n for various c. Note that the solid lines with filled-circular and filled-rectangular are represented for the considered value of m and n, respectively; the unfilled-circular and unfilled-rectangular are excluded. In this thesis, the convergence consideration is that the deviation of half-power beam width of the antenna is less than 0.5 degree which is small enough. Apparently, the number of summation m and n should be larger (m = 7 and n = 1) for the shorter c, due to the influence of the higher order modes. The number of summation m and n will be decreased to 1 and 0 respectively for the larger c, because the higher order modes are reduced rapidly. For the dominant mode (m = 1 and n = 0), the magnitude of current densities keeps almost constant (see Fig. 2.6). Thus, it is found that m = 7 and n = 1 will be used for all ring lengths. These values are used to obtain the characteristics of the antenna that are explicitly expressed hereafter.

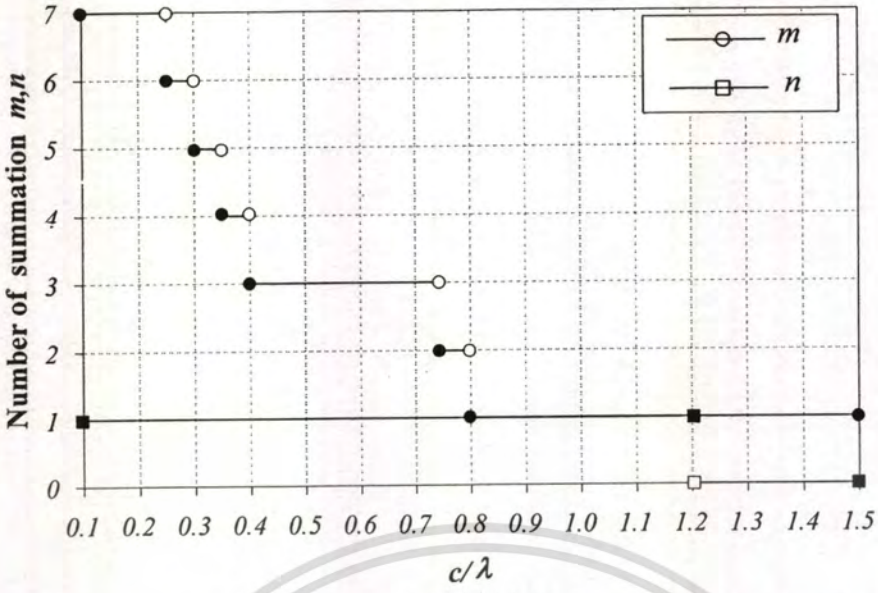

Fig. 2.2 The number of summation m and n for various ring lengths.

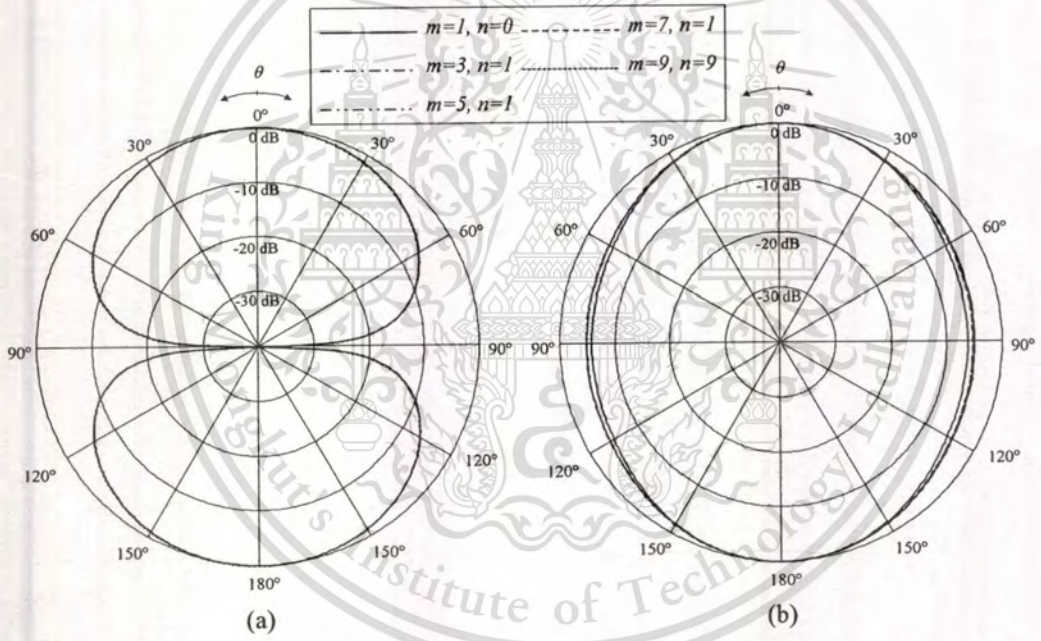

Fig. 2.3 Radiation pattern for various m and n ($c = 0.01\lambda$): (a) yz-plane (b) xz-plane.

To ensure that the number of summation m and n is valid, Fig. 2.3 shows the radiation patterns of the antenna in yz- and xz-planes for various numbers of summation m and n. It is obvious that by using the number of summation $m \geq 7$ and $n \geq 1$, the radiation patterns are nearly identical in which the different half-power beamwidth between the next mode number is less than 0.5 degree. Looking at the total fields as shown in (2.35) and (2.36), it is obvious that the radiation characteristics of the antenna depend on the following parameters, i.e., ring width (a), ring height (b), ring length (c), probe length (l) and probe offset position (s). In this

chapter, the initial probe length is 0.25λ for the reason of impedance matching. Since the cross-section of the antenna is the same as a rectangular waveguide, in this circumstance the ring width and ring height are chosen to be the dimension of a standard waveguide operated at the dominant mode. Thus, the ring width of a, and ring height of $b = a/R$ are selected, where R is the ratio of a/b and $R \geq 1$; in this thesis $R = 2$ is used. The cut-off wavelength is obtained from [31]

$$\lambda_c = \frac{2\pi}{\sqrt{\left(\frac{m\pi}{a}\right)^2 + \left(\frac{n\pi}{b}\right)^2}}. \tag{2.47}$$

Thus, a choice of TE_{10} mode is restricted in the range of $\frac{\lambda}{2} < a < \lambda$. Fig. 2.4 shows the field distributions inside a probe-excited rectangular ring antenna for various ring widths. It is found that the TE_{10} mode is provided when a is in the range of $\lambda/2 < a < \lambda$. For $a > \lambda$, field with higher order modes is achieved. Therefore, for choosing a, it is noted that a should be far away from the upper limit (which is λ) to avoid higher modes. Thenceforth, $a = 0.70\lambda$ and $b = 0.35\lambda$ are selected, and these values are fixed.

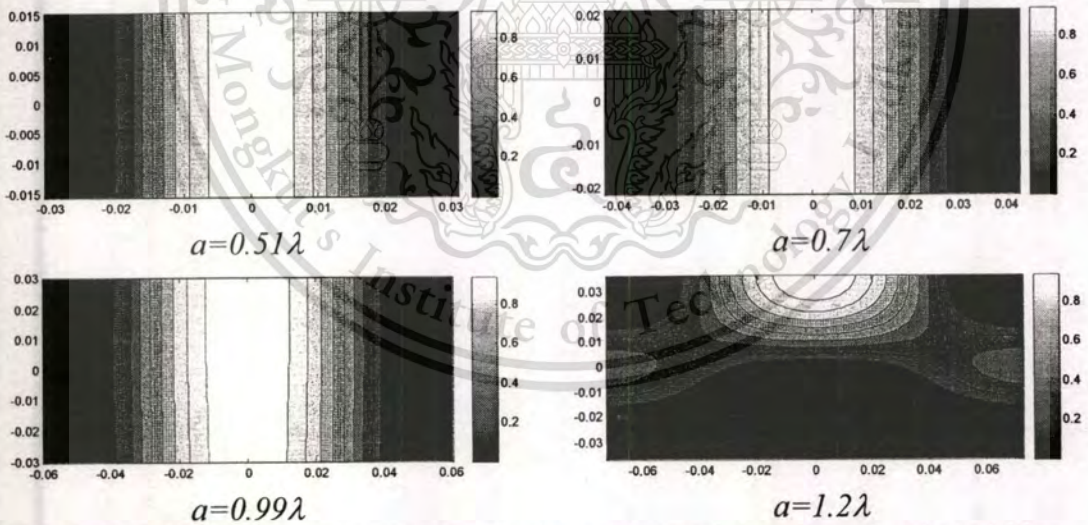

Fig. 2.4 Field distributions inside the rectangular ring for various the ring widths when $b = 0.35\lambda$ and $c = 1.5\lambda$.

In addition, using the total field from the summation of (2.20)-(2.22) and (2.30)-(2.32), the field distributions inside the probe-excited rectangular ring antenna are also plotted for various distance further from the probe excitation z_s (where probe is located at the position of ($x = 0$, $y = -b/2$, $z = 0$) and $z_s = c/2$) as shown in Fig. 2.5.

Apparently, fields at the aperture contain several modes in the vicinity of probe excitation, and the evanescent waves of the higher order modes still have a significant level. At the distance of aperture further from the probe, the evanescent waves of higher order modes are weak, while the TE_{10} mode has been strongly influenced as shown in Fig. 2.5. The strengthen field of each mode in the rectangular ring will be shown next.

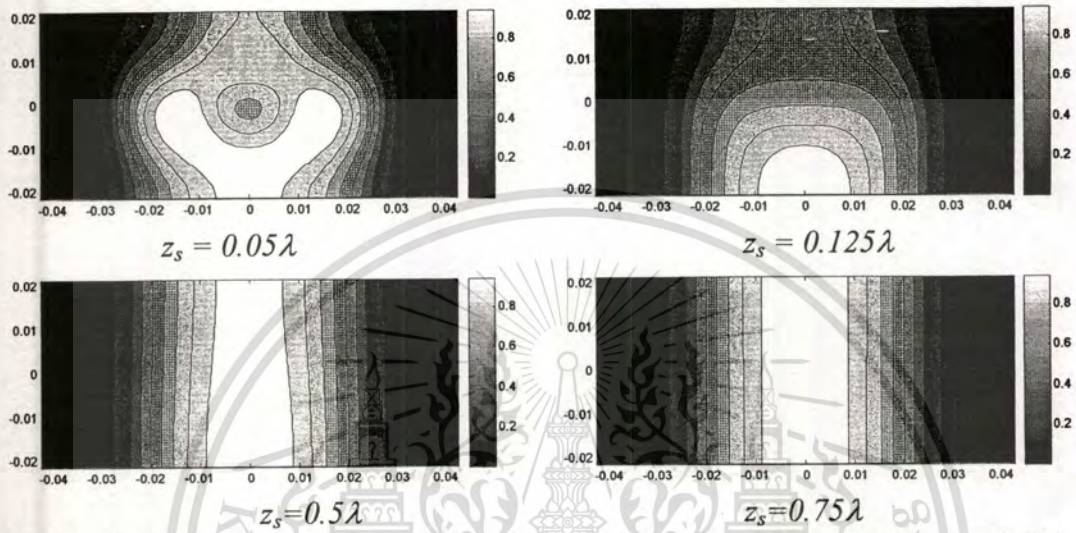

Fig. 2.5 Field distributions inside the rectangular ring for various z_s when $a = 0.70\lambda$ and $b = 0.35\lambda$.

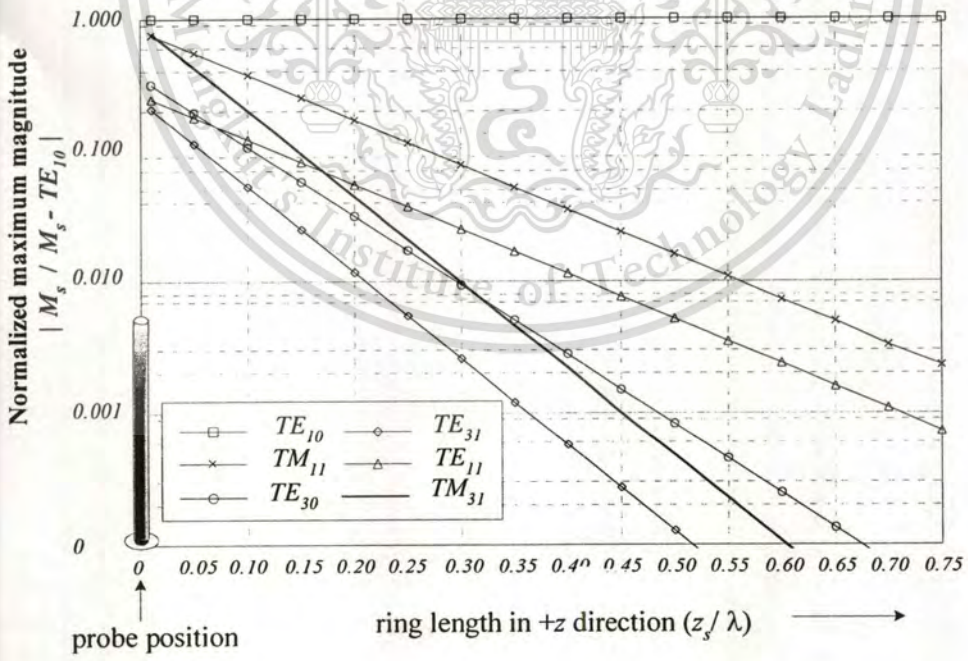

(a)

Fig. 2.6 Normalized magnitudes of M_s and ηJ_s for various aperture distances z_s (where probe is located at $(x = s = 0, y = -b/2, z = 0)$): (a) M_s (b) ηJ_s.

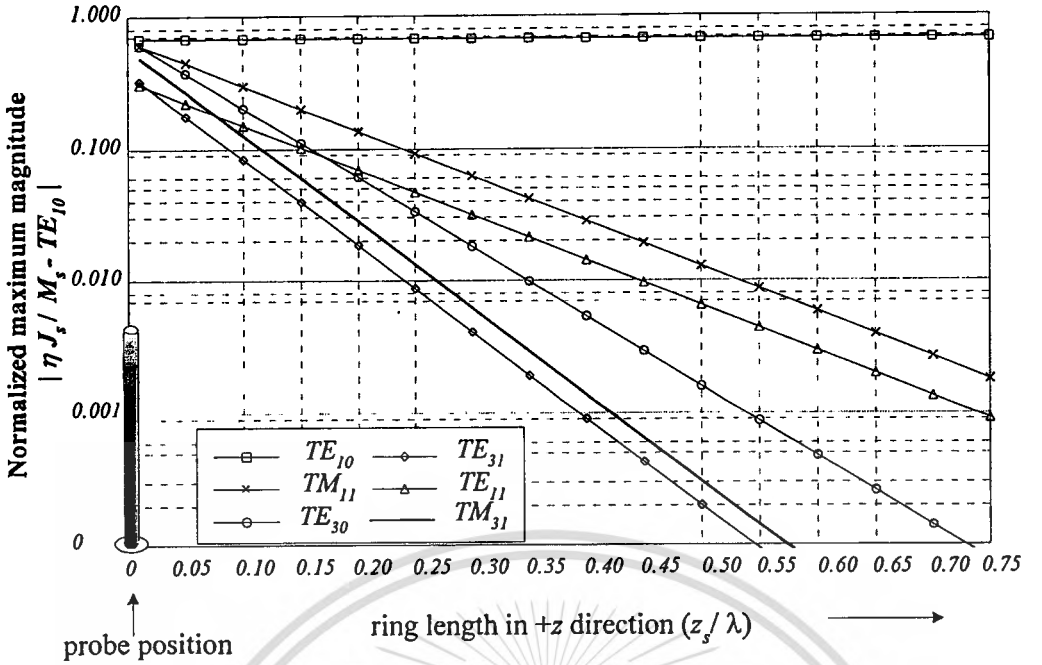

(b)

Fig. 2.6 Normalized magnitudes of M_s and ηJ_s for various aperture distances z_s (where probe is located at $(x = s = 0, y = -b/2, z = 0)$): (a) M_s (b) ηJ_s (cont.).

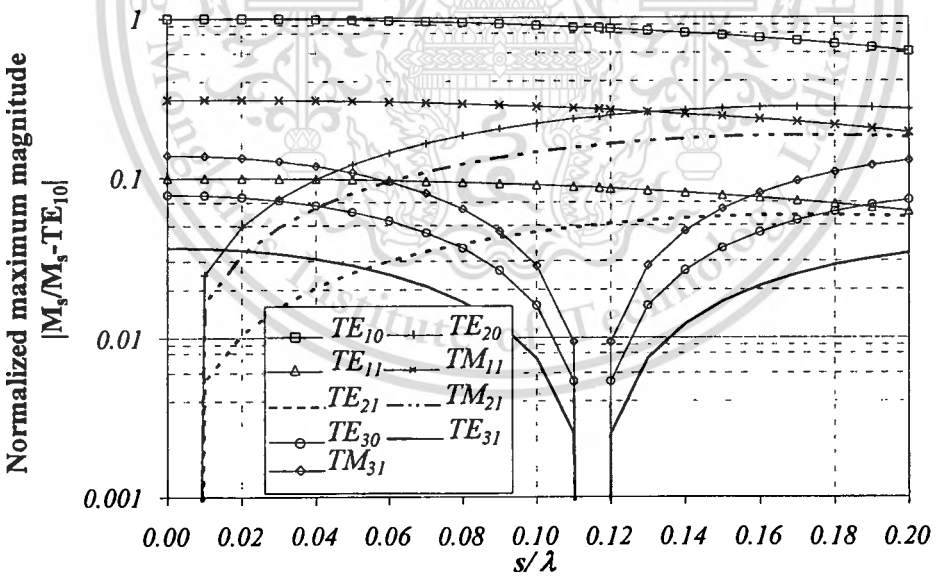

(a)

Fig. 2.7 Normalized magnitudes of M_s and ηJ_s for various s (where probe is located at $(x = s, y = -b/2, z = 0)$: (a) M_s (b) ηJ_s.

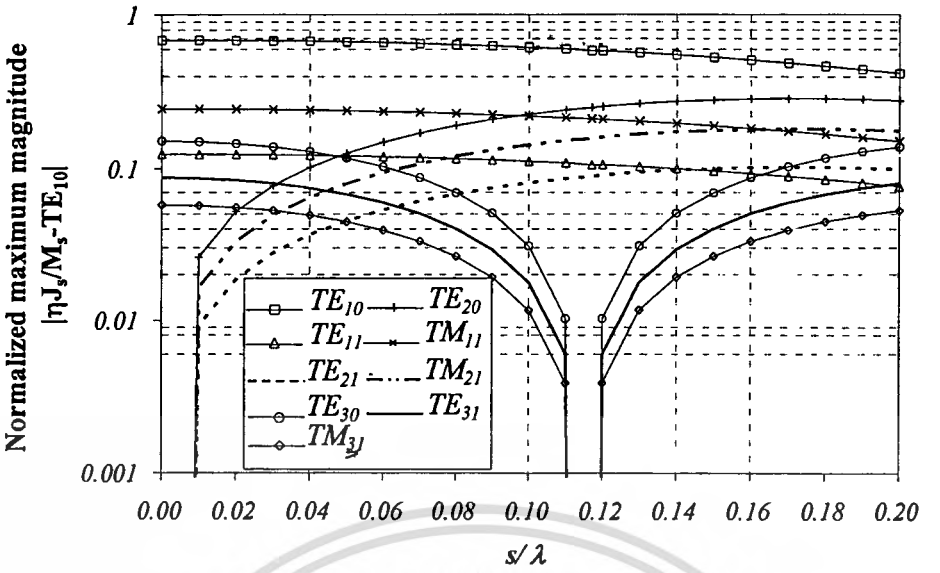

(b)

Fig. 2.7 Normalized magnitudes of M_s and ηJ_s for various s (where probe is located at ($x = s, y = -b/2, z = 0$): (a) M_s (b) ηJ_s (cont.).

Following (2.20)-(2.25) and (2.30)-(2.34), the equivalent current densities of the antenna are determined. It is revealed that a short ring length contains several modes in the vicinity of the probe and the evanescent waves of the higher order modes near the probe have been strong at the aperture as shown in Fig. 2.6. Furthermore, the TE_{10} mode keeps the constant value for any z_s (where z_s is the distance of $c/2$ away from the probe position), whereas the higher order modes are lower as the further distance to the aperture. They reduce rapidly when $z_s = 0.75\lambda$. In addition, it is found that some modes do not exist especially the number of modes with even m, that is different from those in the rectangular waveguide [31]. However, the number of modes with even m are induced and strengthen when probe is shifted from the center ($x = s = 0, y = -b/2, z = 0$) whereas the number of modes with odd m are decreased as shown in Fig. 2.7. The number of modes with odd m is vanished at $s = 0.175\lambda$ and then it is increased again. The dominant mode TE_{10} is still stronger than the others. It should be noted that modal distributions inside a probe-excited rectangular ring antenna have been strongly influence on the input impedance of the proposed antenna shown in the next chapter.

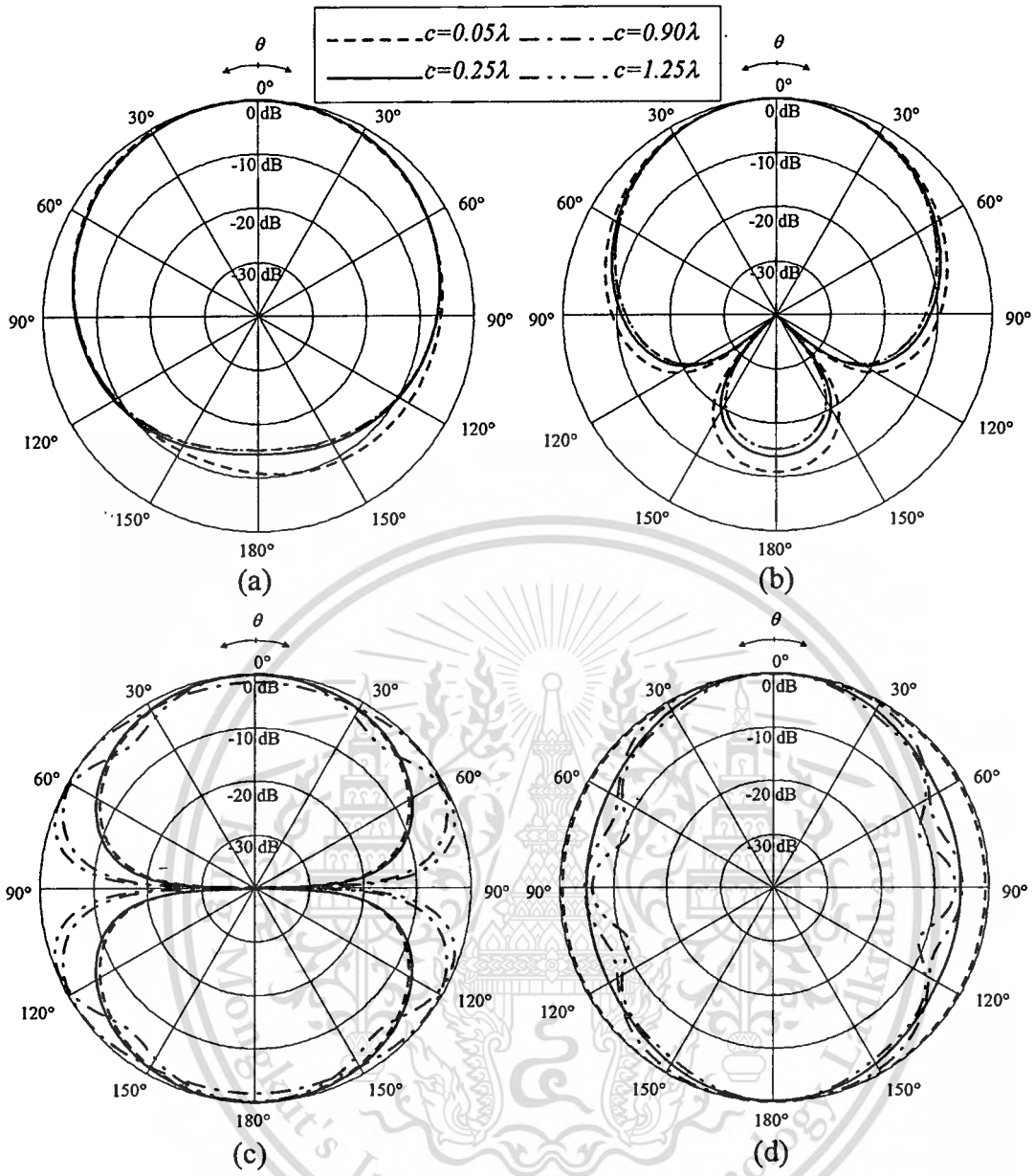

Fig. 2.8 Radiation pattern for various c: (a) yz-plane of $+z$ aperture (b) xz-plane of $+z$ aperture (c) yz-plane of two apertures (d) xz-plane of two apertures.

According to (2.35)-(2.46) in Section 2.2, the electric fields are plotted as a function of c as shown in Fig. 2.8. The radiation pattern of a single aperture in $+z$ and $-z$ directions at $z_s = \pm c/2$ is shown under the condition that, field radiates only toward $+z$ and $-z$ directions and there is no coupling between the apertures. Then, radiation pattern from two apertures is displayed from the combination of a single aperture in $+z$ and $-z$ directions with the same phase. On the other hand, the antenna acts as the array of two apertures separated by the distance between the apertures (the ring length), that contribute to the radiation pattern. As the results, the bidirectional pattern

can be produced. It is observed that, the radiated field for the c shorter than 0.05λ is the same as the radiation pattern of a dipole antenna. Moreover, by increasing c, the pattern in yz-plane is wider and then split. The side lobe formed on each side of the main lobe is the result of ring length greater than λ. Then it becomes a bidirectional with side lobes. The xz-plane pattern has wider beam for the shorter c because the aperture separation affects the radiation patterns. In addition, the yz-plane pattern has null and the xz-plane pattern broadens at $\theta = 90^\circ$ due to the effect of the ring edge.

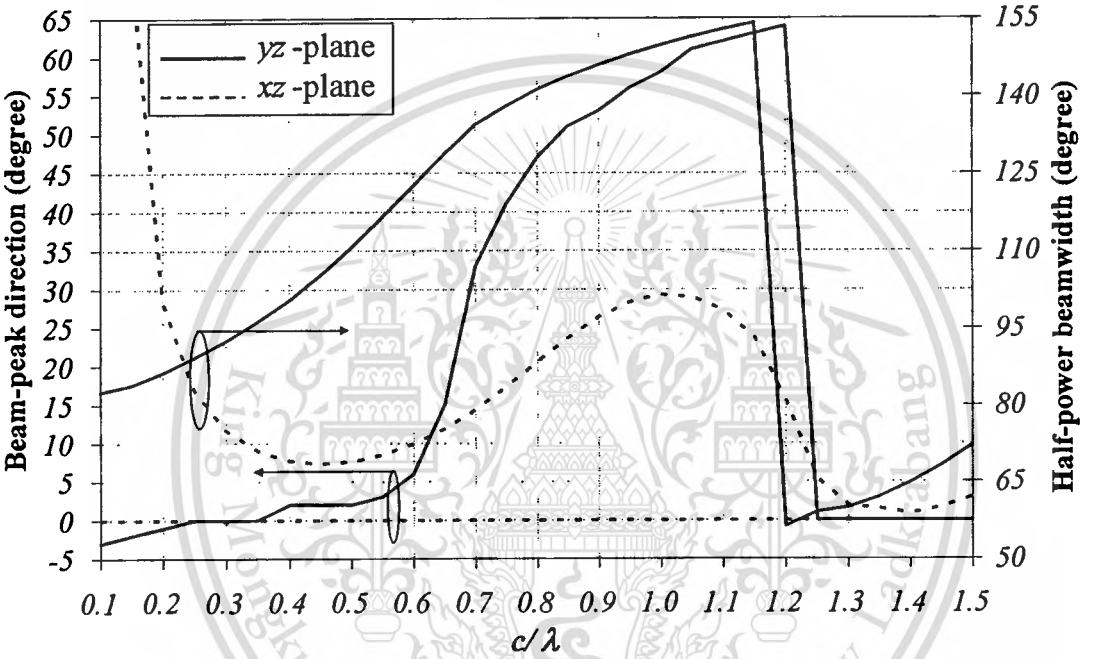

Fig. 2.9 Beam-peak direction and half-power beamwidth for various ring lengths.

In addition, the beam-peak direction of yz-plane will be slightly tilted from z axis ($\theta = 0^\circ$ and $\theta = 180^\circ$) due to the influence of asymmetrical probe position at the upper and lower side (i.e., it is located at the lower side) as shown in Fig. 2.9. For $0.1\lambda \le c \le 1.5\lambda$, it is found that a bidirectional pattern is obtained at $c \le 0.6\lambda$ and occurred again with existed side lobe at $c \ge 1.25\lambda$ (for the beam peak directs +5 and -5 degrees tilted from z axis). Furthermore, in Fig. 2.9, the half-power beamwidth in yz-plane and the xz-plane have the opposite curve, viz., a wider beamwidth and a narrower beamwidth in yz- and xz-planes respectively, as the longer ring length until at $c = 1.25\lambda$ (which the bidirectional pattern with side lobes is occurred), then they

are increased. These result to the directivity of the antenna that will be then described. Note that the narrow beamwidth is required for the high directivity.

The directivity is a figure of merit that quantifies the antenna directive properties comparing with an isotropic antenna. The maximum directivity is defined as the maximum radiation intensity of that antenna (U_{max}) over the radiation intensity of isotropic radiator ($P_{rad}/4\pi$). The high radiation intensity with the low radiated power is required to enhance directivity. The maximum radiation intensity is obtained from combining of the maximum amplitude of electric field that radiates from $+z$ and $-z$ apertures as

$$\begin{aligned}\left|\overline{E}\right|^2 &= \left|E_{\theta,+z}+E_{\theta,-z}\right|^2+\left|E_{\phi,+z}+E_{\phi,-z}\right|^2 \\ &= \left(\left|E_{\theta,+z}\right|^2+\left|E_{\theta,-z}\right|^2+2\left|E_{\theta,+z}\right|\left|E_{\theta,-z}\right|\cos\left(\xi_{\theta,+z}-\xi_{\theta,-z}\right)\right) \\ &+\left(\left|E_{\phi,+z}\right|^2+\left|E_{\phi,-z}\right|^2+2\left|E_{\phi,+z}\right|\left|E_{\phi,-z}\right|\cos\left(\xi_{\phi,+z}-\xi_{\phi,-z}\right)\right).\end{aligned} \tag{2.48}$$

The ring length that provides the maximum directivity must be clarified. Figure 2.8 shows the maximum directivity as a function of ring length when $l = 0.25\lambda$, $a = 0.70\lambda$ and $b = 0.35\lambda$. In Fig. 2.10 (a), it is found that the maximum radiation intensity is provided at $\theta = 0^\circ$ and $\phi = 90^\circ$ by combining the square of magnitude of electric field aperture at $+z$ ($\left|E_{\theta,+z}\right|^2$) and $-z$ directions ($\left|E_{\theta,-z}\right|^2$) respectively, with the phase difference ($\xi_{+z}-\xi_{-z}$) between $+z$ and $-z$ apertures, as defined by subscript $+z$ and $-z$, respectively. Equation (2.48) shows that E_ϕ is null in this direction. Therefore, only a component of E_θ is shown in Fig. 2.10 (a). The phase-difference has more impact on radiation intensity. Nevertheless, at the maximum intensity ($c = 0.5\lambda$), the radiated power is rather high. Hence the maximum directivity does not occur as shown in Fig. 2.10(b). Furthermore, the mode distributions inside the ring also affect to the directivity; i.e. the shorter c provides the high magnitude of higher order mode, and the directivity is decreased. Furthermore, the aperture separation also influences to the directivity. As the results, the maximum directivity of 4.60 dBi for $c = 1.45\lambda$ is achieved because this length provides the narrower beamwidth with existed side lobe. For the bidirectional pattern with no side lobe, the ring length of 0.4λ provides the maximum directivity of 4.43 dBi.

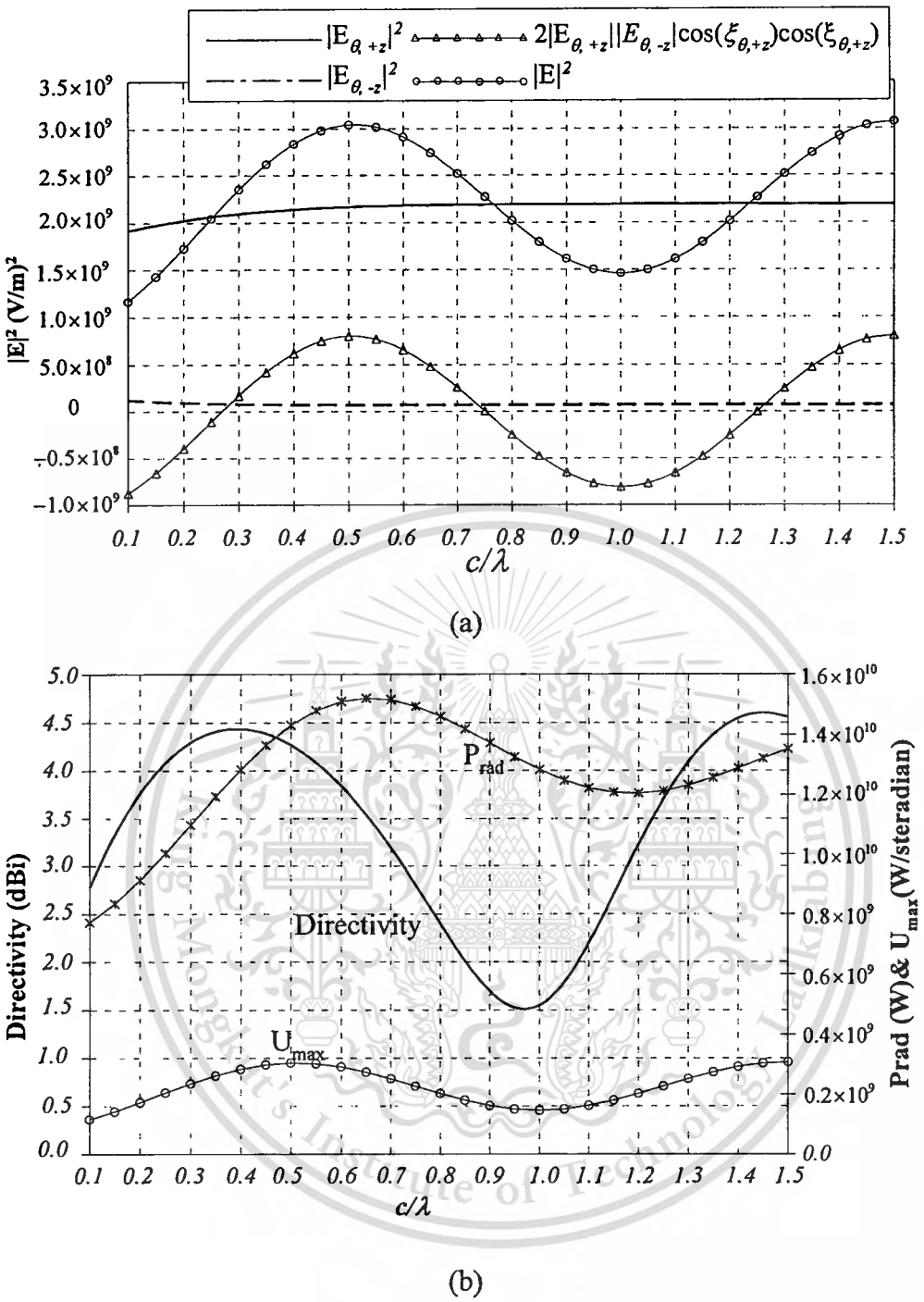

Fig. 2.10 Directivity, radiated power and radiation intensity for various ring lengths: (a) Magnitude of radiated field (b) Directivity, P_{rad} and U_{max}.

2.4 Summary

This chapter presents the investigations of a bidirectional antenna using a probe-excited rectangular ring by applying the dyadic Green's function approach. The analysis begins with the field derivation of a probe-excited rectangular ring which is considered as a part of rectangular waveguide truncated at the ends by the aperture. It

is found from the closed-form solution that the antenna characteristics depend on the ring width, ring height, ring length, length probe and probe position. For the derivations, the electromagnetic fields are expressed as a superposition of the field from two apertures, by neglecting the mutual coupling and disregard the diffraction at the edge of the antenna. The effects of the probe on the features of rectangular ring are illustrated as normalized equivalent magnetic and electric current densities with respect to the equivalent magnetic current of the dominant mode (TE_{10}). It is obvious that the number of modes with even m do not exist when the excited-probe position is at the center ($x = s = 0$, $y = -b/2$, $z = 0$), and they are induced and strengthen when probe is shifted from the center ($s \neq 0$). In addition, the radiation pattern becomes bidirectional pattern for the appropriated ring length c from 0.10λ to 0.65λ and occurred again with the side lobe when $c \geq 1.25\lambda$. Furthermore, the beam-peak direction in yz-plane is slightly tilted from z-axis because of an asymmetrical view in this plane; probe is located at the lower side of ring. In xz-plane, it always directs in $+z$ and $-z$ directions for any ring length of interest due to the symmetrical geometry in this plane. To obtain the antenna parameters, the ring width and ring height are selected as same dimensions of rectangular waveguide operated at the dominant mode. The ring length is varied to achieve the optimum radiation characteristics. Furthermore, the polarization of this antenna at the directions along the street cell ($+z$ and $-z$ directions) is linear because there is only an elevation component of electric field. Since, the results in this chapter are obtained under the assumption of current. Therefore, impedance characteristics are less correction. In the next chapter, impedance characteristics are investigated by using the Moment Methods, which use more accuracy current in the analysis compared to the dyadic Green's function approach that used in this chapter. The validity of this approach is verified by the measurement in chapter 5.

CHAPTER 3
ANALYSIS OF IMPEDANCE CHARACTERISTIC BY MOMENT METHOD WITH RWG BASIS FUNCTIONS

3.1 Introduction

The art of electromagnetic engineering design partly relies on the ability to properly model the physical structure under consideration. Electromagnetic field models are predominantly used by antenna and microwave engineering. The analysis starts from the physical structure (i.e., the geometry and electrical properties of materials involved), and it gives a full insight into the electrical properties of devices and circuits (including propagation, radiation, parasitic effects, etc.). Most electromagnetic field problems do not have an analytical solution; therefore a numerical approach is required. Various numerical techniques have been developed to carry out the electromagnetic field simulation [14]-[21]. The most notable approaches for treating that problem have used integral solution formulations in conjunction with the Moment Methods [32].

Generally, the integral equations are categorized as electric field integral equation (EFIE) and magnetic field integral equation (MFIE) [33]. The EFIE has advantage of being applicable to both open and closed bodies, whereas the MFIE applies only to closed surface. The body surfaces in these approaches is generally modeled either as a wire mesh called wire grid model or as a surface partitioned into smooth or piecewise-smooth patches called surface patches model. The wire-grid modeling approach has been remarkably successful in treating many problems, particularly in those requiring the prediction of far field quantities such as radiation pattern [25]. It also has the advantage that all numerically computed integrals in the moment matrix are only one dimension. However, it is not well suited for calculating near field and surface quantities such as surface current and input impedance. Some of problems encountered include the presence of fictions loop currents in the solution, ill-conditioned in the matrices and incorrect currents at the cavity resonant frequency of the scatter and difficulties in interpreting computed wire currents and relating them to equivalent surface currents. Most of these difficulties can be either completely or partially overcome by surface patch approaches [25]. Several approaches to surface patch modeling have been reported in the literature [34]-[38]. In [37] stated that the use of rectangular patches limits the approaches to structures with curvature

in one dimension only. For modeling arbitrarily shaped surfaces, planar triangular patch models are particularly appropriate. Some of the advantages of the triangular patches are capable of accurately conforming to any geometrical surface or boundary, the patch scheme is easily specified for computer input, and a varying patch density can be used according to the solution required in the surface current. Although planar quadrilateral (non rectangular) patches share some of these feature, it is difficult to construct basis functions defined on them which are free of line charges. Furthermore, the vertices of planar quadrilaterals cannot be independently specified; a restriction that is a sever inconvenience to the modeler. In this thesis, the RWG basis function using triangular patches, which is widely used in MoM analysis [25], [38], is applied.

This chapter is organized as follows. The electrical field formulations are expressed in Section 3.2. In Section 3.3, antenna structure and numerical results are shown. Finally, summary is reported in Section 3.4.

3.2 Electric Field Formulations

In this section an integral equation for the surface current induced on the conducting scatterer deriving from boundary conditions on electric field is shown. To solve the integral equation by moment method, a set of basis function and testing function is used to derive the element of moment matrix.

3.2.1. Electric Field Integral Equation

Fig. 3.1 shows the equivalent source for the electric and magnetic fields out side S. Let S denote the surface of an open or closed surface perfectly conducting scatterer with unit normal $\hat{n}$. An electric field $\bar{E}^i$, defined to be the field due to an impressed source in the absence of the scatterer, is incident and induces surface current $\bar{J}$ (with may regard to the equivalent electric ($\bar{J}_{es}$) and magnetic surface currents ($\bar{J}_{ms}$)) on S. If S is open, we regard $\bar{J}$ as the vector sum of the surface currents on opposite sides of S; hence the normal component of $\bar{J}$ must vanish on boundary of S. The scattered electric field $\bar{E}^s$ can be computed from the surface current by

$$\bar{E}^s = -j\omega\bar{A} - \nabla\Phi \tag{3.1}$$

with the magnetic vector potential defined as

$$\bar{A}(\bar{r}) = \frac{\mu}{4\pi}\int_s \bar{J}\frac{e^{-jkR}}{R}dS' \tag{3.2}$$

and the scalar potential as

$$\Phi(\bar{r}) = \frac{1}{4\pi\varepsilon}\int_s \sigma\frac{e^{-jkR}}{R}dS'. \tag{3.3}$$

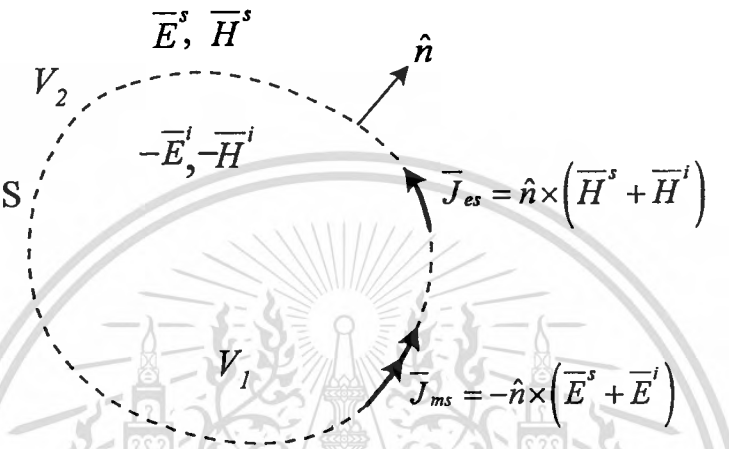

Fig. 3. 1 The equivalent source for the electric and magnetic fields out side S.

A harmonic time dependence $e^{j\omega t}$ is assumed and suppress, $k = \omega\sqrt{\mu_0\varepsilon_0} = 2\pi/\lambda$, when λ is the free space wavelength. The permeability and permittivity of the surrounding medium are μ and ε, respectively, and $R = |\bar{r} - \bar{r}'|$ is the distance between an arbitrarily located observation point $\bar{r}$ and a source point $\bar{r}'$ on S. Both $\bar{r}$ and $\bar{r}'$ are defined with respect to a global coordinate origin. The surface charge density σ is related to the surface divergence of $\bar{J}$ through the equation of continuity,

$$\nabla_s \cdot \bar{J} = -j\omega\sigma. \tag{3.4}$$

An integrodifferential equation for $\bar{J}$ is derived by enforcing the boundary condition $\hat{n}\times(\bar{E}^i + \bar{E}^s) = 0$ on S, then

$$-\bar{E}^i_{\tan} = \left(-j\omega\bar{A} - \nabla\Phi\right)_{\tan},\ \bar{r} \text{ on } S \tag{3.5}$$

Equation (3.5), with (3.2)-(3.4), constitutes the electric field integral equation. Note that the presence of derivatives on the current in (3.4) and on the scalar potential in (3.5) suggests that care should be taken in selecting the expansion functions and test procedure in the MoM.

3.2.2. Basis Function

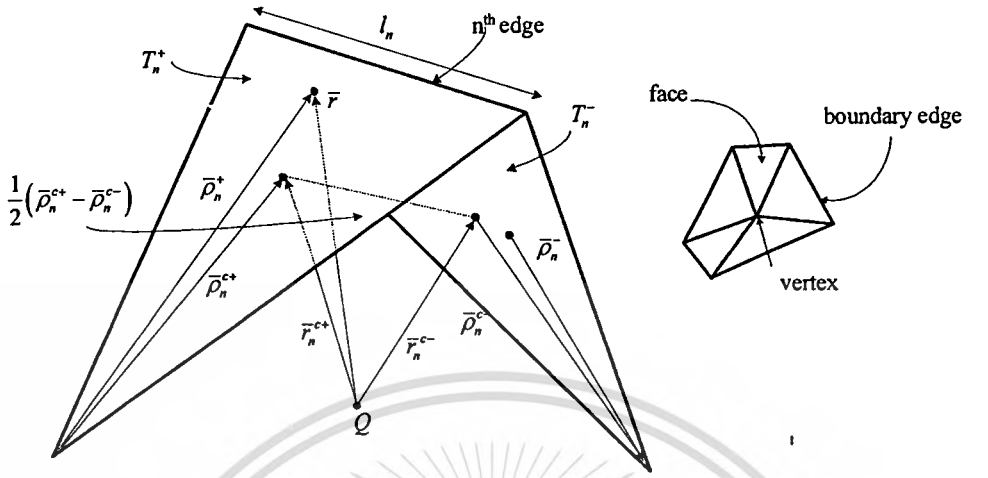

Fig. 3. 2 Triangle pair and geometrical parameters associated with interior edge.

In this section, a set of RWG basis function, which is suitable for EFIE and triangular patch modeling, is introduced. To assume that a suitable triangulation, defined in terms of an appropriate set of faces, edges, vertices, and boundary edges, as illustrated in Fig. 3.2, has been found to approximate S. It is convenient to start by noting that each basis function is to be associated with an interior edge (i.e., non-boundary edge) of the patch model, and it is to vanish everywhere on S except in the two triangles attached to that edge. Fig. 3.3 shows two such triangles, T_n^+ and T_n^-, corresponding to the *n*th edge of a triangulated surface modeling a scatterer. Points in T_n^+ may be designated either by the position vector $\bar{r}$ defined with respect to Q, or by a position vector $\bar{\rho}_n^+$ defined with respect to free vertex of T_n^+. Similar remarks apply to the position vector $\bar{\rho}_n^-$ except that it is directed toward the free vertex of T_n^-. The plus or minus designation of the triangles is determined by the choice of a positive current reference direction for the *n*th edge, the reference is assumed to be from T_n^+ to T_n^-. The vector basis function associated with the *n*th edge as

$$\bar{f}_n(\bar{r}) = \begin{cases} (l_n / 2A^+)\bar{\rho}_n^+(\bar{r}), & \bar{r} \text{ in } T_n^+ \\ (l_n / 2A^-)\bar{\rho}_n^-(\bar{r}), & \bar{r} \text{ in } T_n^- \\ 0, & \text{otherwise} \end{cases} \tag{3.6}$$

where l_n is the length of the edge, $\bar{\rho}_n^{\pm}$ is the vector between the free vertex points, and $\bar{A}_n^{\pm}$ is the area of triangle $T_n^{\pm}$. (Note that, followed throughout this chapter, the subscripts refer to edges while superscripts refer to faces.) The basis function $\bar{f}_n$ is used to approximate represent the surface current. Some properties which make basis function $\bar{f}_n$ uniquely suited to this role are shown as below [37].

(1) The current has no component normal to the boundary (which excludes the common edge) of the surface formed by the triangle pair T_n^+ to T_n^-, and hence no line charges exist along this boundary.

(2) The component of current normal to the *n*th edge is constant and continuous across the edges as maybe seen in Fig. 3.3, which shows that the normal component of $\bar{\rho}_n^{\pm}$ along edge *n* is just the height of triangle $T_n^{\pm}$, with edge *n* as the base and the height expressed as $2A_n^{\pm}/l_n$. This latter factor normalizes $\bar{f}_n$ in (2.6) such that its flux density normal to edge *n* is unity, ensuring continuity of current normal to the edge. This result, together with (l), implies that all edges of T_n^+ and T_n^- are free of line charges.

(3) The surface divergence of $\bar{f}_n$, which is proportional to the surface charge density associated with the basis element, is

$$\nabla_s \cdot \bar{f}_n = \begin{cases} l_n / A_n^+, & \bar{r} \text{ in } T_n^+ \\ -l_n / A_n^-, & \bar{r} \text{ in } T_n^- \\ 0 & \text{otherwise,} \end{cases}$$

since the surface divergence in $T_n^{\pm}$ is $\left(\pm 1/p_n^{\pm}\right)\partial\left(p_n^{\pm}\bar{f}_n\right)/\partial p_n^{\pm}$. The charge density is thus constant in each triangle, the total charge associated with the triangle pair T_n^+ and T_n^- is zero, and the basis functions for the charge evidently have the form of pulse doublets.

(4) The moment of $\bar{f}_n$ is given by $\left(A_n^+ + A_n^-\right) f_n^{avg}$ where

$$\left(A_n^+ + A_n^-\right) f_n^{avg} \equiv \int_{T_n^+ + T_n^-} \overline{f}_n ds$$
$$= \frac{l_n}{2}\left(p_n^{c_0^+} + p_n^{c_0^-}\right)$$

and $p_n^{c_0^\pm}$ is the vector between the free vertex and the centriod of $T_n^\pm$ with $p_n^{c_0^-}$ directed toward an $p_n^{c_0^+}$ directed away from the vertex.

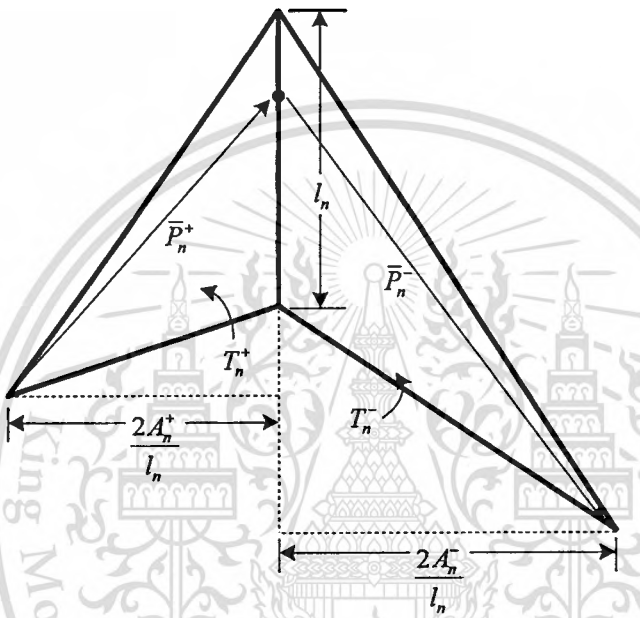

Fig. 3.3 Geometry for construction of component of basis function normal edge.

In terms of RWG basis function $\overline{f}_n$ [39], the surface electric current density $\overline{J}$ on the metal surface divided into triangular patches is given inform

$$\overline{J} \cong \sum_{n=1}^{N} I_n \overline{f}_n(\overline{r}) \tag{3.7}$$

where N is the number of interior (non-boundary) edges. Since a basis function is associated with each non-boundary edge of the triangulated structure, up to three basis functions may have nonzero values within each triangular face. But at a given edge only the basis function associated with that edge has a current component normal to the edge; all other basis currents in adjacent faces are parallel to the edge. Furthermore, since the normal component of $\overline{f}_n$ at the nth edge is unity, each coefficient I_n in (3.7) may be interpreted as the normal component of current density flowing past the nth edge. Also, the basis functions are independent in each triangle

since the current normal to the nth edge, I_n in (3.7), is an independent quantity. At surface boundary edges, the sum of normal components of current on opposite sides of the surface is canceled because of current continuity. Therefore, it is neither defined nor included in (3.7) contributions from basis function associated with such edges.

3.2.3. Testing Function

The next step in the MoM is to select a testing function. Galekin solution, which, basis function and testing function are identical [31], is chosen for testing functions. With a symmetric product defined as

$$< \bar{f}, \bar{g} > \equiv \int_S \bar{f} \cdot \bar{g} dS \tag{3.8}$$

(3.5) is tested with $\bar{f}_m$, yielding

$$< \bar{E}, \bar{f}_m > \; = j\omega < \bar{A}, \bar{f}_m > + < \nabla\Phi, \bar{f}_m > \tag{3.9}$$

If one makes use of surface vector calculus identity and properties of $\bar{f}_m$ at the edges of S, the last term in (3.9) can be rewritten as

$$< \nabla\Phi, \bar{f}_m > = -\int_S \Phi \nabla_s \cdot \bar{f}_m \, dS \tag{3.10}$$

From (3.6), the right hand side (RHS) of (3.10) may be written and approximated as follows:

$$\int_S \Phi \nabla_s \cdot \bar{f}_m \, dS = l_m \left(\frac{1}{A_m^+} \int_{T_m^+} \Phi \, dS - \frac{1}{A_m^-} \int_{T_m^-} \Phi \, dS \right) \cong l_m \left[\Phi(\bar{r}_m^{c_0+}) - \Phi(\bar{r}_m^{c_0-}) \right] \tag{3.11}$$

In (3.11) the average of Φ over each triangle is approximated by the value of Φ at the triangle centroid. With similar approximation, the vector potential (the first term of RHS of (3.9)) and incident field terms (the left hand side (LHS) of (3.9)) may be written as

$$\left\langle \begin{Bmatrix} \bar{E}^i \\ \bar{A} \end{Bmatrix}, \bar{f}_m \right\rangle = l_m \left[\frac{1}{2A_m^+} \int_{T_m^+} \begin{Bmatrix} \bar{E}^i \\ \bar{A} \end{Bmatrix} \cdot \bar{\rho}_m^+ \, dS + \frac{1}{2A_m^-} \int_{T_m^-} \begin{Bmatrix} \bar{E}^i \\ \bar{A} \end{Bmatrix} \cdot \bar{\rho}_m^- \, dS \right]$$

$$\cong \frac{l_m}{2} \left[\begin{Bmatrix} \bar{E}^i(\bar{r}_m^{c_0+}) \\ \bar{A}(\bar{r}_m^{c_0+}) \end{Bmatrix} \cdot \bar{\rho}_m^+ + \begin{Bmatrix} \bar{E}^i(\bar{r}_m^{c_0-}) \\ \bar{A}(\bar{r}_m^{c_0-}) \end{Bmatrix} \cdot \bar{\rho}_m^- \right] \tag{3.12}$$

where the integral over each triangle is eliminated by approximating $\bar{E}^i$ (or $\bar{A}$) in each triangle by its value at the triangle centroid. From (3.10)-(3.12), (3.9) now becomes

$$j\omega l_m\left[\bar{A}(\bar{r}_m^{c_0+})\cdot\frac{\bar{\rho}_m^{c+}}{2}+\bar{A}(\bar{r}_m^{c-})\cdot\frac{\bar{\rho}_m^{c-}}{2}\right]+l_m\left[\Phi(\bar{r}_m^{c_0-})-\Phi(\bar{r}_m^{c_0+})\right]=l_m\left[\bar{E}^i(\bar{r}_m^{c_0+})\cdot\frac{\bar{\rho}_m^{c_0+}}{2}+\bar{E}^i(\bar{r}_m^{c_0-})\cdot\frac{\bar{\rho}_m^{c_0-}}{2}\right] \tag{3.13}$$

which is the equation enforced at each triangle, $m=1, 2, \ldots, N$. The purpose of approximations (3.11)-(3.12) is to eliminate surface integral of the potential quantities allowing a double surface integral to be approximated by a quantity involving a single surface integral in the numerical computation of the moment matrix elements.

3.2.4. Matrix Impedance

Substitution of the current expansion (3.7) into (3.13) yields an $N\times N$ system of linear equations may be written in matrix from as

$$[Z_{mn}][I_n]=[V_m] \tag{3.14}$$

Elements of Z and V are given by

$$Z_{mn}=l_m\left[j\omega\left(\bar{A}_{mn}^{+}\cdot\frac{\rho_m^{c_0+}}{2}+\bar{A}_{mn}^{-}\cdot\frac{\rho_m^{c_0-}}{2}\right)+\Phi_{mn}^{-}-\Phi_{mn}^{+}\right] \tag{3.15}$$

$$V_m=l_m\left(\bar{E}_m^{+}\cdot\frac{\rho_m^{c_0+}}{2}+\bar{E}_m^{-}\cdot\frac{\rho_m^{c_0-}}{2}\right),\ E_m^{\pm}=E^i(r_m^{c_0\pm});\ m=1,2,\cdots,N \tag{3.16}$$

where

$$\bar{A}_{mn}^{\pm}=\frac{\mu}{4\pi}\left[\frac{l_n}{2A_n^{+}}\int_{T_n^{+}}\bar{\rho}_n^{+}\frac{e^{-jkR_m^{\pm}}}{R_m^{\pm}}\,dS'+\frac{l_n}{2A_n^{-}}\int_{T_n^{-}}\bar{\rho}_n^{-}\frac{e^{-jkR_m^{\pm}}}{R_m^{\pm}}\,dS'\right], \tag{3.17}$$

$$\Phi_{mn}^{\pm}=-\frac{\mu}{4\pi j\omega\varepsilon}\left[\frac{l_n}{A_n^{+}}\int_{T_n^{+}}\frac{e^{-jkR_m^{\pm}}}{R_m^{\pm}}\,dS'-\frac{l_n}{A_n^{-}}\int_{T_n^{-}}\frac{e^{-jkR_m^{\pm}}}{R_m^{\pm}}\,dS'\right], \tag{3.18}$$

$$R_m^{\pm}=\left|\bar{r}_m^{c_0\pm}-\bar{r}'\right| \tag{3.19}$$

An antenna is usually fed by a conventional transmission line through two electrically closed terminals. This means that an ideal voltage generator is connected across a gap with a small width, along the antenna. To account for a voltage source instead of an incident wave, a feeding-edge model is introduced. An alternative way is to use a numerical integration over a triangle. The so-called barycentric subdivision [39] of an arbitrary is chosen. Any primary triangle can be divided into 9 equal small sub-triangles by the use of the "one-third" rule. Further assuming, the

integrand is constant with each small triangle. For the simplest way to obtain the current solution in (3.16), the Gaussian elimination [39] is used instead of the matrix inversion.

3.2.5. Input Impedance and Far-Field Parameters

For the model of fed-probe in Fig.3.3, the feeding edge at the junction requires special consideration. There are two edge elements that have the common edge l_n. To separate these two elements, it is convenient to "double" the junction edge, i.e. just repeat it twice in mesh code. The model of delta-function generated is then applied, similar to that for dipole. Since the feeding edge is double, the contribution of each single edge should be taken into account. The input impedance is defined as the ratio of voltage to current at a pair of terminals. Therefore, the antenna impedance is

$$Z_A = \frac{V}{l_{n1} I_{n1} + l_{n2} I_{n2}} \tag{3.20}$$

where indices 1, 2 label two distinct RWG junction elements.

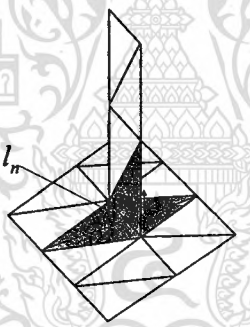

Fig. 3.4 Model of probe feed.

Once the surface currents are known, the electric and magnetic fields everywhere in space can be found, either using surface integrals or elegant dipole model. The dipole model assumes that every RWG edge element behaves like a dipole of constant current, located between the centroids of the triangle adjacent to each edge. The dipole moment, $\bar{m}$, which is the products of an effective dipole current is obtained by integration of the surface current, corresponding to the edge element m, over the element surface, i.e.,

$$\bar{m} = \int_{T_m^+ + T_m^-} I_m \bar{f}_m(\bar{r}) dS = I_m l_m (\bar{r}_m^{c_0-} - \bar{r}_m^{c_0+}) \tag{3.21}$$

where $\bar{f}_m(r)$ is the RWG basis function corresponding to the element m. The surface current coefficient I_m is known from the moment equations. The product of $l_m I_m$ is associated with dipole current, whereas the effective dipole length, l, is given by $\left[\bar{r}_m^{c_0-} - \bar{r}_m^{c_0+}\right]$.

The radiation electric and magnetic fields of an infinitesimal dipole at the point $\bar{r}$ are

$$\bar{E}(\bar{r}) = \frac{\eta}{4\pi}\left((\bar{M}-\bar{m})\left[\frac{jk}{r}+C\right]+2\bar{M}C\right)e^{-jkr} \tag{3.22}$$

$$\bar{H}(\bar{r}) = \frac{jk}{4\pi}(\bar{m}\times\bar{r})Ce^{-jkr} \tag{3.23}$$

Where $\eta = \sqrt{\mu_0/\varepsilon_0}$, $\bar{M} = \frac{(\bar{r}\cdot\bar{m})\bar{r}}{r^2}$, $C = \frac{1}{r^2}\left[1+\frac{1}{jkr}\right]$.

The electric and magnetic fields at a point $\bar{r}$ are obtained as

$$\bar{E}(\bar{r}) = \sum_{m=1}^{M}\bar{E}_m\left(\bar{r} - \frac{1}{2}(r_m^{c_0+} - r_m^{c_0-})\right) \tag{3.24}$$

$$\bar{H}(\bar{r}) = \sum_{m=1}^{M}\bar{H}_m\left(\bar{r} - \frac{1}{2}(r_m^{c_0+} - r_m^{c_0-})\right) \tag{3.25}$$

3.3 Numerical Results

Fig. 3.5 Model of a rectangular ring antenna.

As mentions in chapter 2 that characteristics of the antenna depend on the following parameters, i.e., the ring width (a), the ring height (b), the ring length (c), the probe length (l)

and probe position (s). The ring width of a, and ring height of b are selected as $a = 0.70\lambda$ and $b = 0.35\lambda$ for the condition of dominant mode operation. Accordingly, the antenna characteristics depend on the ring length, probe length and probe position. In the preliminary study, the initial probe length of 0.25λ is selected for the reason of impedance matching (the optimum length is determined later). The antenna structure in Fig. 2.1 can be modeled with a number of triangular patches as shown in Fig. 3.5. The material of the antenna is made by cooper with conductivity of 5.8×10^{7} S/m.

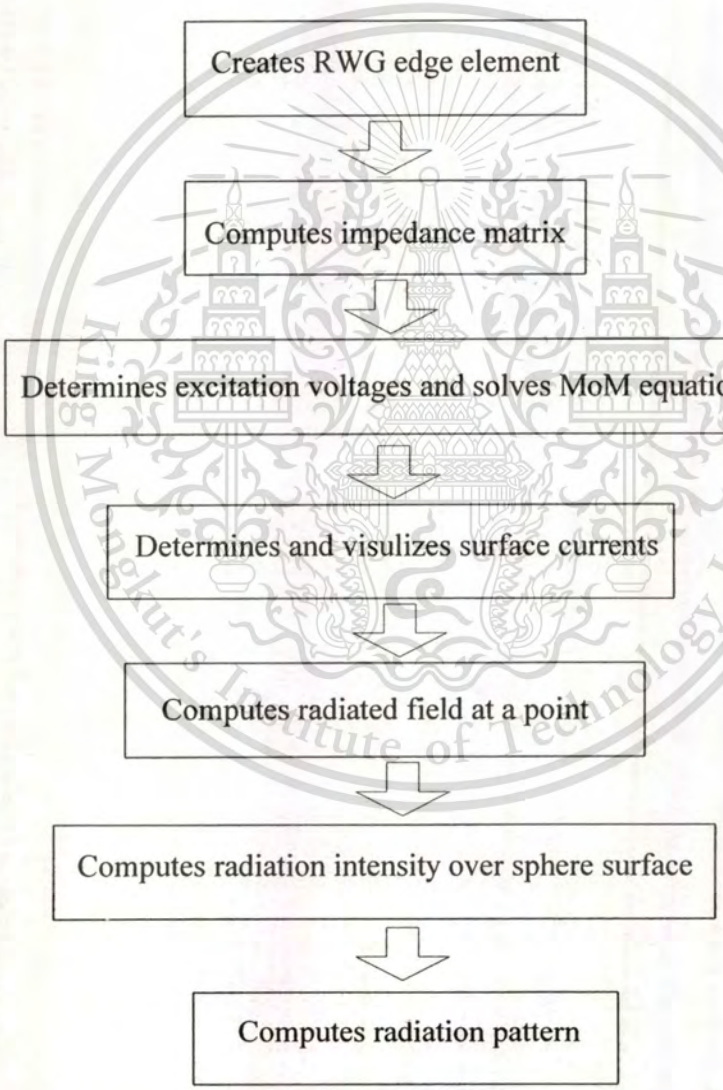

Fig. 3.6 The process for analysis the antenna characteristics using the MoM with RWG basis function.

The process for analysis the antenna characteristics by using the MoM with RWG basis function programming by Matlab7 is shown in Fig. 3.6. The antenna structure is firstly created. Actually, there are several ways of doing so by using Matlab. One way is the use of the built-in mesh generator of the Matlab PDE toolbox. This mesh generator creates planar structures of any (intercepting) rectangles, polygons and circulars, using the convenient graphical user interface (GUI). However, in this thesis, the Delaunay triangulation is applied to build the antenna structure, using Matlab function delaunay. The advantage of this approach is that the PDE toolbox does not needed, and the arbitrary 3D antenna surface and volume meshes can be created. Then, the impedance matrix is determined using the matrix inversion. Consequently, the electric currents flowing on the antenna surface, the near and far fields of the antenna including its radiation patterns and gain can be computed.

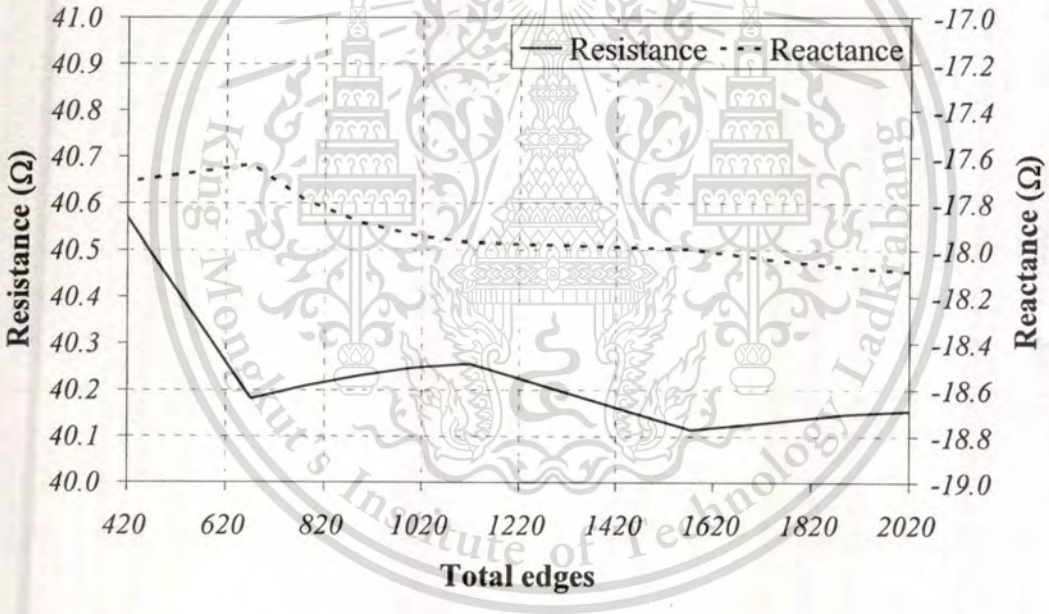

Fig. 3.7 Criterion of convergence.

To study the effect of each parameters (ring length, probe length and probe position), the MoM with RWG basis functions is used. Then, the antenna is modeled with a number of triangular patches feeding with a thin strip instead of a cylindrical one as shown in Fig. 3.4. Before computing the results, it is worthwhile to consider the number of triangular segments that used to model the antenna as shown in Fig. 3.7. The criterion of convergence consideration is that the deviation of input impedance of the antenna is less than 1%. Therefore, a number of

triangular segmentation of 1894 RWG basis functions with time consuming about 11 s (on the AMD Duron (tm) procuws, f=1.39 GHz, 624 MB of RAM) is used. Consequently, the antenna characteristics are investigated. The aim for using MoM with RWG basis functions (RWG-MoM) approach is to determine impedance characteristic. However, the radiation characteristics can be determined also to compare with the results from the dyadic Green's function approach. In addition, gain (including the total antenna efficiency which consists of both radiation and reflection efficiencies) of the antenna is also determined since it is used to compare with the measured gain in Chapter 5 (The directivity that yielded in Chapter 2 can not be used to compare with the measured gain.). Note that a thin strip width of excited probe should be 4 times of the radius of the equivalent cylindrical structure [39].

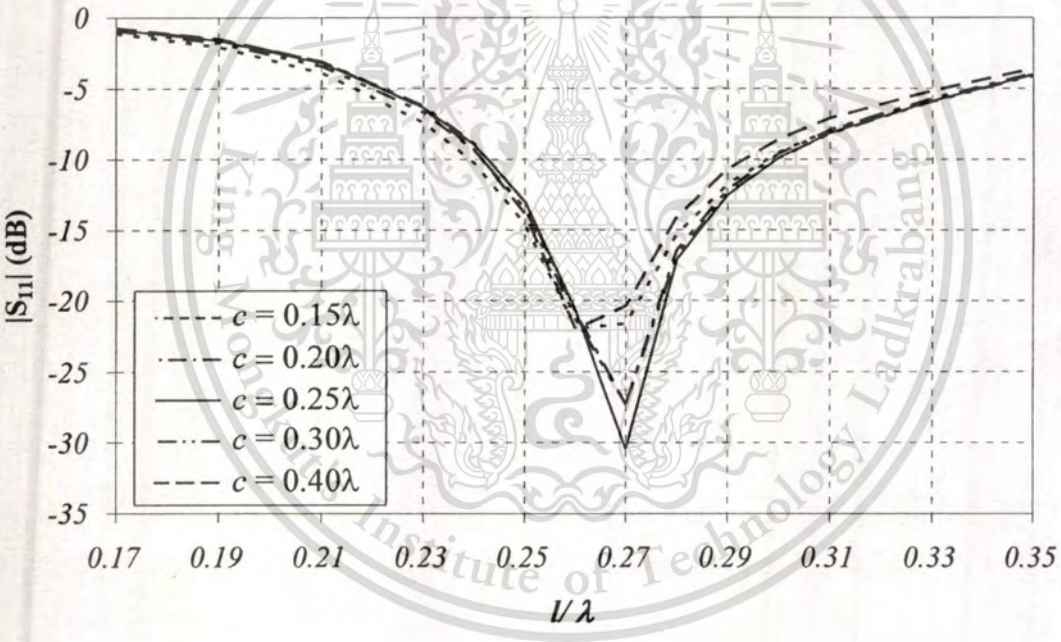

(a)

Fig. 3.8 $|S_{11}|$ and gain of the antenna versus probe length: (a) $|S_{11}|$ and (b) gain.

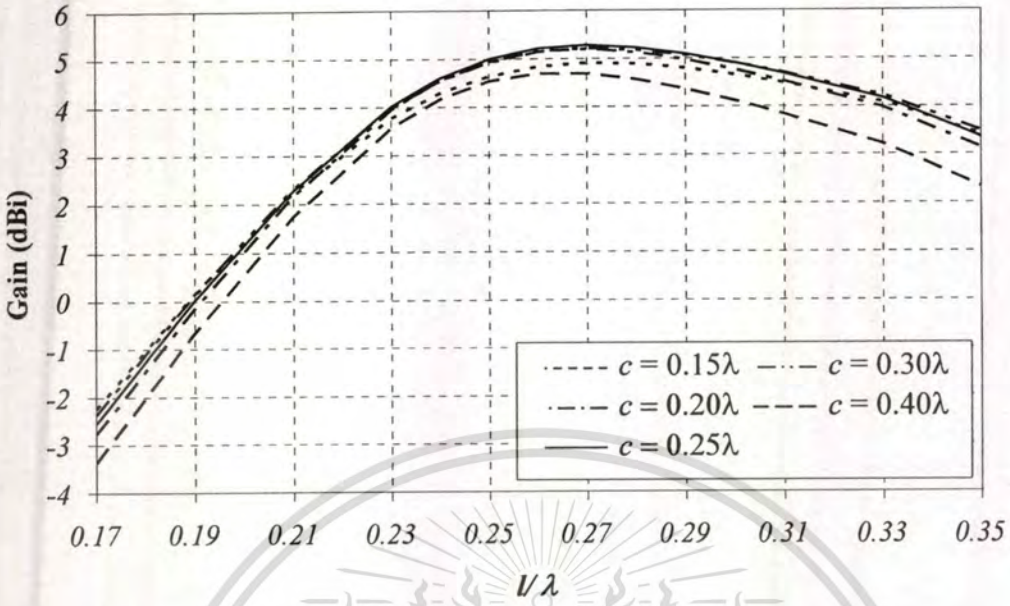

(b)

Fig. 3.8 $|S_{11}|$ and gain of the antenna versus probe length: (a) $|S_{11}|$ and (b) gain (cont.).

To consider the impedance matching between the antenna and coaxial transmission line with characteristic impedance of 50 Ω, the impedance is shown in terms of $|S_{11}|$ versus the probe length l for different c of 0.15λ, 0.20λ, 0.25λ, 0.30λ and 0.40λ respectively, as plotted in Fig. 3.8 (a). It is found that almost all cases provide good matched condition at probe length of 0.27λ with $|S_{11}|$ of -21.62 dB, -27.29 dB, -30.46 dB, -27.25 dB and -20.38 dB for c of 0.15λ, 0.20λ, 0.25λ, 0.30λ and 0.40λ, respectively ($c = 0.15\lambda$ and $c = 0.40\lambda$ provide the lowest $|S_{11}|$ of -21.96 dB and -22.00 dB at $l = 0.26\lambda$). Therefore, the probe length l of 0.27λ is chosen from now on. In addition, Fig. 3.8 (b) shows gains for various c versus probe length l. It is found that the increasing gains are yielded as the longer probe length l until $l = 0.27\lambda$ for c of 0.15λ, 0.20λ, 0.25λ and 0.30λ, and $l = 0.26\lambda$ for c of 0.40λ; then they are decreased. For $l < 0.19\lambda$, the negative gains are obtained due to the reflection coefficient is taken into account for the total gains, and this length is mismatch. Furthermore, the maximum gains are provided at $l = 0.27\lambda$ for c of 0.15λ, 0.20λ, 0.25λ and 0.30λ with gains of 4.92 dBi, 5.22 dBi, 5.28 dBi and 5.20 dBi, respectively, and at $l = 0.26\lambda$ for c of 0.40λ with gain of 4.70 dBi. Comparing the gain for different c, it is found that the ring length of 0.25λ provides the maximum gain and the best matching impedance.

In addition, frequency bands of $|S_{11}|$ and gains plotted as shown in Fig. 3.9. It is found that the resonant frequency is slightly shifted from the operating frequency to $0.99f_0$ with the impedance bandwidth 17% ($|S_{11}| < -10$ dB) for most ring lengths c as shown in Fig 3.7(a) except at c of 0.4λ; its resonance is $0.98f_0$ with impedance bandwidth 15%. It should be pointed that the resonant frequency of a probe-excited rectangular ring is affected by the probe excitation gathering a rectangular ring. Furthermore, at $\theta = 0^\circ, \phi = 90^\circ$ direction, gains of different c are plotted versus frequency as shown in Fig. 3.9 (b). Apparently, the increasing gains are obtained for the increasing frequency until the maximum point at the operating frequency f_0 for c of 0.20λ, 0.25λ and 0.30λ, and the frequency of $0.98f_0$ for c of 0.15λ and 0.40λ. Moreover, the ring length (c) of 0.25λ provides the maximum gain between 4.50 and 5.28 dBi along the frequency band from $0.90f_0 - 1.10f_0$ (the difference between maximum and minimum is less the 3 dB), while the ring length of 0.40λ provides the lowest gain between 3.41 and 4.76 dBi. At the operating frequency, the ring length c of 0.15λ, 0.20λ, 0.25λ, 0.30λ and 0.40λ provide gains of 4.92 dBi, 5.22 dBi, 5.28 dBi, 5.20 dBi and 4.76 dBi, respectively. As the results, the ring length c of 0.25λ is selected to provide the maximum gain.

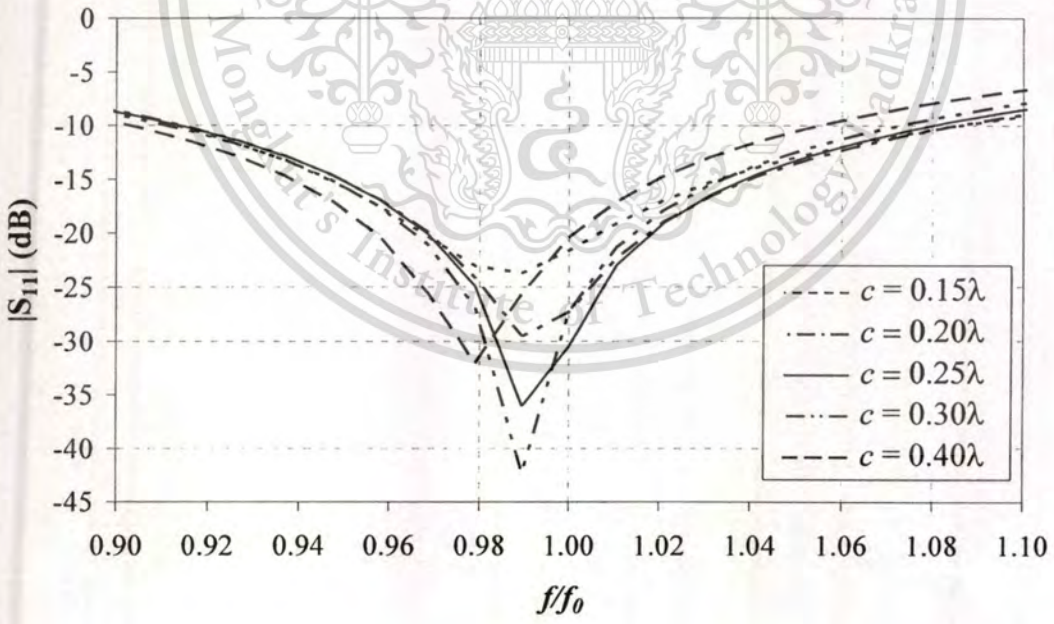

(a)

Fig. 3.9 Frequency bands of: (a) $|S_{11}|$ (b) gain.

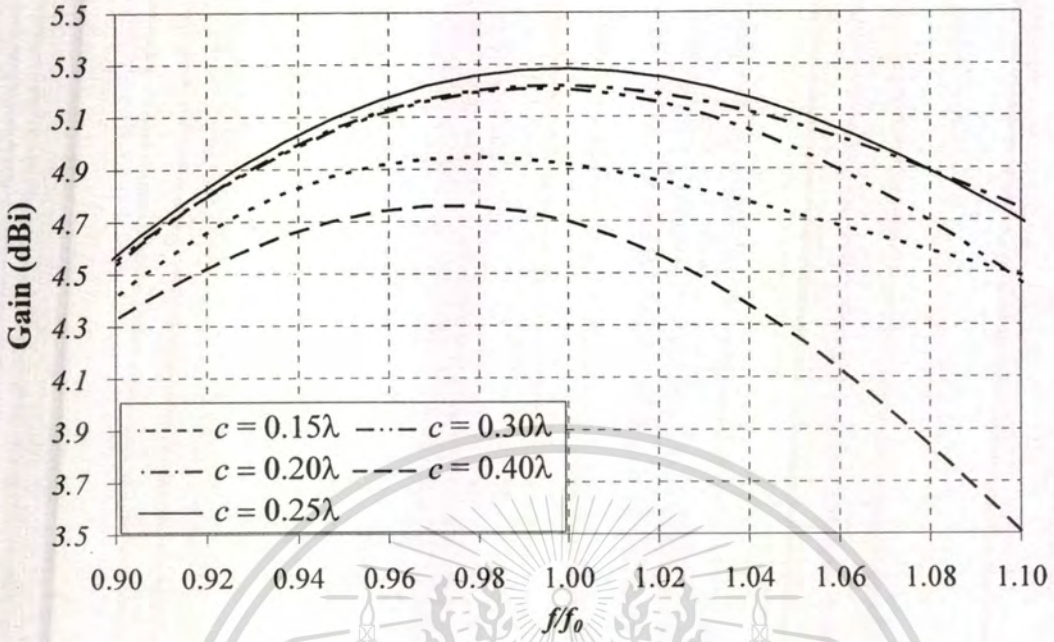

(b)

Fig. 3.9 Frequency bands of: (a) $|S_{11}|$ (b) gain (cont.).

In addition to the probe length, the effect of probe position to $|S_{11}|$ and gain of the presented antenna is also considered and plotted as shown in Fig. 3.10. It is found that $|S_{11}|$ and gain have the opposite curve; i.e., $|S_{11}|$ is increased as further distance of s from the center ($x = s$, $y = -b/2$, $z = 0$) while gain is decreased. The matching condition can be obtained when $s < 0.11\lambda$; at the center ($s = 0$, $y = -b/2$, $z = 0$), the best matched condition with $|S_{11}|$ of -30.46 dB is provided. Gain is decreased because of the mismatched condition. However, gain is slightly decreased for $s > 0.11\lambda$ since the impedance in this range is matched. It is implies that reflection efficiency due to the matching between the antenna and transmission line has more effect to gain which is more than radiation efficiency for various probe positions. On the other hand, the probe position plays a role to the impedance rather than the radiation characteristics.

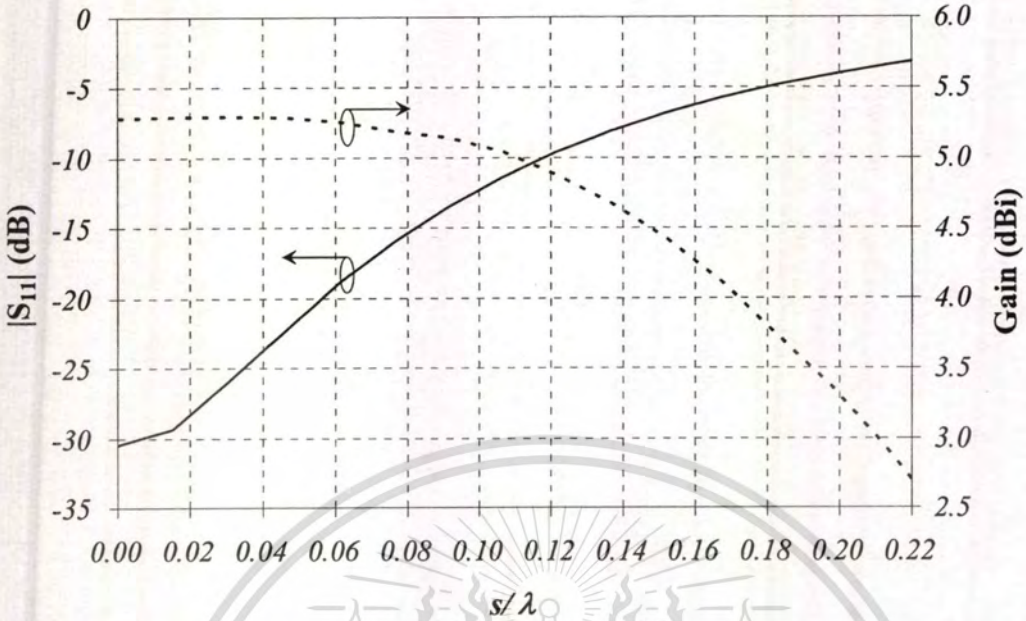

Fig. 3.10 $|S_{11}|$ and gain for various *s*.

Furthermore, the current distributions on the antenna structure are investigated as shown in Fig. 3.11. Apparently, the maximum current occurs at the feed point, and it is dense along a linear probe. Accordingly, the radiation fields are mainly produced from the linear probe and its radiation pattern is confined by the rectangular ring providing bidirectional beam in forward and backward directions. It should be pointed that the linear probe has been strongly affected to the impedance of the antenna.

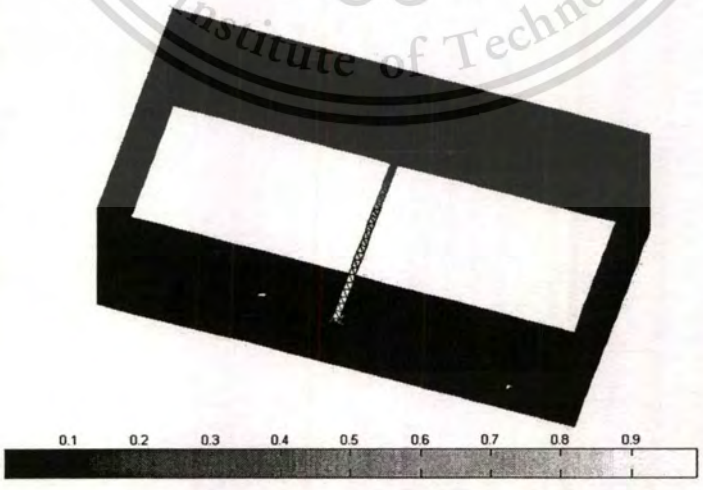

Fig. 3.11 Current distributions on the antenna.

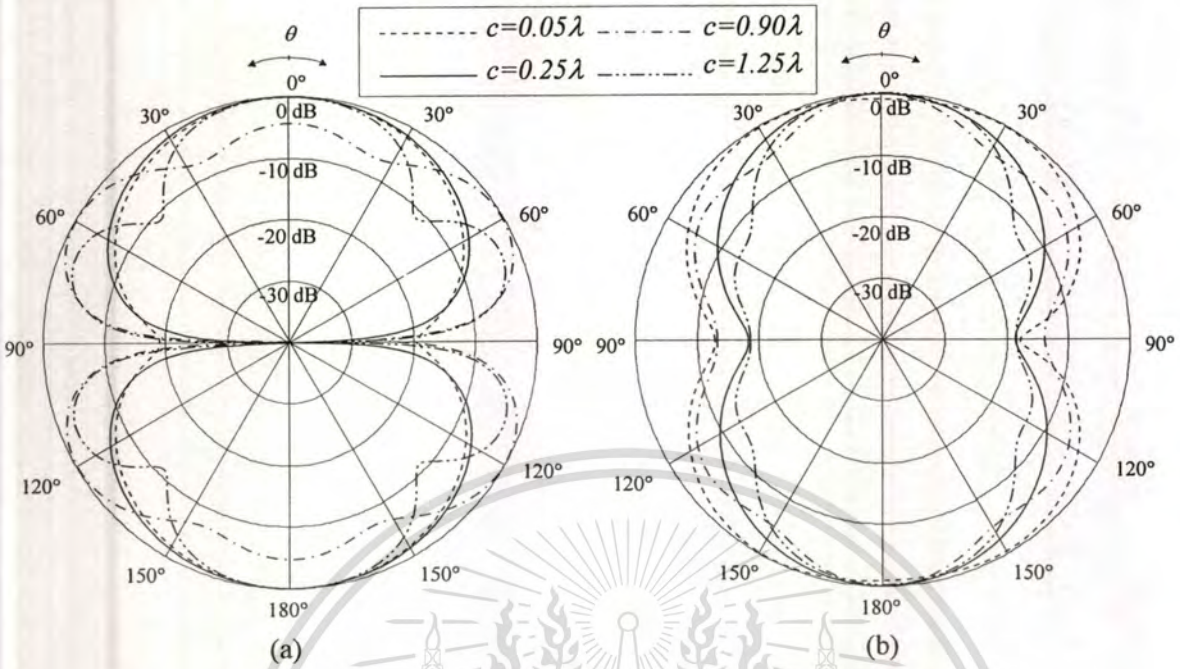

Fig. 3.12 Radiation pattern: (a) *yz*-plane and (b) *xz*-plane.

In addition, the radiation characteristics of the proposed antenna can also be determined to compare with those results obtained from the dyadic Green's function approach in Chapter 2. Fig. 3.12 shows the radiation patterns of a probe-excited rectangular ring antenna for various ring lengths of c. It is found that a bidirectional pattern can be produced due to the confinement of linear probe by rectangular ring. In addition, the separation between the two apertures or the ring length (c) has been strongly influenced to the radiation pattern. In the *yz*-plane, the beamwidth is widened and then split by increasing c. After that, a bidirectional pattern with side lobes is achieved again at $c = 1.25\lambda$. By varying c, the beamwidth of the shorter c in the *xz*-plane is widened because the aperture separation affects the radiation patterns. In addition, in the *yz*- and *xz*-planes patterns have null at $\theta = 90^{\circ}$ due to the ring edge effecting. Comparing results between the dyadic Green's function approach and the MoM with RWG basis function, it is found the same trend of radiation pattern can be obtained. However, using the MoM with RWG basis function, the beamwidths of the antenna are narrower and its null is deeper rather than another one.

3.4 Summary

This chapter presents the impedance, gain and radiation pattern of a probe-excited rectangular ring antenna by using MoM with the RWG basis functions, which is suitable for modeling metallic surface problem. The dimensions of rectangular ring are same as the rectangular waveguide operated at the dominant mode (TE_{10}) as stated in Chapter 2. Using MoM with the RWG basis functions, the antenna is modeled by dividing the antenna surfaces into a number of triangular patches of 1896 segments. Then, the input impedance in terms of $|S_{11}|$ and gain of the present antenna are investigated for various probe lengths and probe positions with different ring length. It is found that the ring length of 0.25λ with the probe length of 0.27λ located at the center ($x = s = 0, y = -b/2, z = 0$) provides the maximum gain of 5.28 dBi and the best impedance matching. By using the delta gab voltage excitation, it is found that the current distributes dense along the linear probe, and then the electric fields radiate. Therefore, a probe excitation has been strongly influenced to the input impedance of the present antenna. Furthermore, the radiation pattern of the antenna is also determined to compare with those obtained from the dyadic Green's function approach. It is obvious that, using the MoM with RWG basis function, the bidirectional pattern with the narrower beamwidths and deeper null rather than that one from the dyadic Green's function approach is obtained. However, both methods provide a same trend of radiation pattern. The validity of this approach is verified by referring to the measurement in Chapter 5.

CHAPTER 4
BAND-WIDTH ENHANCEMENT USING STEPPED-MONOPOLE EXCITATION

4.1 Introduction

Since the Federal Communications Commissions (FCC) announced the decision to allow the unlicensed use of the bandwidth of 3.1-10.6 GHz [28], ultra-wideband (UWB) antennas are gaining prominence and becoming very attractive in modern wireless and mobile communication systems. Many researches and developments on UWB antennas have been continuously conducted [40]-[49]. Among the UWB antenna designs in the recent literature, monopole antennas [50]-[52] are widely employed because of their simple structure and low cost. Many techniques have been reported to extend the antenna bandwidth of the conventional narrow-band antenna for example using the additional substrate [53], introducing several types of sleeves [54]-[55], adding parasitic elements [56] and adopting proximity-coupled configuration with multilayer structure [57]. Most of these antennas yield omnidirectional radiation patterns.

As mention earlier that base station antennas in a microcellular system for the urban areas are located lower than the surrounded buildings along the streets and sometime they are located in the underground areas; the communicable cell is formed along the street. For these environments, the omnidirectional pattern is degraded when it places closed or attached to the wall or metal. If a bidirectional antenna is applied, the deterioration on the omnidirectional antenna performance can be avoided. In addition, the bidirectional antenna is suitable for the street cell because its radiation pattern can be formed along the street. Therefore, the developments on UWB antennas possessing bidirectional pattern are desirable. As mentioned earlier in the previous chapter, we can obtain a bidirectional pattern from a simple-structure and cost-effectiveness of a probe-excited rectangular ring antenna [58], [59]. However, the bandwidth of a probe-excited rectangular ring antenna is relatively narrow. Therefore, the impedance bandwidth should be improved. This chapter presents an approach for extending the band-width of a bidirectional rectangular ring antenna. Therefore, a bidirectional UWB antenna using rectangular ring fed by stepped

monopole instead of probe-excited (linear monopole) is introduced to enhance the impedance bandwidth of the proposed antenna. The antenna structure and parameter study are also presented in detail.

This chapter is organized as follows. Section 4.2 shows the antenna structure. The antenna designs are presented in Section 4.3. Finally, summary is provided in Section 4.4.

4.2 Antenna Structure

The configuration of the antenna consists of the stepped monopole excitation and the rectangular ring as shown in Fig. 4.1 (a). The stepped monopole in Fig. 4.1 (b) is connected to the center conductor of the coaxial transmission line at the feeding point. The coaxial transmission line with air dielectric has a characteristic impedance of 50 Ohms. From Fig. 4.1(b), the parameters of the stepped monopole comprises the top width (w_1), the middle width (w_2), the bottom width (w_3), the middle height (h_1), the bottom height (h_2) and the total height (h). The thickness of the stepped monopole is represented by d. This stepped monopole is surrounded by the rectangular ring with the ring width of a, the ring height of b and the ring length of c. In addition, the gap between the ground plane (the bottom of the rectangular ring) and the bottom of the stepped monopole is defined by δ.

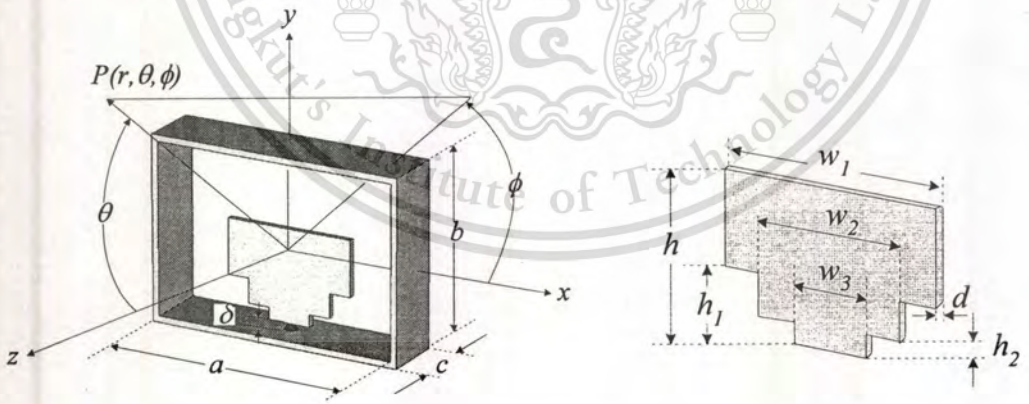

(a) (b)

Fig. 4.1 Antenna structure: (a) perspective view and (b) stepped-monopole excitation.

4.3 Antenna Design

In this section, the parametric studies of the proposed antenna are performed to investigate their effects to impedance and radiation characteristics. In addition,

antenna fabrication and measurement are also carried out. To study the antenna parameters, the CST Microwave Simulation is used to simulate the present antenna excluding a coaxial connector in the antenna model (to analyze only the effects from the antenna parameters). Because it is very convenient for varying many parameters with less time consume compared to RWG-MoM in Chapter 3 in which the convergent criterion of RWG-MoM should be taken very good care for the accuracy when changing the antenna structure.

4.3.1. Antenna Evolution

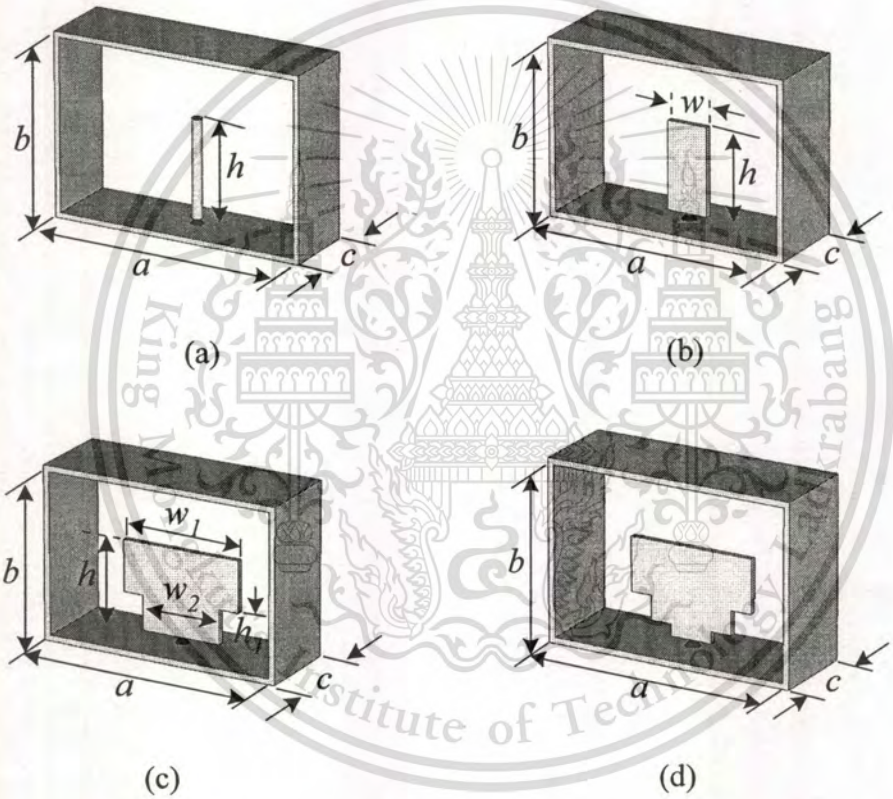

Fig. 4.2 Rectangular ring antennas: (a) linear-monopole excitation, (b) rectangular-monopole excitation, (c) T-monopole excitation and (d) stepped-monopole excitation.

As shown in previous chapters, it is evident that the bidirectional antenna was accomplished by using the linear-monopole excitation (probe-excited) rectangular ring. Nevertheless, the bandwidth of the proposed antenna is relatively narrow. In order to enhance the bandwidth, the feeding structure must be modified. (Note that, for the different feeders, the dimensions of the rectangular ring and the height of the monopole (feeder) are same.) Fig. 4.2 shows the antenna revolution to enhance the

bandwidth. Fig. 4.2 (a) shows the conventional rectangular ring antenna fed by a linear-monopole excitation. In order to accomplish the bidirectional pattern along the UWB frequency range from 3.1 to 10.6 GHz, the impedance band width is enhanced using rectangular-monopole, T-monopole, and stepped-monopole excitations as shown trough Figs. 4.2 (b)-4.2 (d), respectively.

Fig. 4.3 shows $|S_{11}|$ versus frequency for various feeding monopoles. Apparently, the $|S_{11}|$ around the resonant frequency can be improved using the rectangular monopole with spreading the width w rather than the linear monopole. Nevertheless, the use of rectangular-monopole excitation cannot achieve the ultra-wideband operation. Then, the use of T-monopole excitation as shown in Fig. 4.2 (c) is introduced. The bandwidth at lower frequency can be enhanced. However, the ultra-wideband operation is achieved by using stepped monopole as shown in Fig. 4.2 (d). The design parameters will be shown and tabulated in the next subsection.

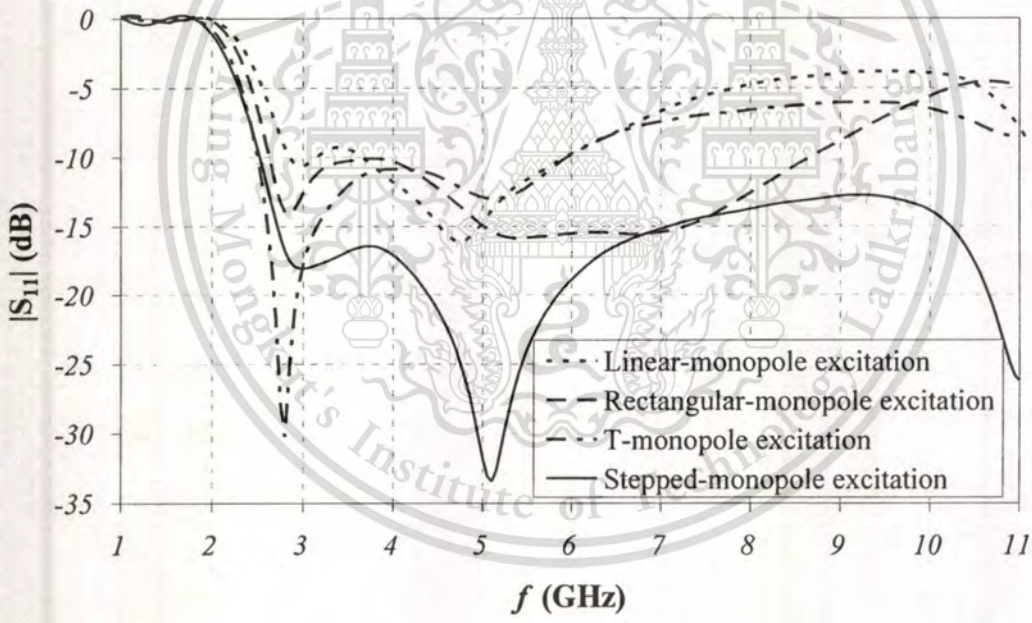

Fig. 4.3 $|S_{11}|$ versus frequency for various feeding monopoles.

Fig. 4.4 through Fig. 4.6 show the radiation patterns of the rectangular ring antenna fed by linear-monopole, rectangular-monopole, T-monopole and stepped-monopole excitations at 3.1 GHz, 6.5 GHz and 10.6 GHz, respectively. It is obvious that the radiation patterns in *yz*-plane are fairly identical for different excited monopoles. At the high frequency, the beam-peak direction trends to alter from the direction of $\theta = 0$ and 180 degrees, it is due to the asymmetry of the antenna structure

between the bottom and the top of the ring in this plane; since, the feeder is located at the bottom of rectangular ring. The beam-peak directions of the antenna fed by linear-monopole, rectangular-monopole, T-monopole and stepped-monopole excitations, respectively, in *yz*-plane are as follows: At the frequency of 3.1 GHz, they direct to 3, 3, 3 and 4 degrees, respectively. For the frequency of 6.5 GHz, they direct to 24, 25, 30 and 30 degrees, respectively. At the frequency of 10.6 GHz, they direct to 16, 23, 39 and 39 degrees, respectively. In addition, the field distributions at the aperture trend to bend away from the center of the aperture to both sides of the edge of the ring (as seen in Fig. 4.21). Moreover, the same trend of symmetry bidirectional pattern is achieved from the rectangular ring fed by the different monopole-excitations in *xz*-plane. The beam-peak direction of $\theta = 0$ degree is provided at the selected frequency except for the T- monopole and stepped-monopole excitations at f of 6.5 GHz; they direct to the same direction at θ of 27 degree. From these results, it is observed that the impedance and the radiation pattern are strongly affected by the feeder and rectangular ring, respectively. Since, the impedances in terms of $|S_{11}|$ of the same dimensions of rectangular ring antenna fed by the different monopoles are significantly different, while the radiation patterns are fairly stable. In the next subsection, parametric study of an UWB antenna using rectangular ring fed by a stepped-monopole is shown in detail.

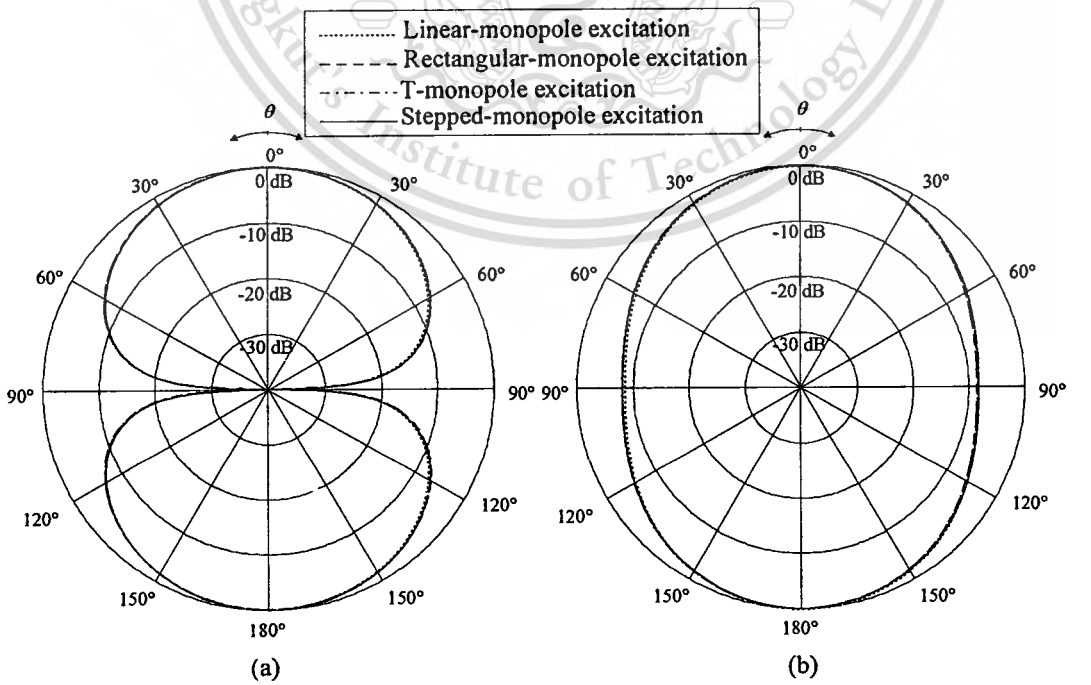

Fig. 4.4 Radiation pattern at 3.1 GHz: (a) *yz*-plane, (b) *xz* –plane.

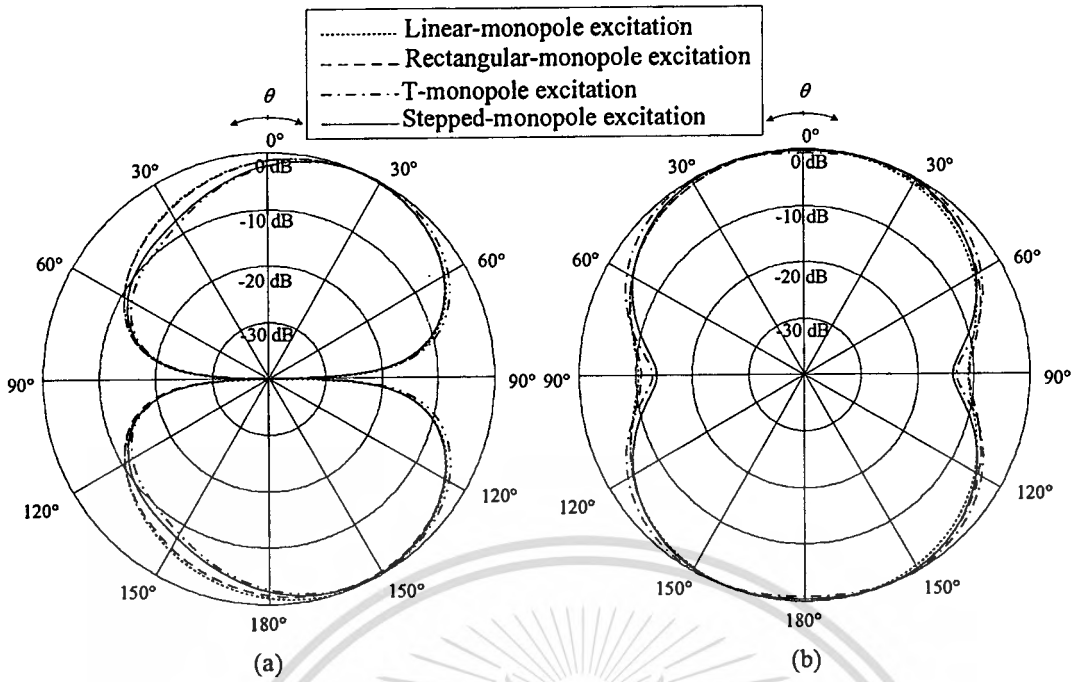

Fig. 4.5 Radiation pattern at 6.5 GHz: (a) *yz*-plane, (b) *xz* –plane.

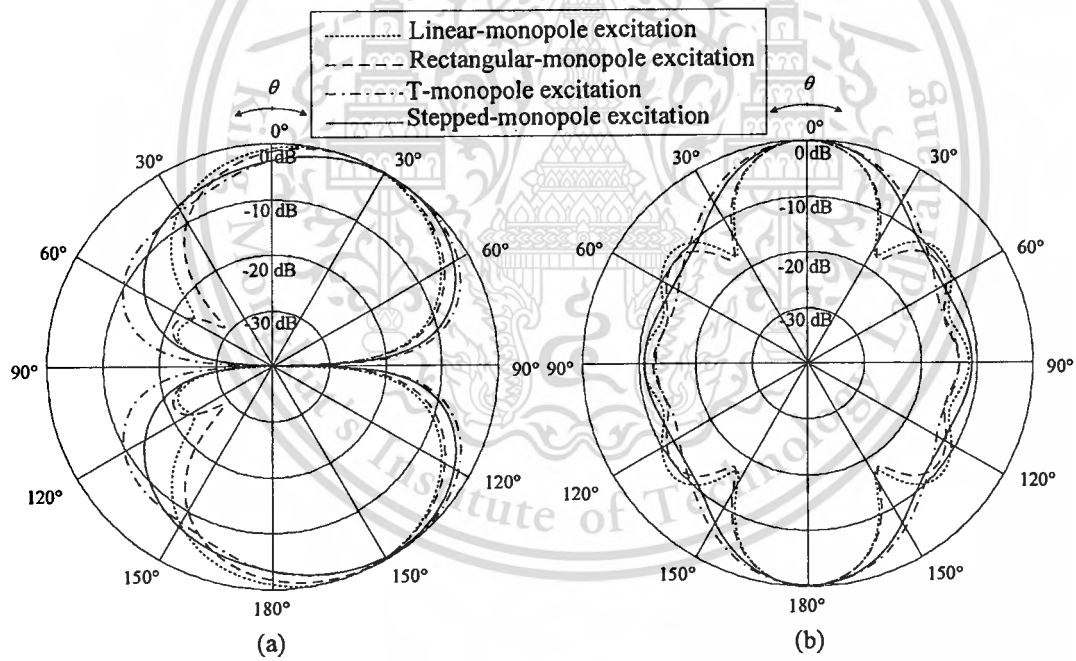

Fig. 4.6 Radiation pattern at 10.6 GHz: (a) *yz*-plane, (b) *xz* –plane.

4.3.2 Parametric Study

In order to accomplish the bidirectional pattern along the UWB frequency range from 3.1 to 10.6 GHz, the antenna design is separated into two parts for rectangular ring and stepped monopole, respectively. It is found that the bidirectional pattern and resonant frequency are significantly affected by the rectangular ring, whereas the

stepped monopole influences to the bandwidth enhancement. Starting with the rectangular ring, its initial width (a) is designed with TE_{10} mode to operate at the lower edge frequency of UWB range. Therefore, the initial ring width (a) is 48 mm. The quarter wavelength of the linear monopole at 3.1 GHz (h = 24 mm) is also initialized for the impedance matching. Fig. 4.7 shows the bandwidth of the nearest resonant frequency of 3.1 GHz of the rectangular ring fed by the quarter-wave monopole for various ring parameters. From this figure, the height (b) and the length (c) of rectangular rings are determined from the widest bandwidth. For compact size, the ring length (c) of 15 mm and b/a of 0.7 are selected.

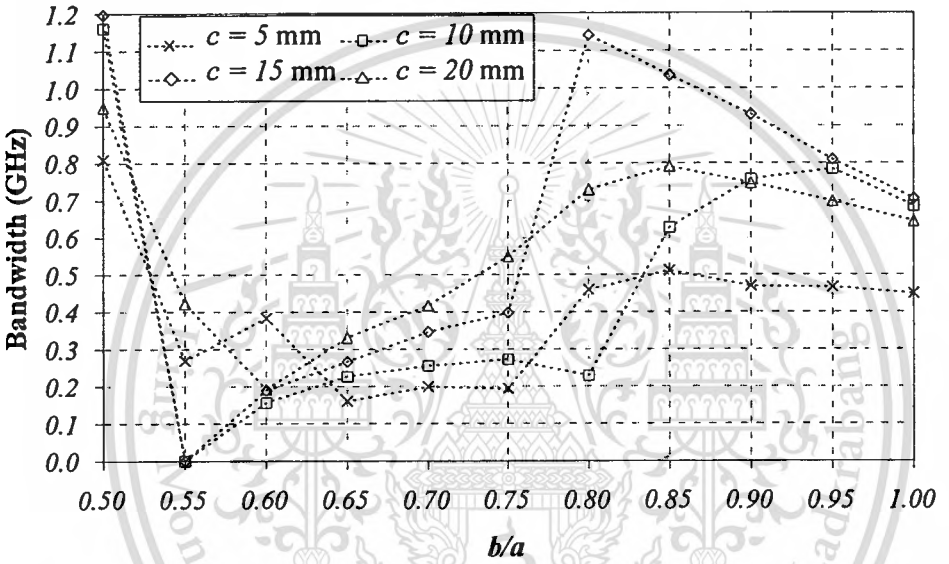

Fig. 4.7 Bandwidth of the lowest resonant frequency as the function of b/a (a = 48 mm, h = 24 mm).

Table 4.1 Suitable parameters that obtain the lower and upper resonant frequencies nearly 3.1 GHz and 10.6 GHz.

h/b	0.42	0.46	0.52	0.60
b/a	1.00	0.90	0.80	0.70

After the initial parameters of a, b and c are chosen, the length of the linear monopole (h) is varied in terms of h/b for different b/a to determine the suitable condition of resonant frequencies for UWB. The lower and the upper resonant frequencies as function of h/b are shown in Fig. 4.8 and Fig. 4.9, respectively. Obviously, the suitable parameters that provide the lower and the upper resonant

frequencies nearly 3.1 GHz and 10.6 GHz are tabulated in Table 4.1. For the compact antenna size, *b/a* of 0.7 and *h/b* of 0.6 are appropriately chosen.

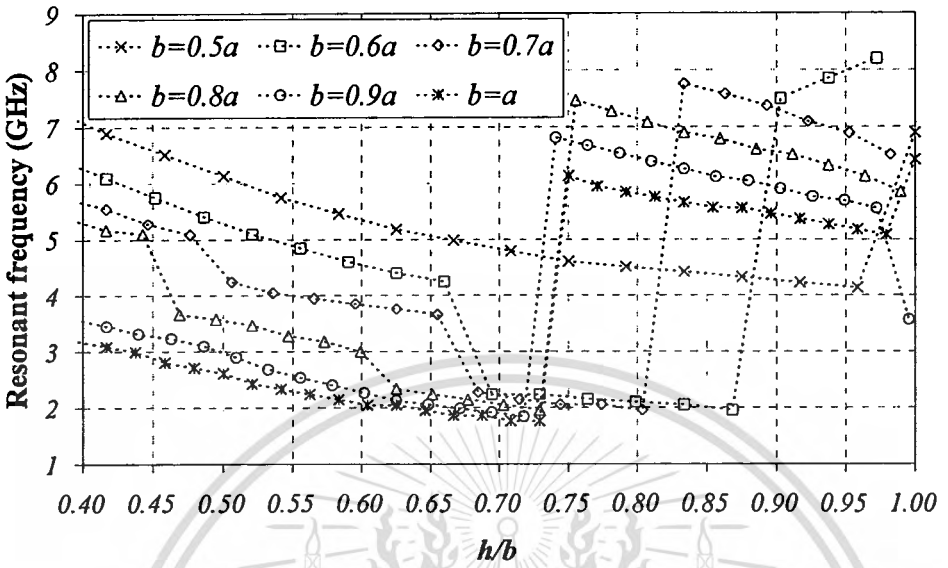

Fig. 4.8 The lower resonant frequency for various *h/b* ($a = 48$ mm, $c = 15$ mm).

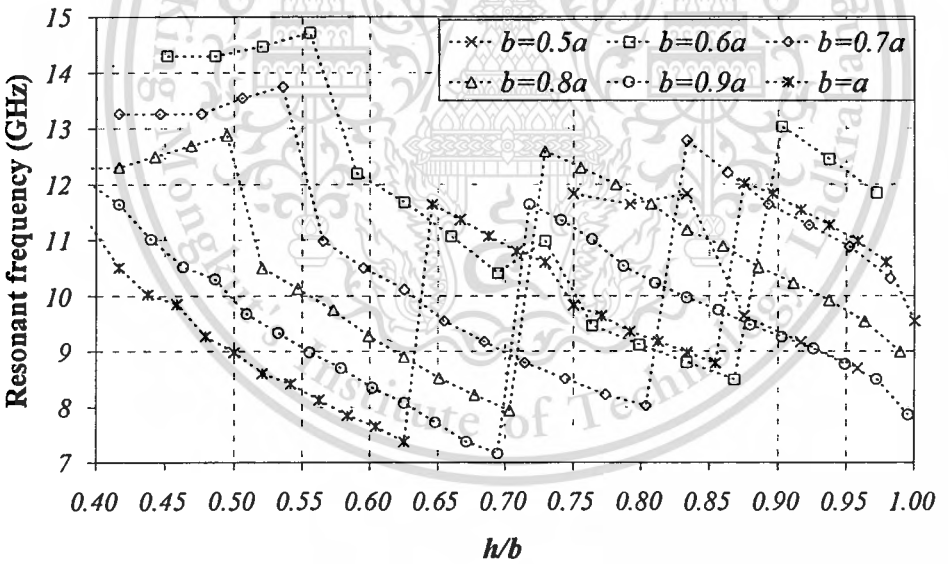

Fig. 4.9 The upper resonant frequency for various *h/b* ($a = 48$ mm, $c = 15$ mm).

Moreover, the ring width (*a*) can be varied to adjust the lower and the upper resonant frequencies as shown in Fig. 4.10. To achieve the lower and the upper resonant frequencies very close to 3.1 GHz and 10.6 GHz respectively, the ring width (*a*) of 40 mm is chosen. Therefore, the suitable parameters of rectangular ring fed by linear monopole that obtains the resonant frequencies proximity to 3.1 GHz and 10.6

GHz are as follows: $a = 40$ mm, $b = 0.7a = 28$ mm, $c = 15$ mm and $h = 0.6b = 16$ mm. These parameters will be used throughout this chapter.

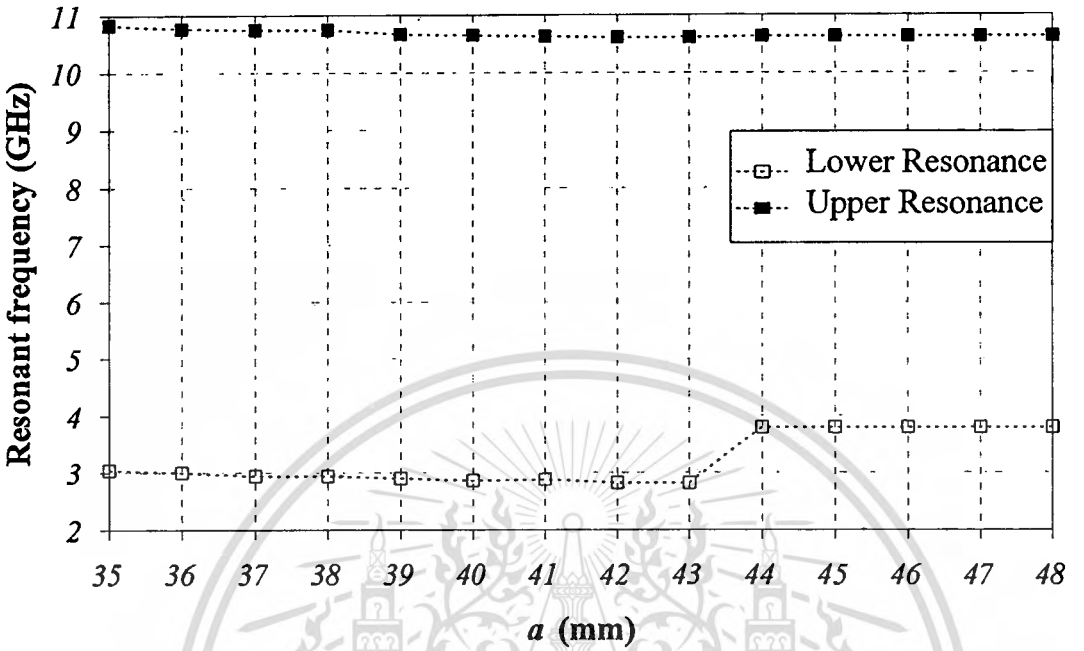

Fig. 4.10 Resonant frequency for various a ($b = 33.6$ mm, $h = 0.6b = 20$ mm).

It is noted from Fig. 4.10 that other ring widths (a) rather than 40 mm can be also selected as required. In this chapter, the ring width (a) of 40 mm is chosen due to available and compact sizes in the fabrication. The smaller ring width yields more compact antenna size at the expense of slightly gain degradation. By following the guidelines of antenna design as mentioned above, other parameters such as b, c, h and w_1 can be determined. After that, h_1, w_2 and w_3 are subsequently obtained. The parameter h_2 can be used to improve the $|S_{11}|$.

To achieve the UWB characteristics, the $|S_{11}|$ along the lower and upper resonant frequencies must be less than -10 dB. Thus, the stepped monopole is introduced to excite the rectangular ring instead of linear monopole. To design the stepped monopole, the dimension should be related with multiple $\lambda_U / 4$ sections ($n\lambda_U / 4$) [27], where λ_U is the free space wavelength of the upper edge frequency of UWB (10.6 GHz) and n is positive integer number. This is due to the fact that the current distribution will be dense at the stepped monopole excitation rather than the rectangular ring at the high frequency. Fig. 4.11 shows $|S_{11}|$ versus frequency for

various h_1. For impedance matching, the choice of h_1 is approximately to $n\lambda_U / 4$, and it is geometrically restricted to be shorter than h. For h = 16 mm in this case, n can be either 1 or 2 that corresponding to h_1 of 7 mm and 14 mm, respectively. However, h_1 of 14 mm is very close to h (h = 16 mm), and it is difficult to adjust the parameters for further bandwidth improvement as seen in Fig. 4.11. Therefore, h_1 of 7 mm is selected because of the flexible design; h_1 of 6 mm and 10 mm can be used also but h_1 of 7 mm provides the better $|S_{11}|$ at the higher frequency.

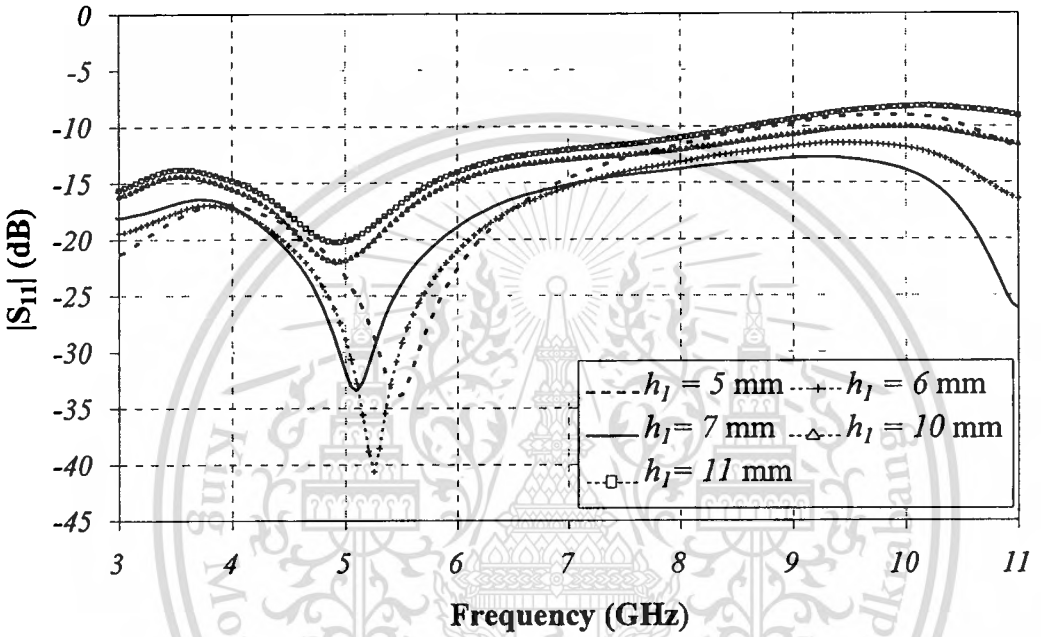

Fig. 4.11 $|S_{11}|$ for various h_1.

To further improve the $|S_{11}|$, additional step is introduced in term of h_2. From Fig. 4.12, h_2 is varied to observe its influence to $|S_{11}|$ versus frequency. It is apparent that h_2 of 3 mm and 5 mm can be selected because the $|S_{11}| < -10$ dB along the UWB range. Comparing between h_2 of 3 mm and 5 mm, it is preferable to choose h_2 of 3 mm because the $|S_{11}|$ at 3.1 GHz and 10.6 GHz is lower.

Furthermore, the widths of stepped monopole are designed in terms of $n\lambda_U / 4$ with the condition that $w_1 > w_2 > w_3$. Fig. 4.13 shows $|S_{11}|$ for various w_1 of 14 mm, 16 mm, 21 mm, 28 mm and 30 mm. It is found that w_1 of 21 and 28 mm provide $|S_{11}| < -10$ dB covered the frequency range from 3.1-10.6 GHz. However, w_1 of 21 mm yields $|S_{11}|$ better than w_1 of 28 mm; thus, w_1 of 21 mm is selected. Moreover, the influence of w_2 and w_3 are also investigated as shown in Figs. 4.14-4.15. From the plot of $|S_{11}|$ for w_2 of 7 mm, 11 mm, 14 mm, 15 mm and 21 mm as shown in Fig. 4.14,

it is found that $|S_{11}| < -10$ dB is obtained for w_2 of 11 mm, 14 mm and 15 mm; w_2 of 14 mm is chosen related with $n\lambda_U / 4$ where $n = 2$. In addition, w_3 of 3 mm, 5 mm, 7 mm, 9 mm and 14 mm is plotted in Fig. 4.15. Obviously, w_3 of 5 mm, 7 mm and 9 mm provide $|S_{11}| < -10$ dB. In this work, w_3 of 7 mm is selected because the better matching condition compared to those three values is obtained.

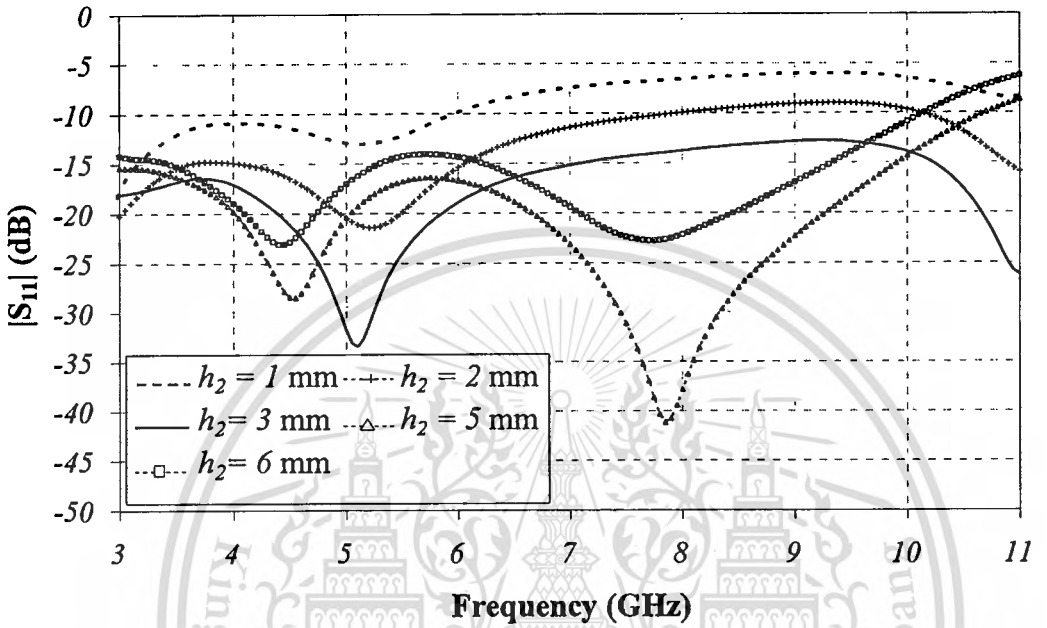

Fig. 4.12 $|S_{11}|$ for various h_2.

It should be pointed out from Figs. 4.11 through 4.15 that w_1 is limited by the ring width (a) and its ranges must from $0.5a$ to $0.7a$. From the design criteria, w_1 of 21 mm, w_2 of 14 mm and w_3 of 7 mm are chosen according to n of 3, 2 and 1, respectively. The influence of these parameters to the $|S_{11}|$ along the frequency is described. It should be noted that if one parameter is varied, the remaining parameters are fixed. Apparently, the stepped monopole can improve the $|S_{11}|$ along the bandwidth of 3.1-10.6 GHz. The designed parameters are ultimately tabulated in Table 4.2.

Table 4.2 Designed parameters.

Parameters	a	b	c	h	h_1	h_2	w_1	w_2	w_3	d	δ
Physical size (mm)	40	28	15	16	7	3	21	14	7	1	1

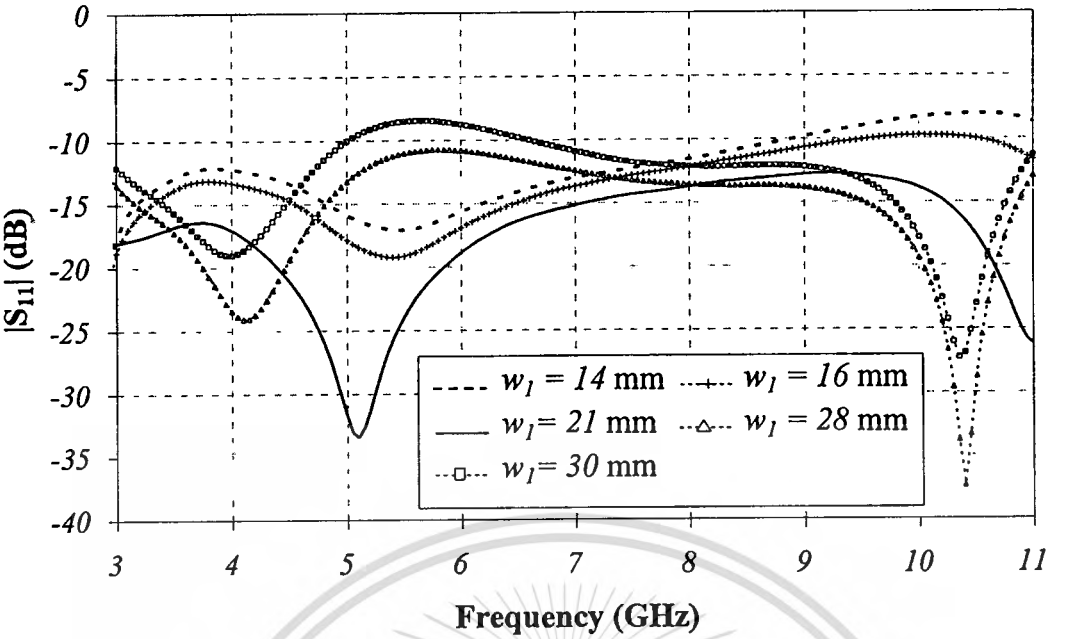

Fig. 4.13 $|S_{11}|$ for various w_1.

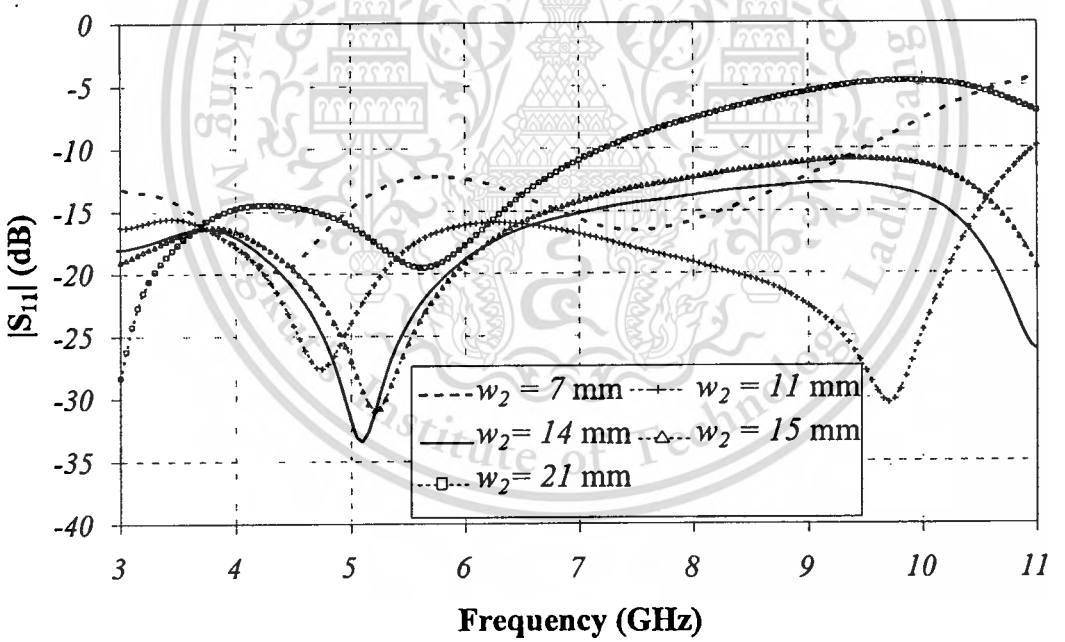

Fig. 4.14 $|S_{11}|$ for various w_2.

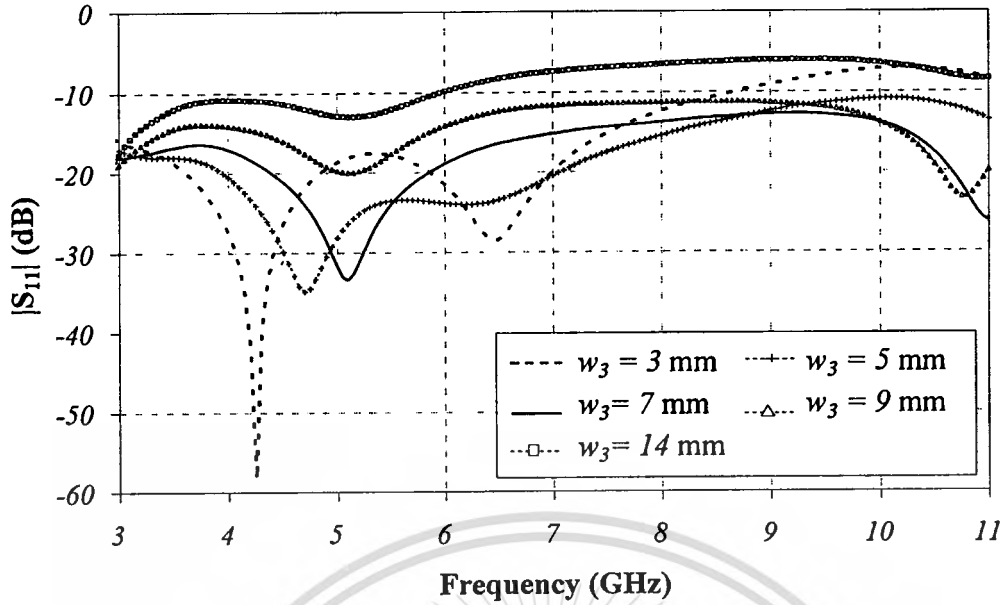

Fig. 4.15 $|S_{11}|$ for various w_3.

In addition, considering the effect of the ring length c, $|S_{11}|$, beam-peak direction, gain, and polarization are investigated. Fig. 4.16 shows the $|S_{11}|$ for various c of 10 mm, 15 mm, 20 mm and 25 mm. It is found that they provide $|S_{11}|$ < -10 dB along the frequency range of 3.1-10.6 GHz with $|S_{11}|$ between -25.76 to -12.67 dB, -33.45 to -12.75 dB, -23.55 to -13.46 dB, and -18.97 to -11.02 dB for c of 10 mm, 15 mm, 20 mm and 25 mm, respectively. The ring length c of 15 mm provides the better $|S_{11}|$ along the UWB frequency range.

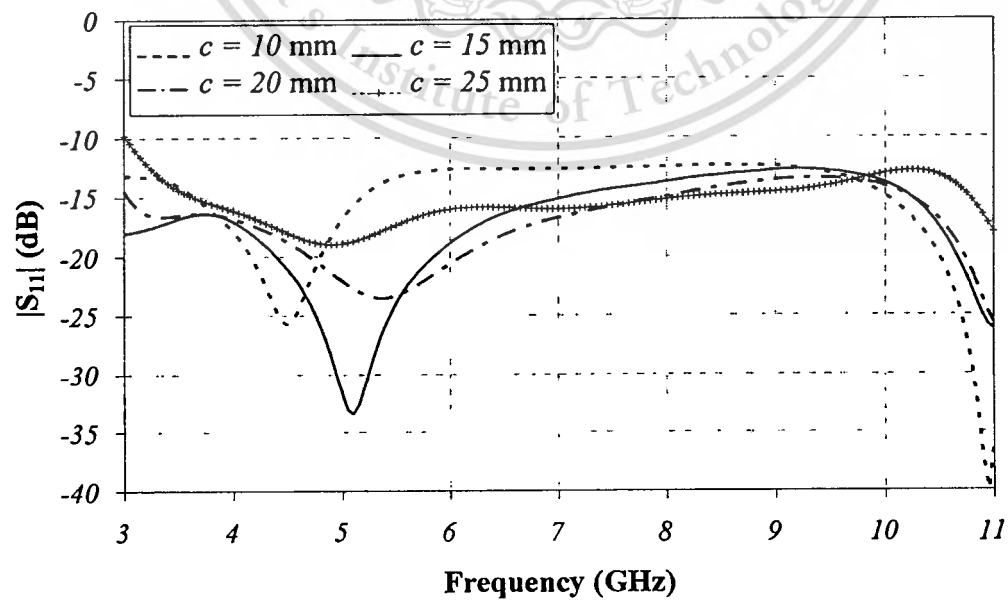

Fig. 4.16 $|S_{11}|$ versus frequency for various ring lengths.

Figures 4.17 (a) and 4.17 (b) show the beam-peak directions for various *c* in *yz*- and *xz*-planes, respectively. It is found that the increasing deviated angle is obtained as increasing *c* in both *yz*- and *xz*-planes at the higher frequency as shown in Fig. 4.17. In *xz*-plane, the beam-peak directions alter from *z*-axis at the frequency about 4.5-7 GHz for *c* of 10 mm, 5-7.5 GHz for *c* of 15 mm and 20 mm, and 5-7 GHz and alter again at 10-11 GHz for *c* of 25 mm. On the other hand, the smaller altered angles from *z*-axis are obtained as the smaller *c*.

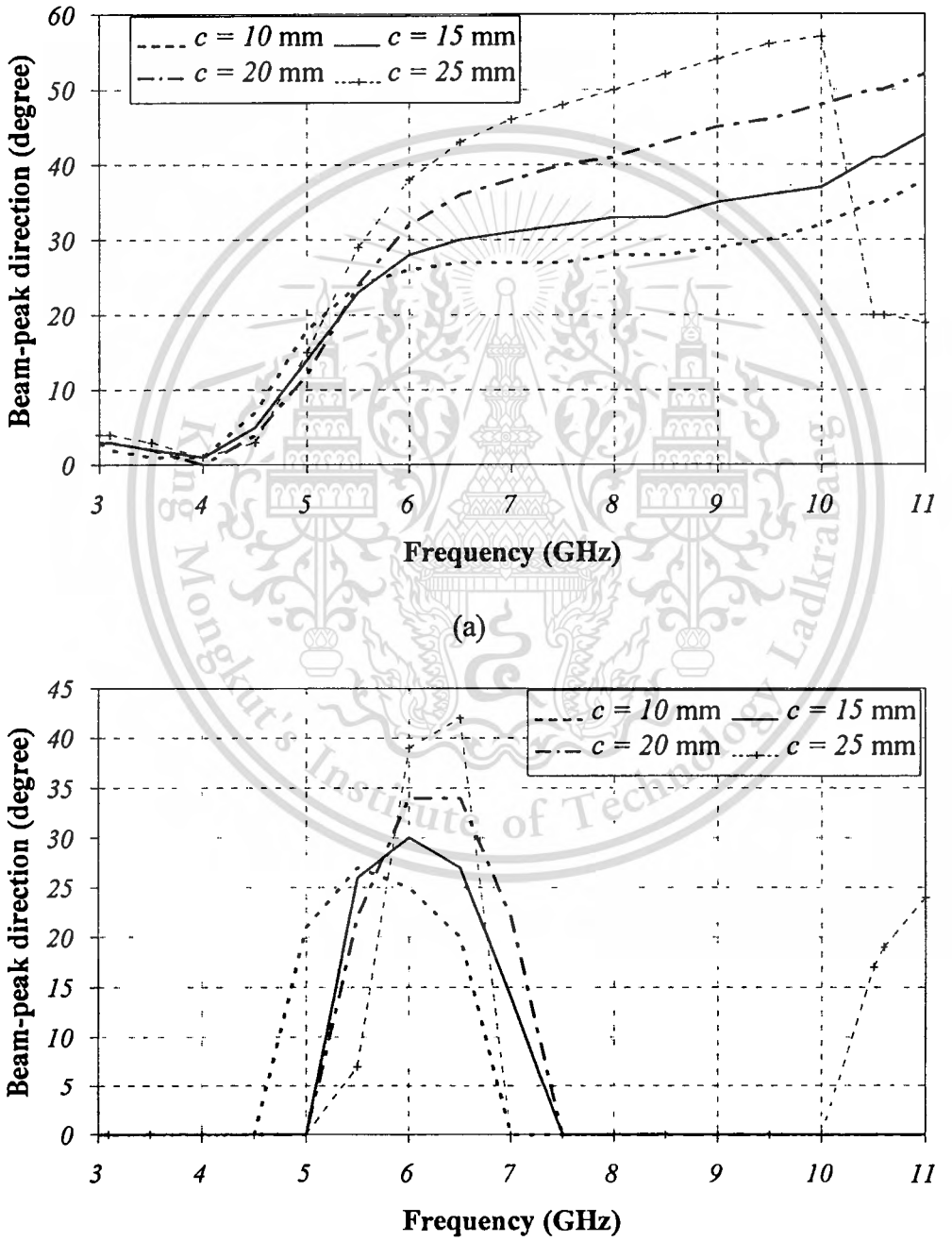

Fig. 4.17 Beam-peak directions: (a) *yz*-plane, (b) *xz*-plane GHz.

In addition, gains for c of 10 mm, 15 mm, 20 mm and 25 mm are shown in Fig. 4.18. Apparently, gains between 2.58-5.52 dBi, 2.33-5.21 dBi, 1.82-4.65 dBi, and 1.17-4.45 dBi, respectively, for c of 10 mm, 15 mm, 20 mm and 25 mm. The maximum gains are provide at 9.5 GHz for c of 10 mm and 15 mm, at 4 GHz for c of 20 mm, and at 4.5 GHz for c of 25 mm. The maximum gain is yielded from c of 10 mm, while the c of 25 mm provides the lowest gain. For polarization of the antenna, the cross polarization discrimination (XPD) for various c is plotted showing the polarization purity of the antenna as shown in Fig. 4.19. It is found that nearly purely linearly polarized with XPD of better than 145 dB at $\theta = 0°, \phi = 90°$ for all cases is provided.

In this work, c of 15 mm is selected due to its $|S_{11}|$ is better than c of 10 mm even it proves fairly lower gain comparing to c of 10 mm.

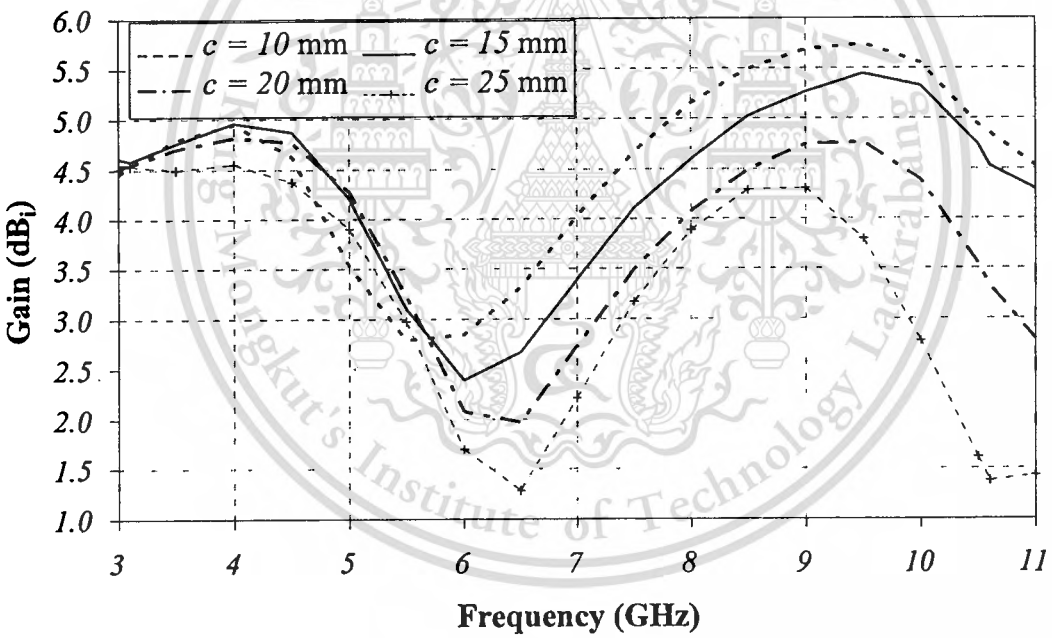

Fig. 4.18 Gain versus frequency for various ring lengths.

The surface current distributions of stepped-monopole excitation rectangular ring for different frequencies are shown in Fig. 4.20. It is found that they mainly distribute in the same direction along the side walls and bottom of the ring at the lower frequency, but they are weak along the stepped monopole. At the high frequency, they are mostly strong along the bottom of the ring and along the stepped monopole. These behaviors mean that the lower resonant frequency is affected by the

rectangular ring, and the stepped monopole has little effect on the performances at lower frequency. On the other hand, the upper frequency is more affected by the currents at the bottom of the ring and the stepped monopole, but there are little effects from the currents at the side walls of the ring.

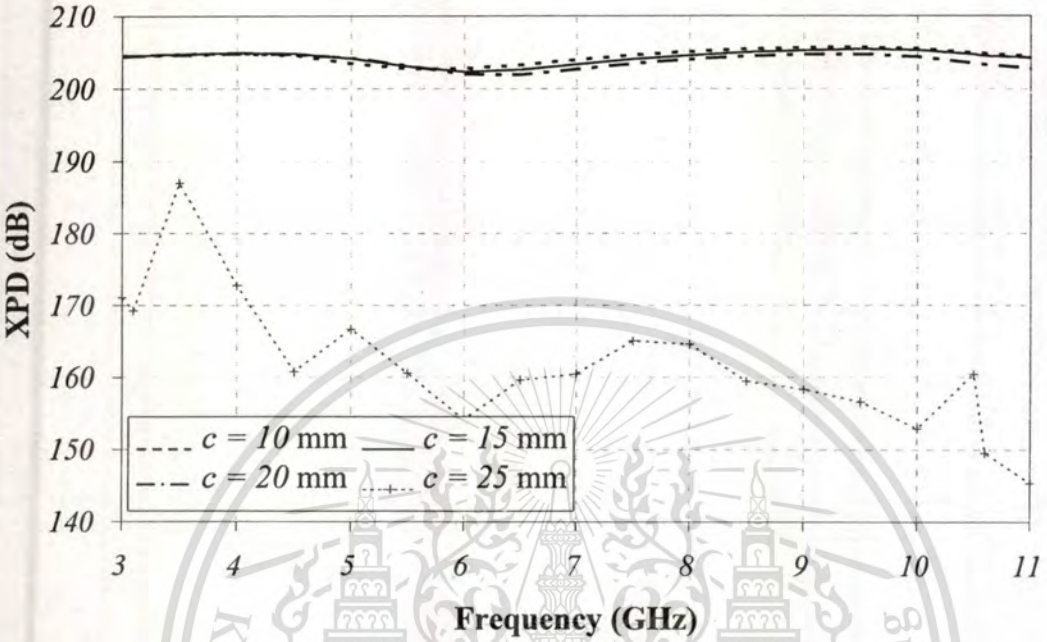

Fig. 4.19 XPD versus frequency for various ring lengths.

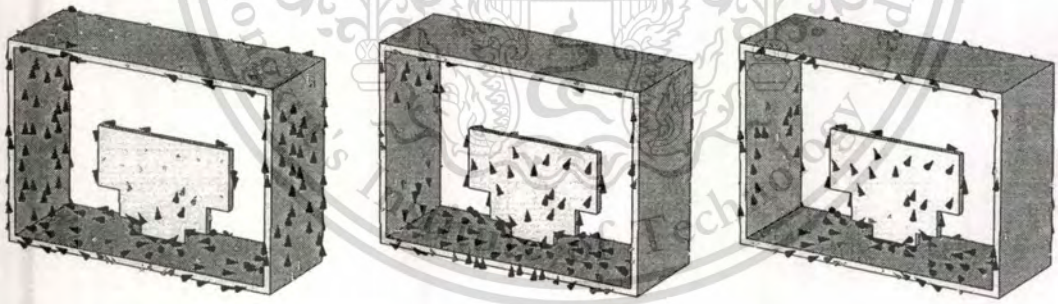

(a) (b) (c)

Fig. 4.20 Surface current distributions: (a) f = 3.1 GHz, (b) f = 6.5 GHz and (c) f = 10.6 GHz.

Furthermore, the electric field distributions at the apertures, which can be explained the radiation behaviors for different frequencies, are shown in Fig. 4.21. Note that the arrow shows the density and direction of currents and fields. It is found that at f = 3.1 GHz, the electric fields at the aperture strengthen at the center of the aperture. Therefore, a bidirectional pattern with the beam-peak direction of 0 degree is

obtained. At the higher frequency, the dense electric fields trend to bend out from the center to both sides of the ring as seen for example at the frequencies of 6.5 GHz and 10.6 GHz in Fig. 4.21. As the results, the radiation patterns in the *yz*-plane of the present antenna are tilted from the *z*-axis, and the symmetry radiation patterns in *xz*-plane are achieved as shown in Figs. 4.5 and 4.6.

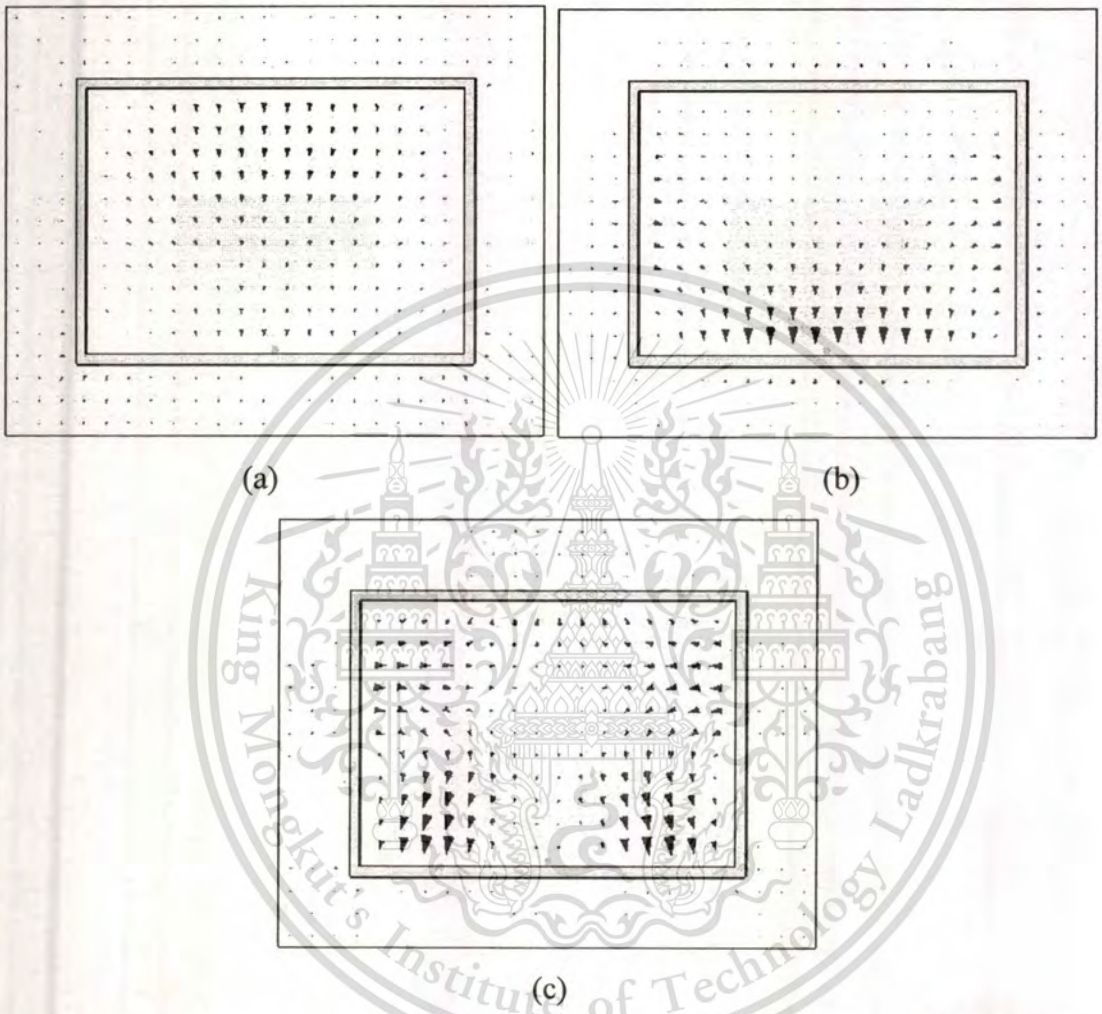

Fig. 4.21 Electric fields at the aperture: (a) $f = 3.1$ GHz, (b) $f = 6.5$ GHz and (c) $f = 10.6$ GHz.

4.4 Discussions

In this chapter, the bidirectional UWB antenna using a rectangular ring fed by a stepped monopole instead of a probe (linear-monopole) excitation is presented to improve the bandwidth of a probe-excited rectangular ring antenna. By spreading the width of linear-monopole to rectangular-monopole excitations, T-monopole and stepped-monopole excitations, the impedance bandwidth of the probe-excited rectangular ring antenna can be enhanced. By adding only two steps, it is enough for

applying the present antenna for the UWB system covered the frequency from 3.1 GHz to 10.6 GHz. However, for the antenna evolution in subsection 4.3.1, the impedance bandwidth seems to widen when the step is added. To see the effect of the additional steps on the excitations to the impedance bandwidth of the present antenna, the step is added from the stepped-monopole to hexagonal-monopole, trapezoidal-monopole and triangular-monopole excitations as shown in Fig. 4.22. It is found that only the suitable number of steps can be used to enhance the impedance bandwidth. That is the impedance bandwidth of the stepped-monopole, hexagonal–monopole and trapezoidal-monopole excitations can be improved by adding more steps, but it is worse by using the triangular-monopole excitation as shown in Fig. 4.23. In addition, the bottom width of the monopole excitation that connects to the coaxial transmission line should be spread for enhancing the impedance around the feed point as seen from the comparing between the frequency response of the trapezoidal-monopole and triangular-monopole excitations. For the radiation pattern of the antenna, it is strongly affected by the dimension of the rectangular ring as reported in the subsection 4.3.1. Therefore, by using the same dimensions of rectangular ring, the radiation pattern fairly stable providing a bidirectional pattern as achieved from the bidirectional UWB antenna using a rectangular ring fed by a stepped-monopole excitation (see Fig. 4.4 through Fig. 4.6). Note that, the simulations of the antenna model included the SMA connector are performed in this section.

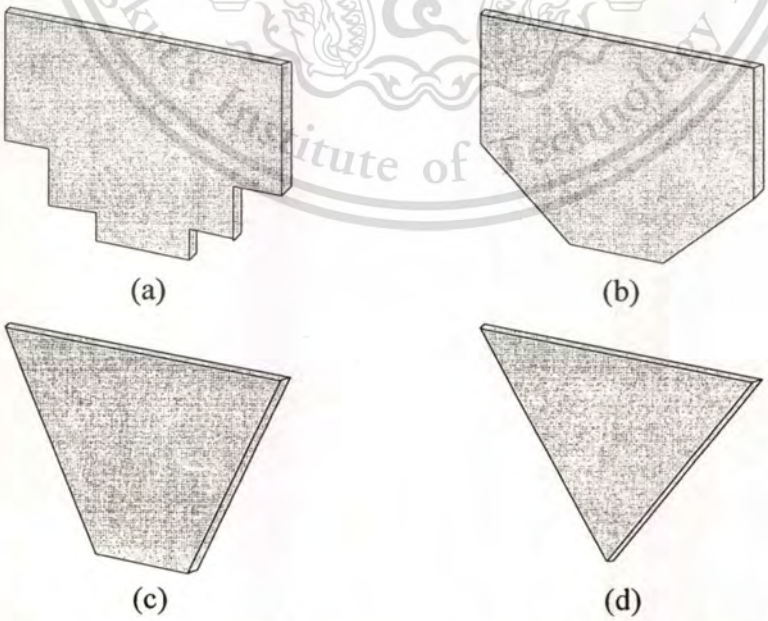

Fig. 4.22 Adding more steps on the monopole excitations: (a) stepped-monopole (b) hexagonal-monopole (c) trapezoidal-monopole (d) triangular-monopole.

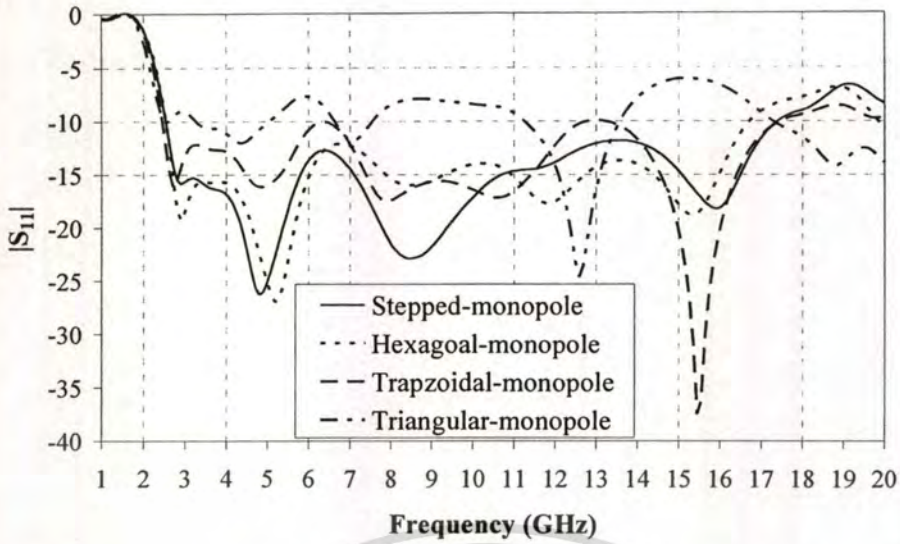

Fig. 4.23 $|S_{11}|$ of the bidirectional antenna by using rectangular ring excited by different feeders: (a) stepped-monopole (b) hexagonal-monopole (c) trapezoidal-monopole (d) triangular-monopole.

4.5 Summary

A bidirectional antenna using rectangular ring excited by stepped monopole to cover the UWB frequency range is presented in this chapter. The initial parameters of the antenna as well as the suitable parameters for enhancing bandwidth are investigated. In the design, the ring dimension is varied to obtain the desired upper and lower resonant frequencies. It is found that the lower frequency has been strongly influenced from ring contribution that can be seen from the dense currents. The bandwidth can be enhanced by improving the impedance that can be done by adjusting the parameters of stepped monopole. As the results, values of *a* of 40 mm, *b/a* of 0.7 and *h/b* of 0.6 are appropriately chosen providing the lower and the upper resonant frequencies at 3.1 GHz and 10.6 GHz with compact antenna size. At *b/a* = 0.7, the ring length is selected at the widest bandwidth with compact size. Moreover, the heights and the widths of stepped monopole are designed relating to the quarter wavelength of the upper edge frequency of 10.6 GHz in terms of $n\lambda_U / 4$. Apparently, the bandwidth can be enhanced using stepped-monopole excitation compared to the conventionally linear monopole. Furthermore, the $|S_{11}|$ is lower than -10 dB, and it provides the fairly stable bidirectional radiation pattern over the frequency range from 3.1 GHz to 10.6 GHz. At the desired direction, the simulated gain of 2.33-5.21 dBi is obtained. The validity of the simulated results is shown in the next chapter comparing to measured results.

CHAPTER 5
MEASUREMENT

5.1 Introduction

This chapter shows the fabrication and measurement of a rectangular ring fed by probe, and stepped monopole. The measurements are performed to confirm the validity of the proposed antenna design. Prototype antenna of a probe-excited rectangular ring is shown in Section 5.2. Subsequently, the radiation pattern, impedance in term of $|S_{11}|$ and gain are provided in Section 5.3. The comparisons between the simulated and measured results are plotted and discussed. Next, prototype antenna of a bidirectional UWB antenna by using a rectangular ring fed by stepped monople is shown in Section 5.4. Then, measurement is performed. The simulated and measured results are plotted and discussed in Section 5.5. The summary is finally provided in Section 5.6.

5.2 Prototype of a Probe-Excited Rectangular Ring Antenna

To verify the theoretical results, a prototype antenna was fabricated with the designed parameters as pointed in the previous chapter to operate at the operating frequency of 1.9 GHz. The ring was made of brass of 1 mm thickness with the dimension of the ring height equals 55 mm (0.35λ) and the ring width equals 110 mm (0.70λ). The ring length is 39 mm (0.25λ). This structure was excited by a linear electric probe made of copper rod with the diameter of 0.65 mm. The probe length was 43 mm (0.27λ). This probe was connected to a transmission line via an SMA connector. The photograph of the fabricated antenna is shown in Fig. 5.1.

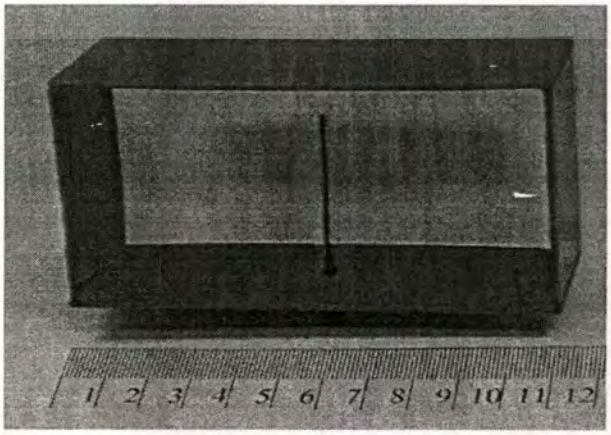

Fig. 5.1 Photograph of the prototype of a probe-excited rectangular ring antenna.

5.3 Results of a Prototype of Probe-Excited Rectangular Ring Antenna

This section shows the comparisons between the theoretical and experimental results. The antenna characteristics such as radiation pattern, gain and impedance are measured and shown next.

5.3.1 Radiation Pattern

To verify the theoretical radiation pattern using dyadic Green's function approach from Chapter 2 and MoM with RWG basis function (RWG-MoM) from Chapter 3, the plot between theoretical and measured results is shown in this subsection. By using an HP8720C Network Analyzer, the radiation pattern was measured.

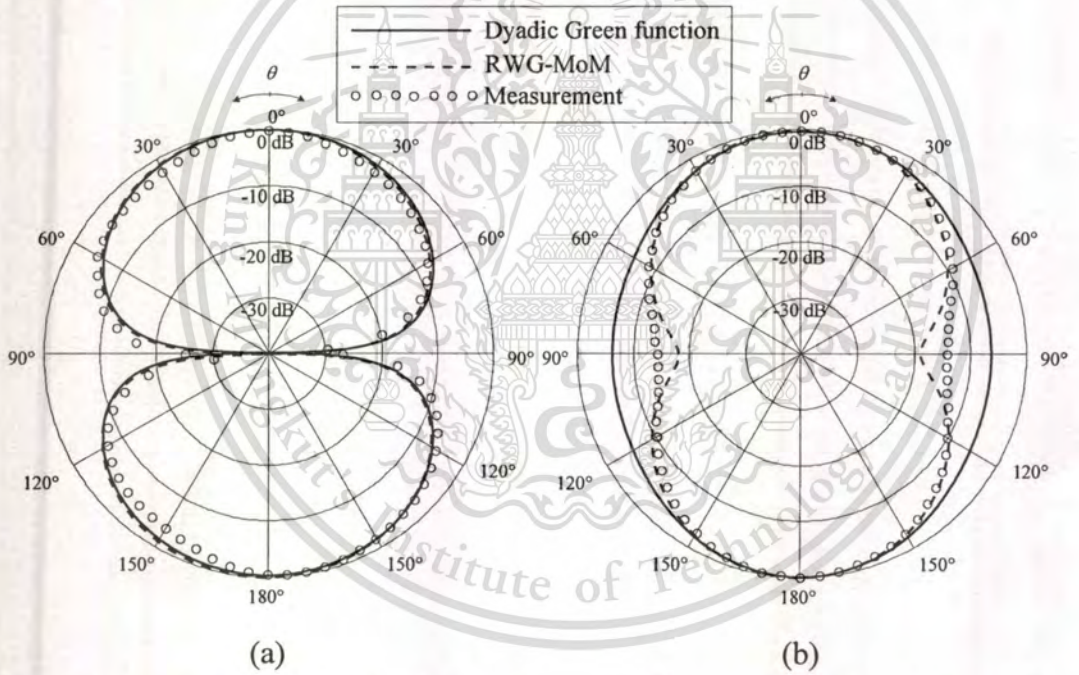

Fig. 5.2 Comparison of the simulated and measured radiation patterns: (a) *yz*-plane and (b) *xz*-plane.

The measured radiation pattern in *yz*-plane and *xz*-plane are shown in Fig. 5.2 (a) and Fig. 5.2 (b), respectively. Obviously, the maximum radiated field directs along the street cell in $+z$ and $-z$ directions. In *yz*-plane, beam shape of the radiation pattern from measurement is quite asymmetry because the linear probe is located at the bottom of the ring making unsymmetrical structure along *yz*-plane. It is found that beam-peak directions in *yz*-plane of the calculated dyadic Green's function approach,

RWG-MoM and measurement direct at 0, 3 and 0 degrees, with the half-power beamwidths of 89, 88 and 95 degrees, respectively. In addition, they are fairly coincided in this plane. For the symmetrical structure along *xz*-plane, the radiation pattern is symmetry in this plane. In *xz*-plane, the beam-peak directions of the simulation (from both dyadic Green's function approach and RWG-MoM) and measurement direct at 0 degree with the calculated dyadic Green's function approach, RWG-MoM and measured half-power beamwidths of 83, 66 and 74 degrees, respectively. The field in *xz*-plane from the dyadic Green's function approach widen at the direction of 90 degree, while the deeply field from RWG-MoM is provided. Nevertheless, they provide the same trend of radiation pattern. Although the sinusoidal current distributions, disregarded mutual coupling and omitted reflection at the edge of the ring is assumed, the experimental result provides the validity of the theoretical prediction.

5.3.2 Impedance and Gain

This subsection shows the comparisons of the simulated impedance characteristic and gain by using RWG-MoM from Chapter 3 and measurement. The matching impedance between coaxial transmission line with the characteristic impedance of 50 Ω and the antenna are plotted in terms of $|S_{11}|$ as shown in Fig. 5.3. Apparently, the simulation and measurement provide the lowest $|S_{11}|$ at $l = 0.27\lambda$ with $|S_{11}|$ of -30.46 dB and -34.32 dB, respectively, as shown in Fig. 5.3 (a). Moreover, the simulated and measured impedance bandwidths of 17% and 18% for the $|S_{11}| < -10$ dB are obtained, respectively. Apparently, the resonant frequencies are yielded at $0.99f_0$ and f_0 for the simulation and measurement, respectively. It is found that the simulation and measurement are in good agreement.

Furthermore, the gain of the antenna was also measured as shown in Fig. 5.4. It is apparent that the simulated and measured gains at the desired direction ($\theta = 0^\circ$ and $\phi = 90^\circ$) along the frequency range from $0.90f_0$ to $1.10f_0$, are between 4.50-5.28 dBi, and 4.19-5.13 dBi, respectively. It is found the minimum and maximum gains from the theory are obtained at the $0.90f_0$ and f_0 with gains of 3.89 dBi and 5.28 dBi, respectively. The minimum and maximum gains of measurement are yielded at the $0.90f_0$ and $1.05f_0$ with gains of 4.19 dBi and 5.13 dBi, respectively. At the operated frequency, gains of 5.28 dBi and 5.05 dBi are obtained from the computation and

measurement, respectively. Obviously the simulation and measurement are in good agreement.

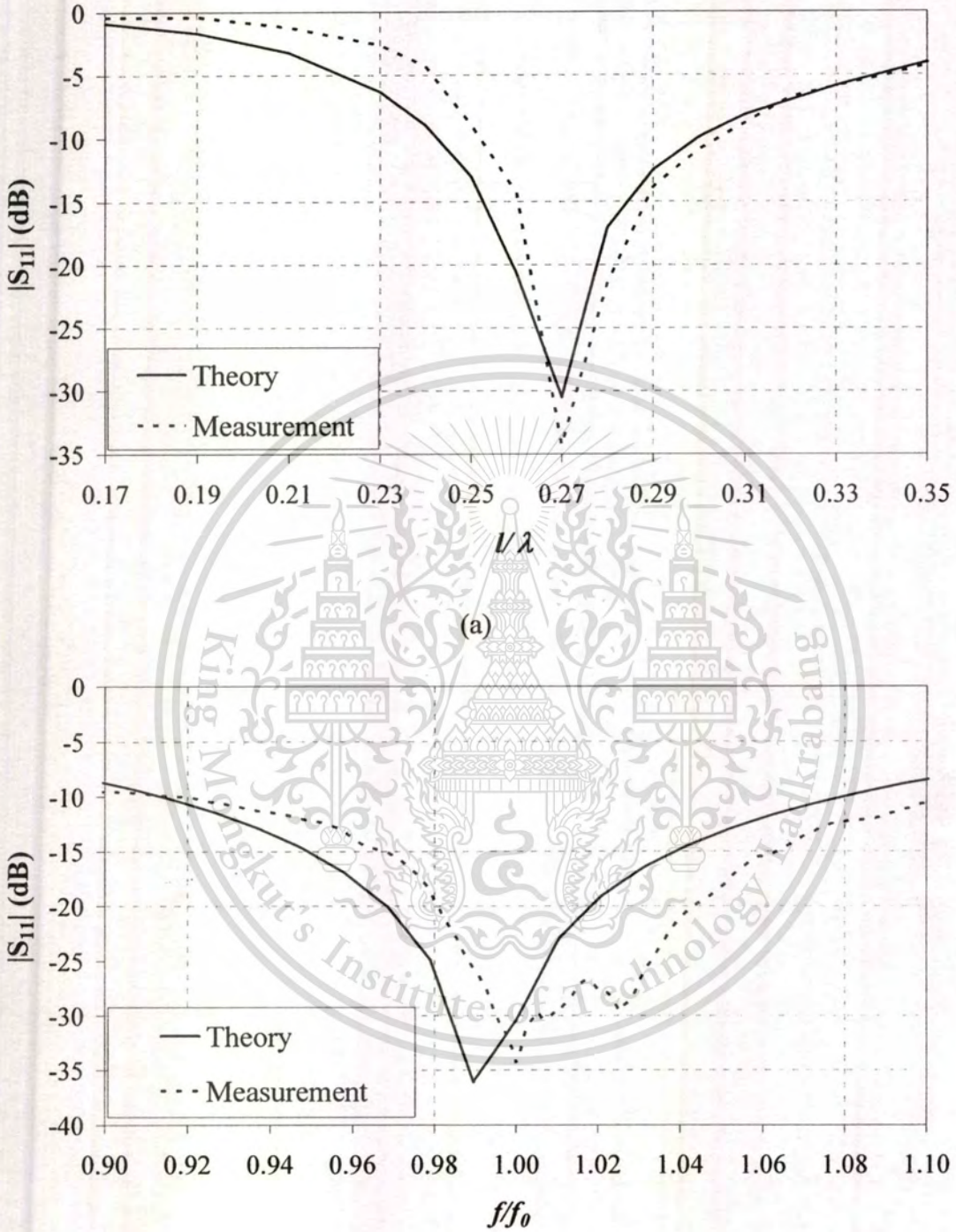

Fig. 5.3 Comparison between the simulated and measured $|S_{11}|$: (a) versus probe length (b) versus frequency.

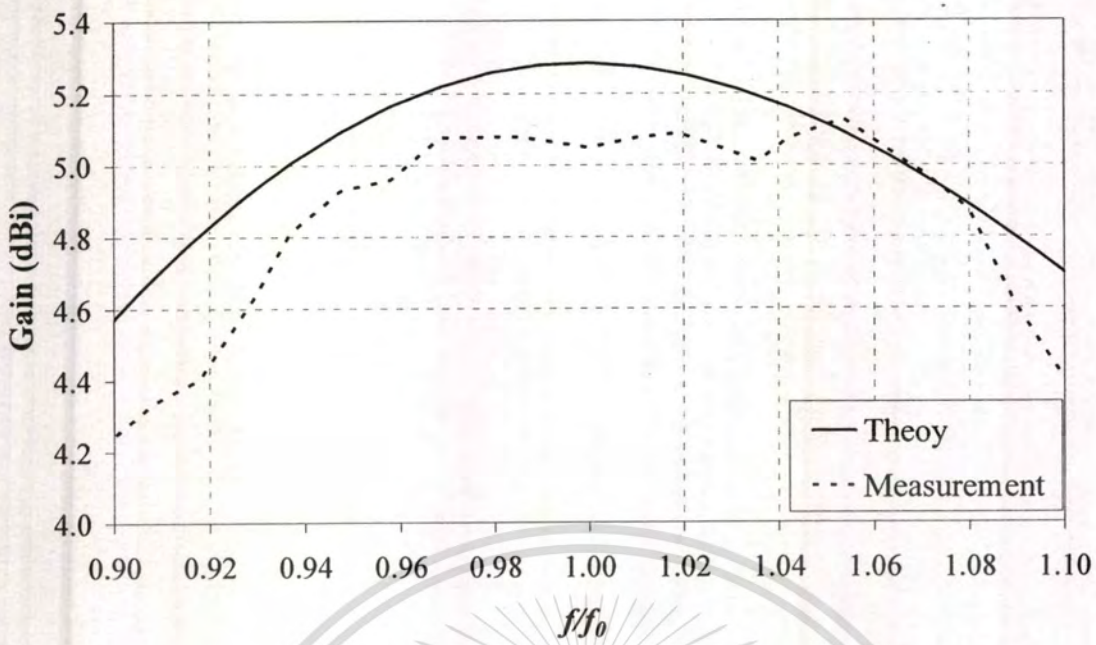

Fig. 5.4 Comparison the simulated and measured gains.

The comparisons between the theoretical and measured results of a probe-excited rectangular ring antenna are summarized and tabulated in Table 5.1.

Table 5.1 Comparisons results between the theory and measurement of a probe-excited rectangular ring antenna.

Antenna Characteristics		**Theory**		**Measurement**
		Dyadic Green's function	**RWG-MoM**	
Beam-peak direction (degree)	*yz*-plane	0	3	0
	xz-plane	0	0	0
Half-power beamwidth (degree)	*yz*-plane	89	88	95
	xz-plane	83	66	74
Gain (dBi)		5.28		5.05
$\|S_{11}\|$ (dB)		-30.46		-34.32
Band width (%)		17		18

5.4 Prototype of a Bidirectional UWB Antenna Using Rectangular Ring Fed by Stepped Monopole

To confirm the validity of the design and simulations of the bidirectional UWB antenna using rectangular ring fed by stepped monopole, the prototype antenna was fabricated from brass with the designed dimensions in Table 4.2. The photograph of the prototype antenna including coaxial feeding port is shown in Fig. 5.5. Then, radiation and impedance characteristics of the proposed antenna are measured and discussed next.

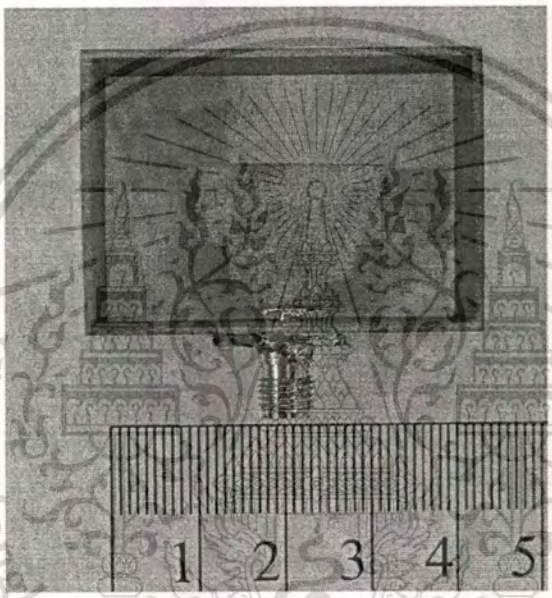

Fig. 5.5 Photograph of the prototype of a bidirectional UWB antenna using rectangular ring fed by stepped monopole.

5.5 Results of a Bidirectional UWB Antenna Using Rectangular Ring Fed by Stepped Monopole

The comparisons between simulation and measurement of radiation pattern, gain and impedance in terms of $|S_{11}|$ of a bidirectional UWB antenna using rectangular ring antenna fed by stepped monopole are presented in this section. For the far field radiation patterns, the designed antenna provides fairly stable bidirectional pattern over the UWB frequency as along the UWB frequency of 3.1 GHz, 6.5 GHz and 10.6 GHz as shown in Fig. 5.6 through Fig. 5.8. For the desired direction, the maximum radiated field directs along the street cell in $+z$ and $-z$ directions. It is found that the radiation pattern in yz-plane tilts from z axis because the stepped monopole is located

at the bottom of the ring making unsymmetrical structure along *yz*-plane. The beam peak in *yz*-plane from the simulation directs at 4, 30 and 39 degrees whereas the measured one directs at 10, 30 and 30 degrees for the frequencies of 3.1 GHz, 6.5 GHz and 10.6 GHz, respectively. At these three frequencics, the simulated half-power beamwidths are 86, 63 and 64 degrees, and the measured half-power beamwidths are 70, 60 and 55 degrees, respectively. Nevertheless, the field is still efficiently strong at the desired direction ($\theta = 0^{\circ}$ and $\phi = 90^{\circ}$). For the symmetrical structure along *xz*-plane, the radiation pattern is symmetry in this plane. The beam peak in *xz*-plane of simulation points at 0, 27 and 0 degrees, for the frequencies of 3.1 GHz, 6.5 GHz and 10.6 GHz respectively, with the simulated half-power beamwidths of 82, 112 and 44 degrees and the measured beam peak directs at 0 degree for those all frequencies with the measured half-power beamwidths of 60, 55 and 35 degrees. Moreover, the same trend of the radiation patterns from the simulation and measurement for different frequencies is obtained.

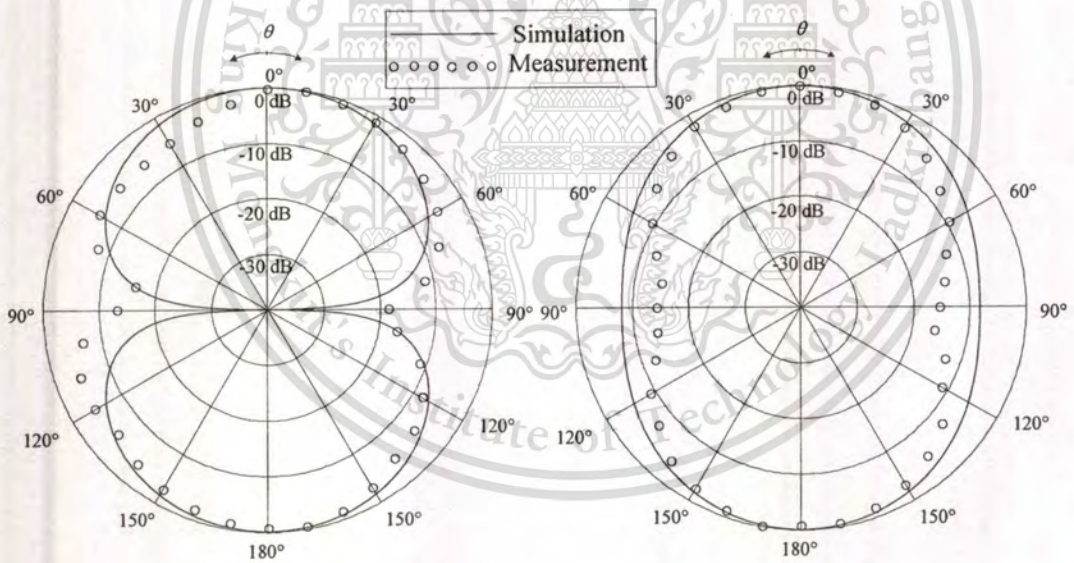

(a) (b)

Fig. 5.6 Radiation pattern at 3.1 GHz: (a) *yz*-plane and (b) *xz*-plane.

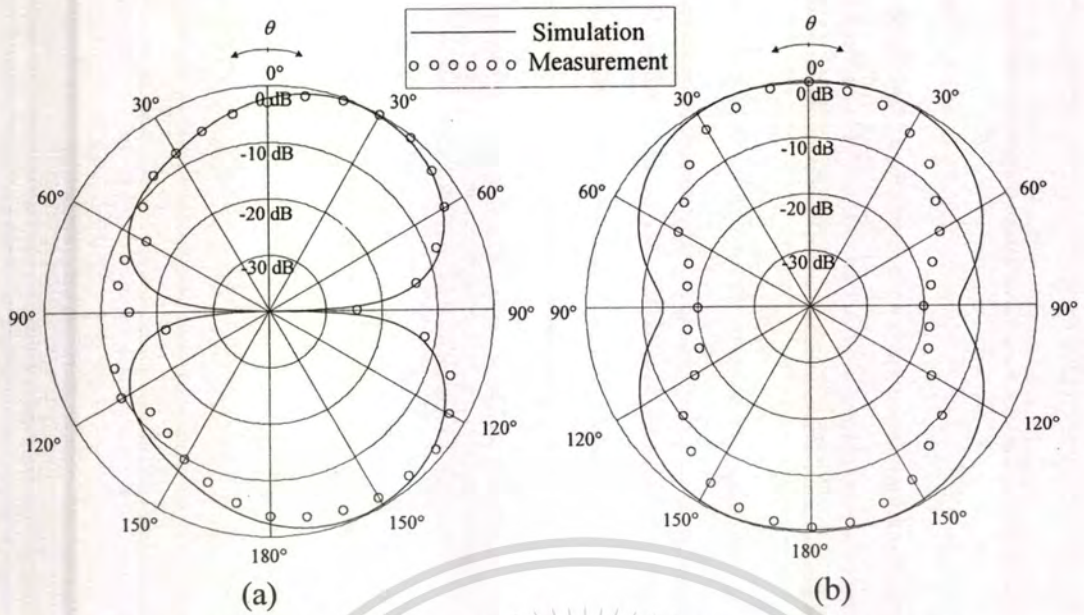

Fig. 5.7 Radiation pattern at 6.5 GHz: (a) *yz*-plane and (b) *xz*-plane.

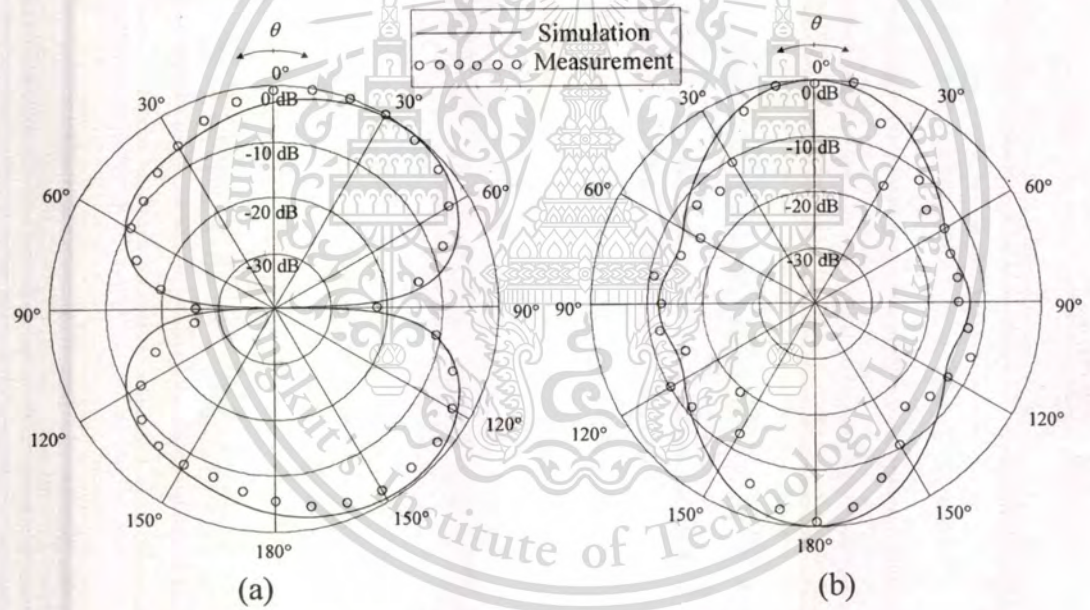

Fig. 5.8 Radiation pattern at 10.6 GHz: (a) *yz*-plane and (b) *xz*-plane.

In addition to radiation patterns, the gain of the antenna was also measured as shown in Fig. 5.9. It is apparent that the measured and simulated gains, at the desired direction ($\theta = 0^{\circ}$ and $\phi = 90^{\circ}$) along the frequency range from 3.1-10.6 GHz, are 2.44-4.98 dBi and 2.33-5.21 dBi, respectively; the minimum and maximum gains of measurement and simulation are yielded at the same frequencies of 6 GHz and 9.5 GHz, respectively. They are in fairly agreement.

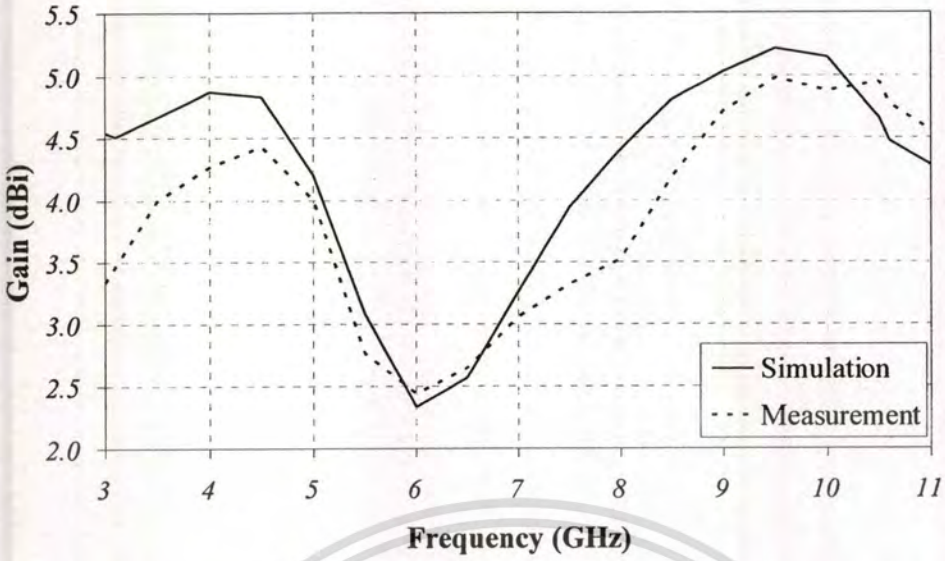

Fig. 5.9 Simulated and measured gains versus frequency.

In addition to the radiation characteristics, the impedance characteristic in terms of $|S_{11}|$ is investigated. It is found that the comparison between the simulated (simulation without SMA connector) and measured $|S_{11}|$ as shown in Fig. 5.10 is different at the frequency higher than 7.2 GHz due to the effect from the coaxial feed connector because the coaxial connector is excluded in the simulation to study only the antenna parameters without connector. However, to verify the discrepancy, the simulation with SMA connector is performed and found that the same trend of simulated and measured results is obtained as shown in Fig. 5.10. The minimum value of -26.15 dB and maximum value of -11.39 dB of the simulated $|S_{11}|$ with SMA connector are obtained at the frequencies of 5.92 GHz and 5.28 GHz, respectively. Nevertheless, the $|S_{11}|$ from both simulations with and without SMA connectors and the measurement are lower than -10 dB over the frequency range from 3.1-10.6 GHz which is significantly improved over the rectangular ring antenna fed by linear monopole that shown in chapter 3. The summarized results of the comparisons between simulation and measurement are tabulated in Table 5.2. It should be remarked that the coaxial connector should be included in the simulation especially for the design of wide-band antenna. Since, it has been influenced to the input impedance of the antenna especially at the high frequency. In addition, each type of connectors has its frequency response to the return loss depended on the properties of the material for implementation also [60]-[61].

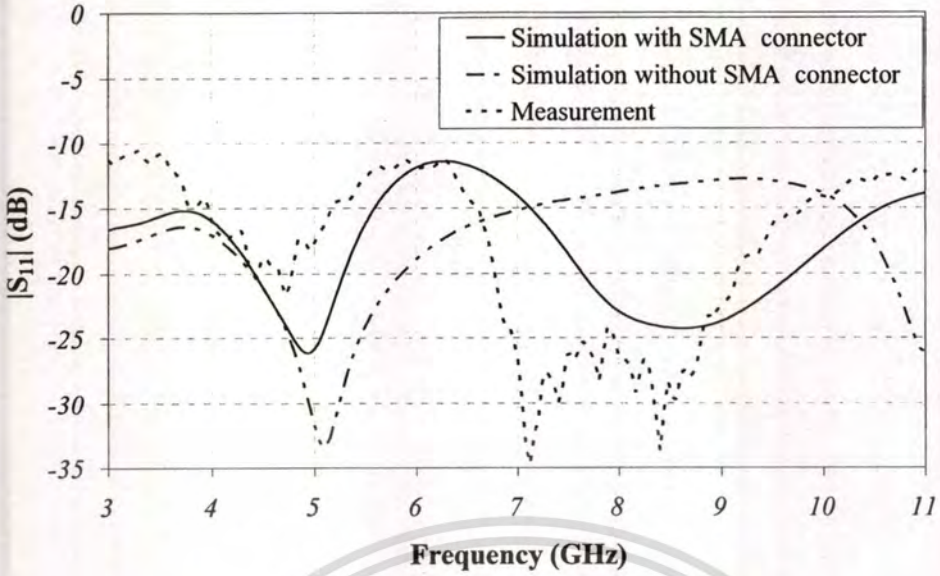

Fig. 5.10 Comparison of the simulated and measured $|S_{11}|$.

5.6 Summary

This chapter presents the measurement of bidirectional rectangular ring antennas fed by linear probe, and stepped monopole for verifying the theory from Chapters 2, 3 and simulations from Chapter 4, respectively. Apparently, the comparison of the radiation pattern between the dyadic Green's function approach, RWG-MoM and measurement are fairly good agreement. The radiation fields in the *yz*-plane are fairly coincide, while the same trend of radiation patterns in *xz*-plane are obtained with the widen and deepen fields at 90 degree from the dyadic Green function and RWG-MoM, respectively. Therefore, the dyadic Green's function approach from Chapter 2 can be used to predict radiation characteristics as well even the mutual coupling and reflection from the ring edges are not taken into account. Furthermore, the impedance and gain of the proposed antenna are also measured. As the results, the RWG-MoM, which uses an accurate current compared with the dyadic Green's function approach, as presented in Chapter 3 provides a reasonable good agreement with those measurements. However, applying the RWG-MoM, a number of sections of triangles according to the convergent criterion are first considered, and taken into account. Therefore, it is not convenient for solving problem that varies a lot of parameters like a bandwidth enhancement using a stepped monopole instead of linear monopole as shown in the Chapter 4. Therefore, the CST simulation is used to design and simulate the proposed antenna. The validity of simulations is also provided by refer to the

measurement. Hence, the antenna prototype was fabricated and measured. It is found that the simulations and measurements are reasonably in good agreement. These results are very useful to design a bidirectional UWB antenna by using rectangular ring fed by stepped monopole as well as for others wide band applications.

Table 5.2 Comparison results between the simulation and measurement of a bidirectional UWB antenna using rectangular ring fed by stepped monopole.

<table>
<tr><th colspan="2" rowspan="2">Antenna Characteristics</th><th colspan="3">Simulation</th><th colspan="3">Measurement</th></tr>
<tr><th>f=3.1 GHz</th><th>f=6.5 GHz</th><th>f=10.6 GHz</th><th>f=3.1 GHz</th><th>f=6.5 GHz</th><th>f=10.6 GHz</th></tr>
<tr><td rowspan="2">Beam-peak direction (degree)</td><td>yz-plane</td><td>4</td><td>30</td><td>39</td><td>10</td><td>30</td><td>30</td></tr>
<tr><td>xz-plane</td><td>0</td><td>27</td><td>0</td><td>0</td><td>0</td><td>0</td></tr>
<tr><td rowspan="2">Half-power beamwidth (degree)</td><td>yz-plane</td><td>86</td><td>63</td><td>64</td><td>70</td><td>60</td><td>55</td></tr>
<tr><td>xz-plane</td><td>82</td><td>112</td><td>44</td><td>60</td><td>55</td><td>35</td></tr>
<tr><td colspan="2" rowspan="2">Gain (dBi)</td><td>4.58</td><td>2.67</td><td>4.53</td><td>4.51</td><td>2.57</td><td>4.47</td></tr>
<tr><td colspan="3">2.44-4.98</td><td colspan="3">2.33-5.21</td></tr>
<tr><td colspan="2" rowspan="5">$|S_{11}|$ (dB)</td><td colspan="3">Without SMA connector</td><td rowspan="3">-11.18</td><td rowspan="3">-11.79</td><td rowspan="3">-21.79</td></tr>
<tr><td>-17.91</td><td>-16.41</td><td>-19.08</td></tr>
<tr><td colspan="3">With SMA connector</td></tr>
<tr><td>-16.47</td><td>-12.93</td><td>-23.40</td><td colspan="3" rowspan="2">-34.74 to -10.61</td></tr>
<tr><td colspan="3">Without SMA connector
-33.45 to -12.73
With SMA connector
-26.15 to -11.39</td></tr>
</table>

CHAPTER 6
CONCLUSIONS AND FUTURE WORK

6.1 Conclusions and Discussions

This thesis presents the analysis of a bidirectional pattern using rectangular ring antenna which is very simple structure. Its structure consists of feeders that are surrounded by rectangular ring. For the feeders in this thesis, a linear monopole (probe) is firstly considered to achieve bidirectional pattern, and then a stepped-monopole is used to enhance bandwidth of the antenna. A rectangular ring antenna fed by either linear- or stepped-monopoles produces a bidirectional radiation pattern that is suitable for applying in the confined areas such as in the building, underground shopping areas, subway station, highway, sky train station and etc.

Chapter 2 presents the theory of the bidirectional pattern using a probe-excited rectangular ring antenna including its structure and the derivation expressions by using dyadic Green's function approach providing a closed form solution. The normalized magnitudes of the equivalent electric and magnetic current densities for various modal distributions are shown. The effects of the excited probe and rectangular ring to the modal distributions are described. Then, the radiation characteristics, such as radiation pattern, beam-peak direction, half-power beamwidth and directivity, are analyzed. It is considered that the radiation pattern of a single aperture in forward- and backward-directions is shown under the condition that, field radiates only forward- and backward-directions, and there is no coupling between the apertures. Then, the total radiated fields (radiation pattern from two apertures) are provided by combining fields of a single aperture in forward- and backward-directions. To obtain the antenna parameters, the ring width and ring height are selected as the dimension of a standard waveguide operating at the dominant mode, because the cross-section of the antenna is the same as a rectangular waveguide. Thus, the ring width of a, and ring height of $b = a/R$ are selected, where R is the ratio of a/b and $R \geq 1$; in this thesis $R = 2$ is used. Then, the ring length is varied to achieve the bidirectional pattern with high directivity. It is found that the bidirectional pattern is provided when ring length c is from 0.10λ to 0.65λ and $c \geq 1.25\lambda$. The highest directivity is obtained at c equals to 0.4λ with directivity of 4.43 dBi. Considering at forward- and backward-directions, this antenna produces a linear polarization because

there is only one component. Due to the derivations are considered under the assumption that current is assumed, the mutual coupling and reflection of the aperture and the diffraction from edge of ring are neglected; therefore, impedance characteristics including gain of the antenna are incorrect.

Those problems in Chapter 2 are solved by using MoM with the RWG basis function as presented in Chapter 3 since this method uses the more accurate current compared to the dyadic Green's function approach in Chapter 2. Applying this approach, the surfaces of the proposed antenna are divided into a number of triangular patches. It should be pointed that the criterion of convergence should be care for selecting a number of patches. In this thesis, the criterion convergence consideration is that the deviation of input impedance is less than 1%. Consequently, the impedance, and gain are investigated for various probe length and probe position with different ring length. It is found that the ring length of 0.25λ with the probe length of 0.27λ located at the center ($x = s = 0, y = -b/2, z = 0$) provides the maximum gain of 5.28 dBi and the best impedance matching with $|S_{11}|$ of -30.46 dB. In addition, the current distribution is investigated. Apparently, the current distributes dense along the linear probe rather than on the ring, meaning that the radiation fields of linear probe are confined by rectangular ring to radiated in forward- and backward-directions. Moreover, the antenna bandwidth is determined. It is found that the probe-excited rectangular ring antenna provides bidirectional pattern with frequency band of 17% ($|S_{11}| < -10$ dB). Furthermore, the radiation pattern of the antenna is also plotted to compare with those obtained from Chapter 2.

In addition to a bidirectional pattern using a probe-excited rectangular ring antenna, the bandwidth enhancement is also presented. In this thesis, the bidirectional UWB antenna using rectangular ring fed by stepped monopole instead of linear monopole is introduced in Chapter 4. To study the antenna parameters, the simulations using the CST Microwave Simulation, which is very convenient for varying several parameters with less time consume compared to RWG-MoM in Chapter 3 in which the convergent criterion of RWG-MoM should be taken very good care for the accuracy when changing the antenna structure. The antenna revolutions to enhance the antenna bandwidth are presented. In the design, the ring dimensions are varied to obtain the desired upper and lower resonant frequencies. It is found that the lower frequency has been strongly influenced from the ring contribution that can be

seen from the dense currents. In addition, the impedance around the resonant frequency can be improved using extended the linear-monopole to rectangular-monopole excitations by spreading the width, T-monopole and stepped-monopole excitations. It is found that the ultra-wideband operation is achieved by using stepped-monopole excitation. The parameter study is presented. Consequently, the optimum parameters are achieved. As the results, the fairly stable bidirectional radiation pattern over the frequency range from 3.1 GHz to 10.6 GHz is provided with the simulated gain of 2.33-5.21 dBi at the desired direction. It should be noted that if the dyadic Green's function approach is applied in the design of the bidirectional UWB antenna using rectangular ring fed by stepped monopole, the current distribution on the stepped-monopole excitation is used instead of the sinusoidal distribution in (2.16) in Chapter 2. However, the input impedance of the antenna, which is the important characteristic in the contribution of Chapter 4, is still low correction under the same assumptions that used in Chapter 2. An alternative choice is that the use of the RWG-MoM to design the present antenna. However, the suitable number of triangular patches should be care when the structure of the antenna is changed.

To verify the results from Chapters 2, 3 and 4, the fabrication and measurement are reported in Chapter 5. The design and prototype of a probe-excited rectangular ring antenna at the operating frequency of 1.9 GHz is shown. Subsequently, radiation pattern in *yz*- and *xz*-planes are measured and plotted compared to the theory from Chapter 2. It is found that the theoretical and experimental results are fairly good agreement. Thus, the dyadic Green's function approach can be used to predict the radiation characteristics as well. In addition, impedance in terms of $|S_{11}|$ and gain are also measured to compare with those simulated results from MoM with the RWG basis function in Chapter 3. Again, they show a reasonably in good agreement. Furthermore, prototype of a bidirectional UWB antenna using rectangular ring fed by stepped monopole was fabricated and measured to verify the simulations in Chapter 4. The radiation pattern at the selected frequency of 3.1 GHz, 6.5 GHz and 10.6 GHz, gain and impedance in terms of $|S_{11}|$ over the UWB frequency are plotted. It is found that the simulated and measured results are in good agreement. Note that the SMA connector is included in the simulation for determining the impedance because it has an effect from the coaxial feed connector at the high frequency (over 7.2 GHz). Therefore, the coaxial feed connector should be included in the simulation to obtain the accurate results especially at the high frequency.

6.2 Remarks for Future Work

In this thesis, the analysis by using the dyadic Green's function has been omitted the mutual coupling between the two apertures and the diffraction at the edge of the ring. As the results, the radiation characteristics especially the radiation pattern in *xz*-plane from the dyadic Green's function widens, while the result from the RWG-MoM deepens around the direction of 90 degree. Therefore, those mutual coupling between the two apertures and the diffraction at the edge of the ring should be taken in to account for the better results. In addition, the more accurate current distribution on the probe excitation is also required [19]. The approximations on the probe may be divided into two parts. Firstly, a filament axial-concentrated current approximation can be used as a dipole antenna problem, while the second is the multi-filament current approximation around the cylindrical probe. These can probably improve the accuracy of the derivations.

Furthermore, the bidirectional UWB antenna using a rectangular ring fed by a stepped monopole instead of a linear probe excitation is presented to improve the bandwidth of a probe-excited rectangular ring antenna. By spreading the width of linear-monopole to rectangular-monopole excitations, T-monopole and stepped-monopole excitations, the impedance bandwidth of the probe-excited rectangular ring antenna can be enhanced. However, the parameters that used in the design are the sufficient parameters in the design for applying for UWB application. The dimensions of the present antenna can be further minimized. For example, the ring width of the antenna can be selected other shorter value rather than 40 mm, then, the relative parameters such as a ring height, monopole heights, and monopole widths will be reduced related to the ring width as the stated in the antenna design of Section 4.3 in Chapter 4. In addition, the ring length can be also reduced. Moreover, the impedance bandwidth of the antenna can be improved by using other shape of monopoles such as the hexagonal–monopole and the trapezoidal-monopole excitations as presented in Section 4.4 of Chapter 4. Furthermore, for other applications that require a bidirectional antenna, this type of antenna can be employed to serve by designing followed the guide line as reported in Chapter 4. Using the concept that the dimensions of the rectangular ring effect on the radiation pattern, while, the impedance characteristics affect by the feeder part.

REFERENCES

[1] K. Fujimori and H. Arai, "Propagation Characteristics in Tunnels Including Base Station Antenna," *IEICE Transactions on Communications*, vol. J82-B, no. 6, pp. 1220-1228, 1999.

[2] I.-F. Chen, "Low Cost Printed Omni-Directional Spiral-Mode Monopole Antenna for Wireless Applications," *IEICE Transactions on Communications*, vol. E87-B, no.6, pp. 1764-1766, 2004.

[3] L.-M. Si and X. Lv, "CPW-FED Multi-Band Omni-Directional Planar Microstrip Antenna Using Composite Metamaterial Resonators for Wireless Communications," *Progress In Electromagnetics Research*, PIER 83, 33-146, 2008.

[4] H. Arai, "Base Station Antennas Inside Tunnels and Subway Stations, and Outdoor Compact Base Station Antennas for PDC System in Japan", *The Proceedings of IEEE Antennas and Propagation Society International Symposium*, vol.1, pp. 568-571, 1999.

[5] H. Arai and K. Cho, "Cellular and PHS Base Station Antenna Systems," IEICE Transactions on Communications, no.9, pp. 980-992, 2003.

[6] K. Cho, T. Hori, H. Tozawa and S. Kiya, "Bidirectional Rod Antennas Comprising Collinear Antenna and Parasitic Elements," *IEICE Transactions on Communications*, No.6, pp. 1255-1260, 1998.

[7] K. Cho, T. Hori and K. Kagoshima, "Bidirectional Rod Antennas Comprising a Narrow Patch and Parasitic Elements," *IEICE Transactions on Communications*, no.9, pp. 2482-2489, 2001.

[8] H. Liu, B.-Z. Wang and W. Shao, "Dual-Band Bi-Directional Pattern Reconfigurable Fractal Patch Antenna for Millimeter Wave Application," *International Journal of Infrared and Millimeter Waves*, vol. 28, no. 1, pp. 25-31, 2007.

[9] S. Kosulvit, C. Phongcharoenpanich, M. Krairiksh and T. Wakabayashi, "Radiation Characteristics of a Bidirectional Antenna Using a Linear Probe in a Rectangular Ring," *The Proceedings of International Conference on Microwave and Millimeter Wave Technology*, pp. 337-340, 1998.

[10] S. Kosulvit, M. Krairiksh, C. Phongcharoenpanich and T. Wakabayashi, "A Simple and Cost-Effective Bidirectional Antenna Using A Probe Excited Circular Ring," *IEICE Transactions on Electronics*, vol. E84-C, no.4, pp. 443-450, 2001.

[11] S. Lamultree, C. Phongcharoenpanich, S. Kosulvit and M. Krairiksh, "Investigations of a Bidirectional Antenna Using a Probe Excited Rectangular Ring," *The Proceedings of Asia-Pacific Microwave Conference* 2005, vol.5, pp. 2943-2946, 2005.

[12] D. Srimoon, C. Phongcharoenpanich, and M. Krairiksh, "A Probe-Fed U-Shaped Cross-Sectional Antenna with Tuning Stubs on a U-Shaped Ground Plane," *IEICE Transactions on Communications*, vol.E89-B, no.5, pp.1636-1645, 2006.

[13] K. Chawanonphithak, C. Phongcharoenpanich, S. Kosulvit and M. Krairiksh, "Characteristics of an Elliptical Ring Antenna Excited by a Linear Electric Probe," *International Journal of Electronics*, vol. 94, no. 10, pp. 973-984, 2007.

[14] J. R. Risser, *Microwave Antenna Theory and Design*, Mc-Graw-Hill, 1949.

[15] A. Yaghjian, "Approximate Formulas for the Far Field and Gain of Open-Ended Rectangular Waveguide," *IEEE Transactions on Antennas and Propagations*, vol. 32, no. 4, pp.378-384, 1984.

[16] H. Jia, K. Yoshitomi, and K. Yasumoto, "Rigorous Analysis of Rectangular Waveguide Junctions by Fourier Transform Technique," *Progress In Electromagnetics Research*, PIER 20, pp. 263-282, 1998.

[17] M. E. Sabbagh and K. Zaki, "Modeling of Rectangular Waveguide Junctions Containing Cylindrical Posts," *Progress In Electromagnetics Research*, PIER 33, pp. 299-331, 2001.

[18] M. R. Booty and G. A. Kriegsmann, "Reflection and Transmission from a Thin Inhomogeneous Cylinder in a Rectangular TE_{10} Waveguide," *Progress In Electromagnetics Research*, PIER 47, pp. 263-296, 2004.

[19] J.-F. Liang, H.-C. Chang, and K. A. Zaki, "Coaxial Probe Modeling in Waveguides and Cavities," *IEEE Transactions on Microwave Theory and Techniques*, vol. 40, no. 12, pp. 2172-2180, 1992.

[20] H.-W. Yao and K. A. Zaki, "Modeling of Generalized Coaxial Probes in Rectangular Waveguides," *IEEE Transactions on Microwave Theory and Techniques*, vol. 43, no. 12, pp. 2805-2811, 1995.

[21] C. T. Tai, *Dyadic Green Functions in Electromagnetic Theory*, 2nd ed., IEEE Press, 1994.

[22] C. T. Tai, "On the Eigenfunction Expansion of Dyadic Green's Function," *The Proceedings of IEEE*, Vvol.61, pp. 480-481, 1973.

[23] D. T. Moroney and P. J. Cullen, "The Green's Function Perturbation Method for Solution of Electromagnetic Scattering Problems," *Progress In Electromagnetics Research*, PIER 15, pp. 221-252, 1997.

[24] S. Liu, L. W. Li, M. S. Leong, and T. S. Yeo, "Rectangular Conducting Waveguide Filled with Uniaxial Anisotropic Media: a Modal Analysis and Dyadic Green's Function," *Progress In Electromagnetics Research*, PIER 25, pp. 111-129, 2000.

[25] S. M. Rao, D. R. Wilton, and A. W. Glisson, "Electromagnetic Scattering by Surfaces of Arbitrary shape," *IEEE Transactions on Antennas and Propagation*, vol. AP-30, pp. 409-418, 1982.

[26] J. L. Volakis and D.B. Davidson, "Moment Antenna Simulation with Matlab: RWG Basis Functions," *IEEE Antennas and Propagation Magazine*, vol.43, no.5, pp.100-107, 2001.

[27] S. Lamultree and C. Phongcharoenpanich, "Bidirectional Ultra-Wideband Antenna Using Rectangular Ring Fed by Stepped Monopole," *In Electromagnetics Research*, PIER 85, pp. 227-242, 2008.

[28] Ultra-Wideband Operation FCC Report and Order, Tech. Rep. US 47 CFR Part 15, 2002.

[29] CST Microwave Studio, Release 5.0, 2004, Germany.

[30] C. A. Balanis, *Antenna Theory Analysis and Design*, John Wiley & Sons, 1997.

[31] C. A. Balanis, *Advanced Engineering Electromagnetics*, John Wiley & Sons, 1989.

[32] L. C. Godara, "Method of Moments Applied to Antennas," Chapter 8 in *Handbook of Antennas in Wireless Communications*, CRC Press, New York, 2002.

[33] M. N. O. Sadiku, *Numerical Techniques in Electromagnetics*, CRC Press, Florida, 1992.

[34] D. L. Knepp and J. Goldhirsh, "Numerical Analysis of Electromagnetic Radiation Properties of Smooth Conducting Bodies of Arbitrary Shape," *IEEE Transactions on Antennas and Propagation*, vol.AP-20, no.3, pp. 383-388, 1972.

[35] E. H. Newman and D.M. Pozar, "Electromagnetic Modeling of Composite Wire and Surface Geometries," *IEEE Transactions on Antennas and Propagation*, vol. AP-26, no. 6, pp. 784-789, 1978.

[36] A. W. Glisson and D.R. Wilton, "Simple and Efficient Numerical Methods for Problems of Electromagnetic Radiation and Scattering from Surface," *IEEE Transactions on Antennas and Propagation*, vol.AP-28, no. 5, pp. 593-603, 1980.

[37] S. M. Rao, D. R. Wilton and A. W. Glisson, "Electromagnetic Scattering by Surfaces of Arbitrary Shape," *EEE Transactions on Antennas and Propagation*, vol.AP-30, no. 3, pp. 409-418, 1982.

[38] J. L. Volakis and D. B. Davidson, "Moment Antenna Simulation with Matlab: RWG Basis Functions," *IEEE Antennas and Propagation Magazine*, vol.43, no. 5, pp. 100-107, 2001.

[39] S. N. Makarov, *Antenna and EM Modeling with MATLAB*, John Wiley & Sons, New York, 2002.

[40] X. H. Wu and Z. N. Chen, "Comparison of Planar Dipoles in UWB Applications," *IEEE Transactions on Antennas and Propagation*, vol. 53, no. 6, pp. 1973–1983, 2005.

[41] A. F. Almutairi, S. F. Mahmoud and N. A. Aljuhaishi, "Wide-Band Circular Patch Antenna with 2-Pin Loading for Wireless Communications," *Journal of Electromagnetic Waves and Applications*, vol. 19, no. 6, pp. 839–851, 2005.

[42] A. A. Eldek, A. Z. Elsherbeni and C. E. Smith, "Rectangular Slot Antenna with Patch Stub for Ultra Wideband Applications and Phased Array Systems," *Progress In Electromagnetics Research*, PIER 53, pp. 227–237, 2005.

[43] S. Lamultree, C. Phongcharoenpanich, S. Kosulvit and M. Krairiksh "A Wide Impedance Bandwidth of a Rectangular Ring Antenna Fed by Planar Disc Monopole," *The Proceedings of 2006 Asia-Pacific Microwave Conference*, vol. 3, pp. 2006-2009, 2006.

[44] S. Lamultree, C. Phongcharoenpanich and D. Torrungrueng, "Design of UWB Bidirectional Rectangular Ring Antenna Fed by Stepped Monopole," *The Proceedings of 2007 Asia-Pacific Microwave Conference*, vol. 3, pp. 1365-1368, 2007.

[45] F. Geran, G. Dadashzadeh, M. Fardis, N. Hojjat and A. Ahmadi, "Rectangular Slot with a Novel Triangle Ring Microstrip Feed for UWB Applications," *Journal of Electromagnetic Waves and Applications*, vol. 21, no. 3, pp. 387–396, 2007.

[46] W. Ren, J. Y. Deng and K. S. Chen, "Compact PCB Monopole Antenna for UWB Applications," *Journal of Electromagnetic Waves and Applications*, vol. 21, no. 10, pp. 1411-1420, 2007.

[47] G.-M. Zhang, J. S. Hong, B.-Z. Wang, Q. Y. Qin, J. B. Mo and D.-M. Wan, "A Novel Multi-Folded UWB Antenna Fed by CPW," *Journal of Electromagnetic Waves and Applications*, vol. 21, no. 14, pp. 2109-2119, 2007.

[48] S. A. Hosseini, Z. Atlasbaf and K. Forooraghi, "A New Compact Ultra Wide Band (UWB) Planar Antenna Using Glass as Substrate," *Journal of Electromagnetic Waves and Applications*, vol. 22, no. 1, pp. 47-59, 2008.

[49] A. Siahcheshm, S. Sadat, C. Ghobadi and J. Nourinia, "Design of a Microstrip Slot Antenna Filled by an Isosceles Triangle for UWB Applications," *Journal of Electromagnetic Waves and Applications*, vol. 22, no. 1, pp. 111-118, 2008.

[50] Z. N. Low, J. H. Cheong and C. L. Law, "Low-Cost PCB Antenna for UWB Applications," *IEEE Antenna and Wireless Propagation Letters*, vol. 4, pp. 237–239, 2005.

[51] J. Liang, C. C. Chiau, X. Chen and C. G. Parini, "Study of a Printed Circular Disc Monopole Antenna for UWB Systems," *IEEE Transactions on Antennas and Propagation*, vol. 53, no. 11, pp. 3500– 3504, 2005.

[52] L. Peng and C.-L. Ruan, "A Microstrip Fed Monopole Patch Antenna with Three Stubs for Dual-Band WLAN Applications," *Journal of Electromagnetic Waves and Applications*, vol. 21, no. 15, pp. 2359-2369, 2007.

[53] D. Guha, Y. M. M. Antar, A. Ittipiboon, A. Petosa and D. Lee, "Improved Design Guidelines for the Ultra Wideband Monopole-Dielectric Resonator Antenna," *IEEE Antennas and Wireless Propagation Letters*, vol. 5, no.1, pp. 373–376, 2006.

[54] C. B. Ravipati and C. J. Reddy, "Low Profile Disc and Sleeve Loaded Monopole Antenna," *The Proceedings of the IEEE Antennas and Propagation Society International Symposium,* vol. 2A, pp. 160–163, 2005.

[55] J. Guo, Y. Ji and Q. Liu, "Sleeve Monopole Antennas at the Center of a Circular Ground Plane," *IEEE Microwave and Optical Technology Letters*, vol. 38, no. 4, pp. 341–343, 2003.

[56] K. K. Kang, J. W. Lee, C. S. Cho, and T. K. Lee, "An Improved Impedance Bandwidth of Modified UWB Antenna with Staircased Parasitic Rings," I*EEE Antennas and Wireless Propagation Letters*, vol. 6, pp. 521-524, 2007.

[57] Y. Ren, and K. Chang, "An Ultrawideband Microstrip Dual-Ring Antenna for Millimeter-Wave Applications," *IEEE Antennas and Wireless Propagation Letters*, vol. 6, pp. 457-459, 2007.

[58] C. Phongcharoenpanich, S. Lamultree, S. Kosulvit and M. Krairiksh, "Theory and experiment of an antenna using a probe excited rectangular ring," *The Proceedings of the 2003 IEEE AP-S International Symposium on Antennas and Propagation and USNC/CNC/URSI North American Radio Science Meeting*, vol. 3, pp. 737-740, 2003.

[59] S. Lamultree, C. Phongcharoenpanich, S. Kosulvit and M. Krairiksh, "Radiation Characteristic Analyzes of a Probe-Excited Rectangular Ring Antenna by the Dyadic Green Function Approach" *The Progress In Electromagnetics Research B*, vol. 11, pp. 79-101, 2009.

[60] Components for Wireless Communication GigaLane Co., Ltd., "Application of SMA Connector," http://www.sjtechnology.co.uk/images/connectors/

[61] Johnsom Components™, "50 Ohm SMA Field Replaceable 4-Hole Flange Mount Jack Receptacle -With EMI Gasket," http://emersonnetworkpower.com/webapp/wcs/stores/servlet/ESC/resources/

RELATED PUBLICATIONS

[1] S. Lamultree and C. Phongcharoenpanich "Bidirectional Ultra-Wideband Antenna Using Rectangular Ring Fed by Stepped Monopole," *The Progress In Electromagnetics Research PIER 85*, pp. 227-242, 2008. (Impact factor of 3.320)

[2] S. Lamultree, C. Phongcharoenpanich, S. Kosulvit and M. Krairiksh, "Radiation Characteristic Analyzes of a Probe-Excited Rectangular Ring Antenna by the Dyadic Green Function Approach" *The Progress In Electromagnetics Research B,* vol. 11, pp. 79-101, 2009.

[3] S. Lamultree, C. Phongcharoenpanich, S. Kosulvit and M. Krairiksh, "A Wide Impedance Bandwidth of a Rectangular Ring Antenna Fed by Planar Disc Monopole," *The Proceedings of Asia-Pacific Microwave Conference 2006*, pp. 12-15, 2006.

[4] S. Lamultree, C. Phongcharoenpanich, S. Kosulvit and M. Krairiksh, "Investigations of a Bidirectional Antenna Using a Probe Excited Rectangular Ring," *The Proceedings of Asia-Pacific Microwave Conference 2005*, vol.5, pp. 2943-2946, 2005.

[5] C. Phongcharoenpanich, S. Lamultree, S. Kosulvit, M. Krairiksh and J. Takada, "Analysis of a Dihedral Corner Reflector Antenna Excited by a Probe inside Rectangular Ring," *The Proceedings of the 2004 International Symposium on Antennas and Propagation*, vol. 1, pp. 225-228, 2004.

[6] S. Lamultree, C. Phongcharoenpanich, S. Kosulvit and M. Krairiksh, "An Equivalent Circuit of a Bidirectional Antenna Using a Probe Excited Rectangular Ring," *The Proceedings of the 2004 IEEE International Symposium on Antennas and Propagation and USNC/URSI National Radio Science Meeting*, vol. 2, pp.1672-1675, 2004.

AUTHOR BIOGRAPHY

Suthasinee Lamultree was born in Maha-sarakham, North-east of Thailand. She received B. Eng. and M. Eng. degrees in Telecommunication Engineering from King Mongkut's Institute of Technology Ladkrabang (KMITL), Thailand, in 2000 and 2003, respectively. She received the best paper award from the International Conference on Information and Communication Technologies (ICT 2003), and the best student presentation from 2005 Electrical Engineering/Electronics, Computer, Telecommunications, and Information Technology (ECTI) International Conference. She won an IEEE Antennas and Propagation Society Graduate Scholarship for 2005-2006. In ECTI-CON 2008 international conference, she received the best paper award in communication systems. Her research interests are antennas, electromagnetics and microwave engineering. She is a student member of IEICE and ECTI association.